©2019

William P. Lustig

ALL RIGHTS RESERVED

LUMINESCENCE IN METAL-ORGANIC FRAMEWORKS: MECHANISMS AND APPLICATIONS AS PHOSPHORS AND SENSORS

By

WILLIAM P. LUSTIG

A dissertation submitted to the

School of Graduate Studies

Rutgers, the State University of New Jersey

In partial fulfillment of the requirements

For the degree of

Doctor of Philosophy

Graduate Program in Chemistry & Chemical Biology

Written under the direction of

Dr. Jing Li

And approved by

_____

_____

_____

_____

New Brunswick, NJ

October 2019

ABSTRACT OF THE DISSERTATION

Luminescence in metal-organic frameworks: mechanisms and applications as phosphors and sensors

By William P. Lustig

Dissertation Director:

Dr. Jing Li

Luminescent metal-organic frameworks (LMOFs) are a class of supramolecular material composed of metal ions connected by organic ligands to form crystalline frameworks that emit light when excited. In these organic-inorganic frameworks, single metal ions or metal ion clusters serve as 'nodes', with rigid multidentate ligand molecules linking these nodes into an ordered three-dimensional lattice. Luminescence can arise from the metal nodes, organic ligands, or interactions between these components. Because the properties of an LMOF depend on both the characteristics of the building blocks used to construct it and how these building blocks interact with each other, altering these building blocks can impart an incredible degree of tunability to an LMOF's properties. However, the complex interactions that are possible between framework components render the rational design of LMOFs with specific luminescent properties challenging.

This work used a combination of spectroscopic, crystallographic, and theoretical methods to understand the chemical and optoelectronic processes that take place within LMOFs. This understanding was then used to develop broadly-applicable strategies for the rational design of LMOFs for commercial applications, which were in turn used to design and synthesize several new LMOFs with record-breaking performance as optical sensors and phosphor materials. LMOF-241 was designed for the detection of common food-contaminating mycotoxins using a photoinduced electron transfer mechanism. It was used to optically detect mycotoxins with unprecedented speed and sensitivity, with detection limits on the ppb-scale. A chromophoric-ligand strategy was previously used to design LMOF-231 for use as a blue-excitable, yellow-emitting phosphor material in white LED bulbs, and it demonstrated the highest quantum yield for any yellow-emitting LMOF reported (76%). This exceptional quantum yield was improved to 88% in LMOF-231-$F_{0.2}$, which was designed using a bandgap–modulation strategy. Finally, the effect of post-synthetic structural rigidification on LMOF quantum yield was studied using the isostructural LMOFs-263 and 301. This work demonstrated that rigidification via structural packing is an effective strategy for increasing luminescence efficiency, with LMOF-263 demonstrating a nearly five-fold increase in quantum yield.

ACKNOWLEDGEMENTS

I would first like to thank my research advisor, Dr. Jing Li, for her incredible support throughout the course of my degree. The faith that she has put in me, the guidance she has given me, her unwavering encouragement, and the incredible patience she has shown me have helped me to accomplish something that I once believed was out of my reach. I will always strive to meet the example she has set, as both a scientist and a person.

I would also like to thank Dr. Deirdre O'Carroll, Dr. Ralf Warmuth, and Dr. Zhichao Hu for serving on my committee and for the insight and advice you have given me over the years. I am also extremely grateful for the time that I got to spend with the members of the Li Group. Past and present, your collaboration and friendship has been invaluable. I would especially like to thank Dr. Zhichao Hu, Dr. Ben Deibert, Dr. Nathan Rudd, and Ever Velasco. I sincerely appreciate all of the collaborators who have worked with me, especially Dr. Fangming Wang, Dr. Simon Teat, Dr. Zeqing Shen, Dr. Soumya Mukherjee, Dr. Sujit Ghosh, and Dr. Timo Thonhauser.

Thank you to my mother, Mary Nell Cummings, my father, Tom Lustig, and my brother, Jimmy Lustig, because I couldn't have done this without your support. Thank you to my amazing girlfriend Andrea Bermeo-Villalva, who is always there for me. And finally, thank you to my dog, Geno, who kept me sane.

Table of Contents

List of Tables

List of Figures

Chapter 1: Introduction

1.1 Luminescent Metal-Organic Frameworks

Metal-organic frameworks (MOFs) are crystalline solids composed of single metal ions (primary building units, PBUs) or metal ion clusters (secondary building units, SBUs) linked together by organic ligands with multiple binding sites to form extended network structures. As MOFs are crystalline materials, diffraction techniques can provide precise information about their structure, while their chemical and physical properties can be well tuned by varying the identity of the metal ions, organic ligands, and overall connectivity of the framework. Additionally, their porous nature allows guest species to be encapsulated within them. As a result, functional MOF materials have been reported for a wide variety of applications, including gas separation and storage,[1,2,3] proton conduction,[4,5] catalysis, [6,4] and drug delivery, [7,8] among others.

This tunability also extends to their luminescent properties. Luminescence in MOFs can arise from the organic ligands, metal centers, guest species, or from processes that involve multiple structural components. Luminescent MOFs (LMOFs) have found promising applications in imaging,[9,10] sensing,[11-14] and optoelectronics,[15,16] as well as in solid state lighting (SSL) devices.

1.2 MOF Luminescence Mechanisms

Photoluminescence occurs when the absorption of light creates an excited electronic state, which then emits a photon as it decays back to a ground state. Photoluminescence can be broadly characterized as fluorescence or phosphorescence. In fluorescence, an electron is excited into some singlet excited state (S*n*) and quickly relaxes into the lowest singlet excited singlet state (S1). Emission then occurs when the electron makes the spin-allowed transition

from S1 to the ground state (S0) (fig. 1). This process is fast, usually taking less than 1 microsecond to occur. In phosphorescence, an electron is again excited into some singlet state (S*n*) and relaxes into the lowest excited singlet state S1—however it then undergoes intersystem crossing into the triplet excited state (T1). Emission is associated with the spin-forbidden transition from T1 to the ground state (S0) (fig. 1). As the emissive transition is spin-forbidden, this process is slower, typically on the order of milliseconds or longer. However, as there is no an exact cutoff in terms of the excited state lifetimes in fluorescence and phosphorescence, identifying which process is at work can be nontrivial. These emission processes also compete with non-radiative excitation decay processes, for example, transitions associated with vibrational states provide avenues for excited states to relax through releasing heat, rather than a photon (fig. 1). Quantum yield is used to quantify the efficiency of photoluminescence processes. The internal quantum yield (IQY) of a material is the percentage of absorbed photons which are emitted, while the external quantum yield (EQY) is the percentage of incident photons which, following absorption, result in the emission of a photon from the phosphor.[15] The difference between the two is that the internal quantum yield describes only the efficiency of the emissive step in photoluminescence, while the external quantum yield provides the efficiency of the entire photoluminescence process, including the initial absorption of the photon.

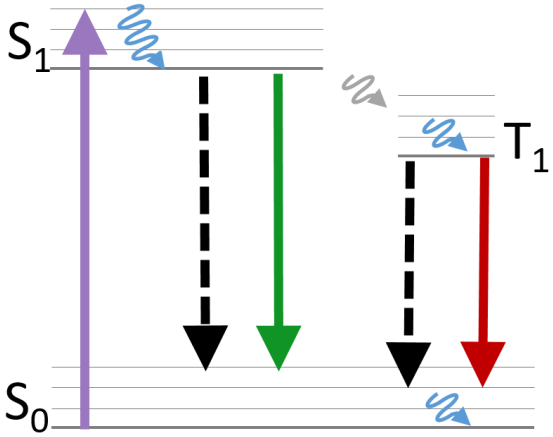

Figure 1. Jablonski diagram showing the processes active in photoluminescence. Excitation (purple arrow) is followed by fast relaxation (blue arrow) to the S1 singlet state, which can emit a photon through fluorescence (green arrow), decay via a non-radiative process (dashed arrow) or undergo intersystem crossing (grey arrow) to the T1 triplet state, which can in turn emit a photon through phosphorescence (red arrow) or decay nonradiatively (dashed arrow).

In LMOFs, the composite nature of the frameworks can result in complex photoluminescence processes. Broadly speaking, LMOF and LCP luminescence can involve metal ions, ligand molecules, and guest molecules, and the process can either be localized on one species or result from charge transfer between multiple species (fig. 2).

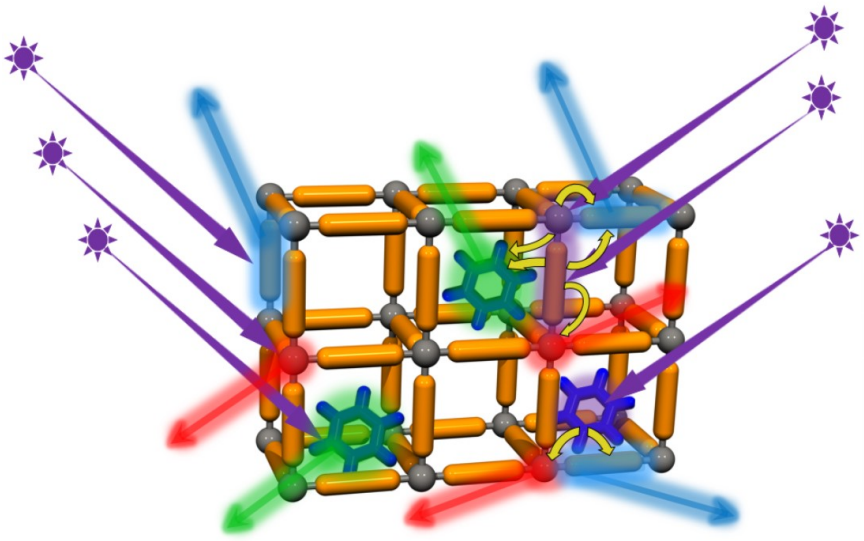

Figure 2. Diagram showing the luminescence processes most commonly active in LMOFs and LCPs. Excitation is shown in purple. Charge and energy transfer processes are indicated by yellow arrows.

Emission from ligands is shown in blue, while emission from metals is shown in red, and emission from guests is shown in green.

Ligand-centered emission is a fairly common mechanism in LMOFs and LCPs, as the majority of MOFs and CPs are constructed on rigid ligand molecules, and the vast majority of rigid ligands are aromatic. In large, the extended conjugation of ligand molecules can often bring ligand HOMO/LUMO (highest occupied molecular orbital/lowest unoccupied molecular orbital) energy gaps into the visible range, potentially resulting in emission energies falling in the visible range.[17] In LMOFs and LCPs with purely ligand-centered emission, there is neither orbital mixing between ligand molecules and the metal ions they are coordinated to, nor energy transfer processes between ligand molecules. These frameworks can be considered to be arrays of single luminescence centers. The differences in luminescence between these frameworks and the bulk ligand are primarily related to the immobilization of the ligand molecules, as upon incorporation into a framework, certain molecular motions pertinent to the free ligand are prevented or otherwise limited. This in turn can lead to an increased quantum yield, as fewer non-radiative excitation decay pathways are available, as well as broadened emission peaks.[18]

Metal-centered emission in LMOFs and LCPs generally stems from lanthanide ions within a framework. Lanthanide ion luminescence can produce emission covering the spectrum from UV to NIR emission—in the case of most trivalent lanthanide ions, this emission comes from a f-f electronic transition. Because only f orbitals participate in the transition, and because these orbitals are shielded by the closed 5s and 5p orbitals, these transitions are insulated from environmental and ligand effects; luminescence resulting from these transitions is therefore extremely sharp and characteristic for each lanthanide. However, as f-f transitions are parity-forbidden, most lanthanide ions have extremely poor absorption, resulting in weak emission under direct excitation.[15]

Sensitization is an important process that can be used to circumvent this, in which excitation energy is absorbed by a ligand molecule, then transferred to a metal ion that would otherwise have weak absorption. This is also referred to as an antenna effect, and enables strongly-emissive LMOFs and LCPs to be constructed which take advantage of lanthanide luminescence. In this process, initial absorbance occurs on the (antenna) ligand, and is followed by intersystem crossing from the ligand singlet state into the ligand triplet state. This in turn is followed by energy transfer from the ligand triplet state to the lanthanide triplet state (fig. 3). The nature of the interaction between the antenna species and the lanthanide ion determines the type of energy transfer process that is active in the mechanism. For lanthanide ions which are bonded to antenna ligands, Dexter energy transfer mechanisms predominate, while Förster resonance energy transfers are responsible for most energy transfer for non-bonded antenna/emitter pairs.[15] Following the injection of excitation energy from the ligand triplet state into the lanthanide triplet state, characteristic La(III) emission occurs. Because the excitation event occurs on the ligand species, the parity-forbidden f-f transitions that are responsible for La(III) species' poor absorption can be avoided, drastically increasing the emission from the lanthanide.[19]

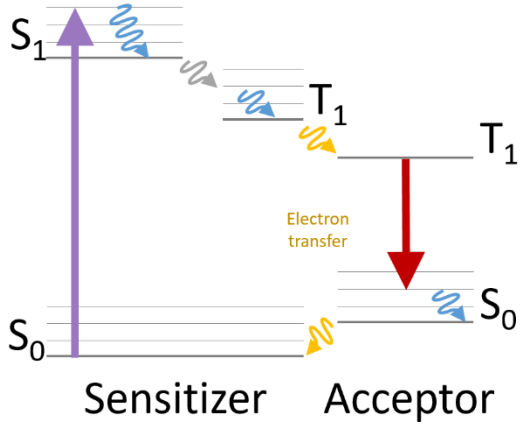

Figure 3. Jablonski diagram showing the processes involved in sensitization, with excitation on the sensitizer/antenna species undergoing intersystem crossing from the S1 into the T1 state, followed by transfer into the acceptor species.

Guest-centered emission occurs when guest species present in the pores of the framework serve as luminescence centers within a LMOF or LCP. The identity of this guest species can vary widely from molecular organic phosphors, to fluorescent metal complexes, to metal ions or nanoparticles. These guests can either provide the entirety of an LMOF or LCP's emission, or the guest's emission energy can be chosen to compliment the emission from the framework, resulting in broad spectrum emission from the material.[20-21] These guests can be introduced into the framework in several different ways. In "ship in a bottle" synthesis, guest components are taken up into LMOF pores before self-assembly into an emissive guest species, while in "bottle around a ship" synthesis, guest species are present in the initial synthesis of the framework, and the framework forms around the guest species, incorporating them formation of the framework. These two methods are more common for large, electrically neutral guests (molecular phosphors, metal nanoparticles), while ion exchange processes are more common for ionic guests.[22-23] In these, charge-bearing frameworks undergo ion exchange between the guest species and charge-balancing ions present in the framework's pores. Additionally, guests whose size is smaller than the pore windows in a porous MOF can often be incorporated through diffusion-mediated processes, wherein the MOF is soaked in a

solution containing the guest for some period of time, allowing the guest molecules to diffuse into the material.[24]

The previously described luminescence mechanisms focus on processes with absorption and emission on the same species. However, more complex emission mechanisms are often present in LMOFs and LCPs, with absorption by one species followed by charge transfer to another species, with emission occurring on that secondary species. Additionally, emission can occur between molecular orbitals with contributions from more than one component of the framework.

Ligand-ligand charge transfer (LLCT) emission mechanism involve luminescence from orbitals with contributions from multiple ligand molecules, or luminescence resulting from energy transfer from an absorber ligand to an emitter ligand. As ligands of LMOF and LCP are typically aromatic, frameworks which result in ligand stacking can exhibit orbital mixing between ligand molecules based on pi-pi interactions. If multiple ligands with different oxidation/reduction potentials participate in stacking, this can also lead to charge transfer emission processes. For ligand molecules with greater separation, Förster resonance energy transfer (FRET) mechanisms can move excitation from one ligand to another.[12] However, this would depend on overlap between the emission and absorbance spectra of the two ligands, and that the ligands are oriented appropriately for dipole-dipole coupling.

Ligand to metal charge transfer (LMCT), like LLCT, can either result from orbital mixing between metal ions and ligand molecules, or from absorbance on ligands followed by energy transfer onto the metal, where emission occurs. In LMCT luminescence through orbital mixing, the LUMO is primarily based on orbitals from the metal ion, with the HOMO primarily composed of ligand orbitals. Transition metal ions with closed d subshells (i.e. d^0 and d^{10} metals) are known to participate in LMCT luminescence, as the large gap between their

HOMO and LUMO that comes from having a closed d subshell effectively prevents metal-centered emission processes.[25] However, as metal ions with closed-d subshells have high-lying LUMO energy levels, ligand molecules with similarly high-lying HOMO energy levels are generally required for LMCT in the visible range. As a result, a combination of closed-subshell metals that can be partially reduced, such as the d^{10} metals Zn(II) or Cd(II) used in combination with ligand molecules that can be easily/partially oxidized and have high-lying HOMO energy levels can often lead to LMCT luminescence.[15]

In metal to ligand charge transfer (MLCT), transitions between mixed metal/ligand orbitals are responsible for luminescence, with the majority of the HOMO being contributed by metal orbitals, and the majority of the LUMO being contributed by ligand orbitals. Like LMCT, d^{10} metals can participate in MLCT as their large HOMO/LUMO gap prevents metal-centered luminescence in the visible range. However, as the metal and ligand contributions to the framework HOMO/LUMO are inverted relative to LMCT, so too are the oxidation/reduction requirements. Metals that can be partially oxidized, such as Cu(I) and Ag(I) can participate in MLCT luminescence with ligands that have low-lying LUMO and can be partially reduced.[26]

Mechanisms of host-guest charge transfer depend primarily on the nature of the guest species, but follow the general patterns laid out in previous mechanisms. Dyes with conjugated or aromatic moieties can interact with the aromatic ligands of the framework through pi-pi interactions, resulting in Dexter energy transfer mechanisms which can transfer excitation energy between the host framework and guest species. Through careful selection of guest and ligand molecules with appropriate reduction/oxidation potentials, redox-mediated charge transfer can also play an important role in charge transfer, as can Förster resonance energy transfer over longer distances.[27] When the guest species is a metal ion, often a lanthanide, it

can be chelated by free oxygen or nitrogen containing moieties in the ligand, or it can be located more generally in the pore.[23, 28] As with the previously described sensitized LMCT luminescence, chelated lanthanides participate in luminescence through a Dexter energy transfer process, while free lanthanides participate in luminescence through Förster resonance energy transfer.

1.3 LMOFs as Optical Sensors

In optical sensing, the presence of a given analyte is detected through the modulation of luminescence from a probe material. This typically involves emission turn-on, emission turn-off, or shifts in the emission energy/wavelength from the luminescent probe. This type of sensing is advantageous in that it combines technical simplicity with the potential for extremely powerful performance. The instrumentation required only consists of an excitation source, probe material, emission detector, and signal output. The resulting devices can be extremely cost effective, and depending on the specific application, can often be compact enough for mobile use. Moreover, despite their low cost, small size, and ease of use, selective ppb-level sensitivity can be achieved through careful design of the probe material.

An effective luminescent probe should have short response time, good sensitivity and selectivity for the analyte, strong emission when in the on-state, high stability and reusability in real-world conditions. Because of their exceptional tunability, luminescent metal-organic frameworks (LMOFs) are especially effective in this role.

Porosity, pore geometries, and pore surface chemistry can be controlled to maximize selective interactions between the framework and the analyte material. This allows for the sensitivity, selectivity, and recyclability of the probe to be optimized. Simple adjustments of the pore dimensions allow for size-based selectivity. This can be accomplished by adjusting the actual pore size and geometry, or by partially occluding the pore through functionalization

of the inner surface or the inclusion of guest molecules.[29] Similarly, controlling the chemical environment of the pore through ligand design, ligand functionalization, or specific guest inclusion can allow for the selection of species by their chemical properties. Through the use of hydrophobic ligands, for example, hydrophilic molecules may be excluded from the pores of the material, further increasing its selectivity for a given hydrophobic analyte.[30] In addition to tuning the broad chemical environment, specific functional groups that interact strongly with the desired analyte may be included in the pore to enhance selectivity for that material. Ligands with Lewis-basic moieties, such as amine-based functional groups, can be used to increase interactions with Lewis-acidic analytes.[31] Post-synthetic removal of terminal ligands may expose open metal sites, allowing for the coordination of Lewis-basic analytes.[32] Ligands with large, planar, aromatic regions can increase π-π stacking interactions between the framework and aromatic analyte molecules.[33] These optimizations not only impact selectivity, but sensitivity as well. By improving the ability of an LMOF to selectively interact with the analyte material, preconcentration of the analyte within the LMOF can be achieved.[34] This increases the local concentration of the analyte, allowing for extremely efficient sensing even when the general concentration of the analyte might otherwise be too low to detect.

LMOFs are also well suited as luminescent probe materials because of their capacity for strong emission and the diversity of luminescence mechanisms available to them. Until now, these charge transfer and energy transfer mechanisms have been discussed as functioning between ligand molecules and metal ions. However, the inherent porosity of MOFs permits analyte molecules within the pores to participate in—or interfere with—these mechanisms as well. Guest molecules can act as independent luminescence centers, or they can participate in charge transfer to and from ligands or metals. Finally, multiple emission mechanisms can occur simultaneously within a single LMOF.

In designing an LMOF-based probe material to take advantage of these mechanisms, many options are available. As an analyte interacts with an LMOF it may induce changes in the emission wavelength, emission quenching, or emission enhancement. Shifting the emission energy occurs when interactions between the analyte and LMOF alter the LMOF electronic structure.[22] This can be accomplished through including functionality that directly interacts with the targeted analyte as described above. Additionally, it is possible to take advantage of solvochromic behavior in an LMOF, where the adsorption of polar or nonpolar molecules can stabilize or destabilize the excited state and thereby alter LMOF excited state energy levels and the wavelength of resulting emission.[35]

The most common quenching mechanisms are charge transfer, in which a photoexcited electron is transferred from the higher-lying LUMO of the LMOF into the lower-lying LUMO of the (typically electron-deficient) analyte, and FRET, in which overlap between the emission spectra of the LMOF and absorbance spectra of the analyte permits transfer of excitation energy from the LMOF to the analyte, where it decays non-radiatively. While direct orbital overlap between LMOF and analyte molecules is required for charge transfer, FRET can take place over longer distances on the nanometer scale, and so requires only that the analyte be present in or near the LMOF's pore.[36] Emission enhancement can occur through a similar mechanism, with photoexcited electrons from the higher-lying analyte LUMO transferred into the lower-lying LMOF LUMO.

In either case, modulation of emission intensity from the LMOF requires specific relationships between the LUMO energy levels of the target analyte and LMOF, or spectral overlap between the LMOF emission and analyte absorbance. Using a chromophoric ligand-based strategy to prepare LMOFs with LC-based emission is useful method of designing an LMOF sensor with the appropriate LUMO energy levels or emission wavelength to interact

with a targeted analyte.[25] This strategy entails preparing an emissive ligand based on an organic chromophore with the optoelectronic properties and functionality necessitated by the target analyte, then constructing it into a MOF with d^0 or d^{10} transition metals. These closed d subshell species have relatively low-lying HOMOs (highest occupied molecular orbitals) and high-lying LUMOs that usually preclude their participation in luminescence. The resulting MOF should then possess similar properties (emission and excitation spectra, HOMO and LUMO energy levels) as the initial chromophore.

1.4 LMOFs as Phosphor Materials

Global efforts to improve energy efficiency are important for reducing energy cost and consumption, decreasing carbon dioxide emission and slowing down global warming. A significant portion of global energy is directed towards infrastructure – transportation of goods and people, lighting, and heating/cooling are responsible for the bulk of energy use[37-38]. Improving the energy efficiency of these processes will lead to significant payoffs in global energy savings. Lighting is an especially attractive target, as it accounts for a significant portion of energy use. Developing more efficient lighting technologies has already begun, and addressing its energy efficiency requires less alteration of global infrastructure. Currently, three main types of general lighting technologies exist. Conventional incandescent bulbs generate white light by heating a filament to incandescence. Fluorescent bulbs function by ionizing mercury vapor through the use of an electric current, which produces UV radiation. This UV radiation excites a phosphor material on the interior surface of the bulb, which emits white light. Solid state lighting based on light-emitting diodes (LEDs) uses an electroluminescent diode to produce narrow emission peaks, which can be converted into white light in a variety of ways. In multi-chip LEDs, white light is produced by mixing emission from red, green, and blue LED chips. However, using three LED chips drastically increases the cost of these bulbs.

In phosphor-converted white LEDs (pc-WLEDs), phosphors excited by a single-chip LED produce white light, either directly or by combining the emission of the selected chip. There are three main varieties of pc-WLEDs. In the first, a UV-emitting LED chip is used to excite a mix of red, green, and blue phosphor materials to produce white light. The second is similar, with the UV-emitting LED chip exciting a phosphor which directly produces white light. The third common variety is a blue chip based pc-WLED, in which a blue-emitting LED chip is used to excite a yellow phosphor or multi-component phosphors. The combined emissions from the blue chip and phosphor(s) give the white light.

When qualifying the light produced by a lighting device, two important characterization metrics are the color temperature and chromaticity. The color temperature of an emissive material relates the color of light produced to the temperature at which an ideal black body radiator would produce light of the same color. As such, it is only of use when describing light colors produced by black body radiators, from red, through orange and yellow, and into white light. It is most commonly used to indicate whether a bulb produces "cold" blue-white light (higher color temperatures) or "warm" yellow-white light (lower color temperatures), and is provided for most commercial light bulbs. Chromaticity describes the color of light more completely. The international standard method of plotting chromaticity was developed by the International Commission on Illumination (CIE) in 1931, which uses a coordinate system to indicate a specific color (fig. 4).[39] The CIE coordinates of a given light source may be calculated using its spectral power distribution and three color matching functions, allowing the hue of light perceived by the human eye to be determined from spectral data. Of special note is the coordinate (0.333, 0.333), which is ideal white light.

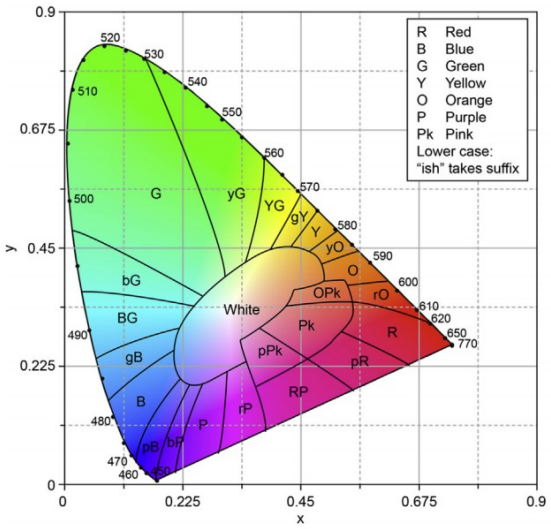

Figure 4. CIE chromatography plot, showing the colors corresponding to each region of the plot.

While LED bulbs are the most energy efficient and longer-lasting general lighting technology, their highest initial cost has slowed their adoption. This is unfortunate, as the US Dept. of Energy has estimated that if the United States switched to entirely LED lighting, over 300 TWh of energy would be saved annually, which is nearly double the amount expected to be generated by wind and solar power generation plants by 2030.[40] As the phosphor materials currently used in WLEDs rely on rare-earth elements (REEs), which contribute significantly to their high cost, developing new, more efficient phosphors materials that have little or no dependence on REEs could reduce the cost of these devices, resulting in faster adoption of the technology and major global energy savings.

LMOFs are an ideal material with which to replace REE-based phosphors, as their excitation and emission properties can be carefully tuned by engineering appropriate metal centers, organic ligands, guest molecules, and structural connectivity. Constructing a framework provides an opportunity to orient and arrange absorber and emitter species for effective luminescence processes. Additionally, studies have shown that the luminescence efficiencies (e.g. internal quantum yield, IQY) of LMOFs/LCPs that exhibit ligand-based

emission can be significantly enhanced by rigidification or immobilization of the ligands to minimize molecular motions such as vibration and rotation that contribute to nonradiative decay. This is especially noteworthy in the case of ligands based on aggregation-induced emitters (AIE phosphors). LMOFs and LCPs provide a unique opportunity to create high quality, precisely tuned phosphors for applications in solid-state lighting technologies.

Chapter 2: Detection of Mycotoxins by a Highly Luminescent MOF

2.1 Introduction

Each year, over one billion tons of food products, or one quarter of the global food supply, are disposed of following colonization by fungi which produce harmful mycotoxins.[41] These mycotoxins are a fungal waste produce which can be extremely toxic to both humans and animals.[42] The most commonly produced variety of mycotoxins are aflatoxins and ochratoxins.[43] Four common varieties of aflatoxins are B1, B2, G1, and G2, while the most common Ochratoxin is Ochratoxin A (OTA). AFB1 is both the most hazardous and the most common aflatoxin, and low-level exposure can induce cancer of the liver.[44,43]

Because of their common occurrence and exceptional hazardousness, detecting mycotoxins in foodstocks is an important food safety application. with the US FDA limiting the allowable concentration of AFB1 in cattle feed to 300 ppb.[45] Detecting mycotoxin is generally done using immunoassays and mess spectrometry, which—while effective—are also prohibitively expensive and technically complex. This limits their applicability in developing areas where mycotoxin poisoning is most common. [46] Developing more economical, practical, and functionally simple detection methods for mycotoxins is therefor of great interest.

As described in chapter 1, optical sensing is both a powerful and simple method of chemical detection which luminescent MOFs (LMOFs) are extremely well suited to. We designed and synthesized the first LMOF for the fast optical detection of a collection of mycotoxins with an exceptional detection limit of 46 ppb.

2.2 Experimental Methods

All reagents are used as purchased unless specified otherwise.

2.2.1 Synthesis of tppe Ligand

Synthesis of the ligand 1,1,2,2-tetrakis(4-(pyridin-4-yl)phenyl)ethane (tppe)[47] began with the reaction of solid 1,1,2,2-tetraphenylethene (tpe) with liquid bromine to produce 1,1,2,2-tetrakis(4-bromophenyl)ethene (Br_4-tpe), which was purified via recrystallization in dichloromethane/methanol. A Suzuki coupling reaction between Br_4-tpe and pyridine-4-boronic acid, catalyzed by palladium (II) acetate, was used to attach the pyridine moiety to the tpe moiety. The final product was extracted with chloroform and purified using column chromatography (stationary phase = silica, mobile phase = 30:1 $CHCl_3$:MeOH).

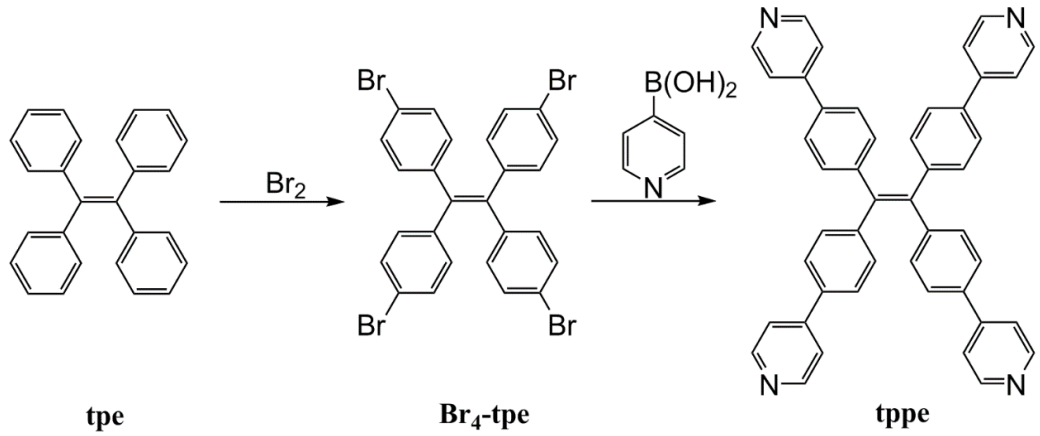

Figure 5. tppe synthetic scheme.

2.2.2 Synthesis of $Zn_2(bpdc)_2(tppe)$ (LMOF-241)

In a 20 mL glass vial, $Zn(NO_3)_2 \cdot 6H_2O$ (0.015 g, 0.05 mmol), biphenyl-4,4'-dicarboxylic acid (H_2bpdc, 0.012 g, 0.05 mmol), and tppe (0.013 g, 0.02 mmol) were added. Then N,N-dimethylacetamide (DMA, 8 mL), dimethyl sulfoxide (2 mL), and isopropanol (2 mL) were added to the mixture. The reaction mixture was kept under ultrasonication until all solids dissolved. The glass vial was sealed and kept at 150 °C for 24 hours. The transparent light yellow needle-shaped crystals were harvested by filtration after the reaction mixture cooled down to room temperature.

2.2.3 Structure Analysis of LMOF-241

Single crystal diffraction data for LMOF-241 were collected on a Bruker APEXII CCD diffractometer using the synchrotron source (λ = 0.7749 Å) at the Advanced Light Source 11.3.1 Chemical Crystallography beamline. All non-hydrogen atoms were refined anisotropically; hydrogen atoms were placed geometrically, constrained and refined with a riding model. The unresolvable electron density from the void space in the structure was removed by SQUEEZE. The powder X-ray diffraction (PXRD) patterns were collected on a Rigaku Ultima-IV diffractometer using monochromatic Cu Kα radiation (λ= 1.5406 Å). Data were collected between a 2θ of 3 – 50° with step size of 0.02° at scanning speed 3.0°/min (Table 1).

Table 1. Single crystal data of LMOF-241

Compound	LMOF-241
Formula	$C_{111}H_{72}N_6O_{12}Zn_3$
M	1877.85
Crystal system	Monoclinic
Space group	C 2
a/Å	44.091(2)
b/Å	25.4060(14)
c/Å	17.1248(9)
α/°	90
β/°	91.176(4)
γ/°	90
V/Å^3	19178.7(17)
Z	4
Temperature/K	260(2)
λ (radiation wavelength)/Å	0.7749
D (g/cm^3)	0.650
Reflections collected	83865
R1[a] [I > 2σ(*I*)]	0.0598
wR2[b] [I > 2σ(*I*)]	0.1463
Goodness-of-fit	0.983
CCDC No.	1006120

[a] $R1 = \sum \left| F_o - F_c \right| / \sum \left| F_o \right|$

[b] $wR2 = \sum [w(F_o^2 - F_c^2)^2] / w(F_o^2)^2]^{1/2}$

2.2.4 Porosity Characterization of LMOF-241

Gas sorption isotherms were collected on a volumetric gas sorption analyzer (Autosorb-1 MP, Quantachrome Instruments). Ultra-high purity N2 (99.999%) was used for the experiment. Liquid nitrogen was used as coolant to achieve cryogenic temperature (77 K). As-made LMOF-241 (200 mg) was immersed in 15 mL dichloromethane (DCM) in a glass vial for 2 hours, then the supernatant was decanted and 15 mL fresh DCM was replenished. This process was repeated 6 times. About 150 mg DCM exchanged sample was outgassed at 333 K overnight under dynamic vacuum and the subsequent degassed sample (LMOF-241') was used. The N2 isotherm was collected in a pressure range from 10^{-7} to 1 atm at 77 K. Surface area was analyzed using Autosorb v1.50 software. The Brunauer–Emmett–Teller (BET) surface area of LMOF-241' is 1268 m^2/g.

2.2.5 Computational Study of LMOF-241 and Mycotoxins

To quantitatively measure the interactions between LMOF-241 and Aflatoxin B1 and B2, a simulation of mycotoxin loaded LMOF-241 structures was performed, and configurations with closest analyte-MOF contacts were chosen for each toxin. The Materials Studio Sorption package was used to simulate adsorption of Aflatoxin B1 and B2 into the pores of LMOF-241, generating an optimized toxin-loaded MOF structure. The simulation utilized the GCMC method and Burchard Universal Force Field, and was performed at room temperature for 107 equilibirum steps. The LMOF-241 supercell used in the simulation was composed of 2x3x3 unit cells (approximately 90x75x50 Å). Six and five configurations, chosen on the basis of close contact of toxin with the MOF, were selected for Aflatoxin B1 and B2 respectively. A fragment of the overall structure (toxin@LMOF-241) was taken for Extended Hückel calculations. The LMOF-241 fragments were chosen such that the closest PBU to the

toxin molecule was included, with all Zn clusters full coordinated. H atoms were manually added to any non-coordinated carboxylate groups for charge balancing purposes.

The electronic properties of LMOF-241 and selected mycotoxins were evaluated using extended Hückel (EH) method.[48-49] A fragment containing a complete LMOF-241 primary building unit (PBU), composed of 1 Zn^{2+}, 2 tppe, and 2 bpdc, was used in the calculations, with dangling carboxylates terminated with hydrogen to ensure a neutral framework.

2.2.6 Optical Characterization

The optical band gap, fluorescence internal quantum yield (IQY), and solid state excitation and emission spectra were measured for LMOF-241 at room temperature in air. Diffuse reflectance data were collected using a Shimadzu UV-3600 spectrophotometer, and the Kubelka-Munk function was used to estimate the optical band gap. IQY measurements were collected using a Hamamatsu C9220-03 spectrophotometer with integrating sphere. Solid state excitation and emission spectra were collected using a Varian Cary Eclipse spectrophotometer.

2.2.7. Fluorescence Titration

Following solvent exchange with DCM to remove the solvent remaining in the structure following its synthesis, LMOF-241 was added to DCM and the mixture was kept under ultrasonication to form a suspension (4 mg/mL), and stock solutions of Aflatoxin B1 (AFB1) Aflatoxin B2 (AFB2), Aflatoxin G1 (AFG1) and Ochratoxin A (OTA) dissolved in DCM were prepared. DCM was used as the solvent because of its photo-inactivity and LMOF-241's stability in it. The fluorescence titration was performed by adding analyte aliquots to the LMOF-241 suspension. The initial photoluminescence (PL) spectrum of the suspension and spectra after each analyte aliquot addition were recorded on a Varian Cary Eclipse

spectrophotometer. The suspension was thoroughly stirred before each PL measurement. Each measurement was repeated three times and the average value was used.

2.3 Results and Discussion

2.3.1 Framework Structure

LMOF-241forms monoclinic crystals with C2 symmetry. The framework has primary building unit metal nodes, with the tetrahedral zinc (II) ion coordinated with carboxylates from two bpdc molecules and two tppe molecules (Fig. 6a). Each individual framework consists of a network of one-dimensional, hexagonal pores oriented along the *c* axis (Fig. 6b). Three of these frameworks then interpenetrate to give the final structure of LMOF-241, with the remaining pores measuring 16.6 Å across.

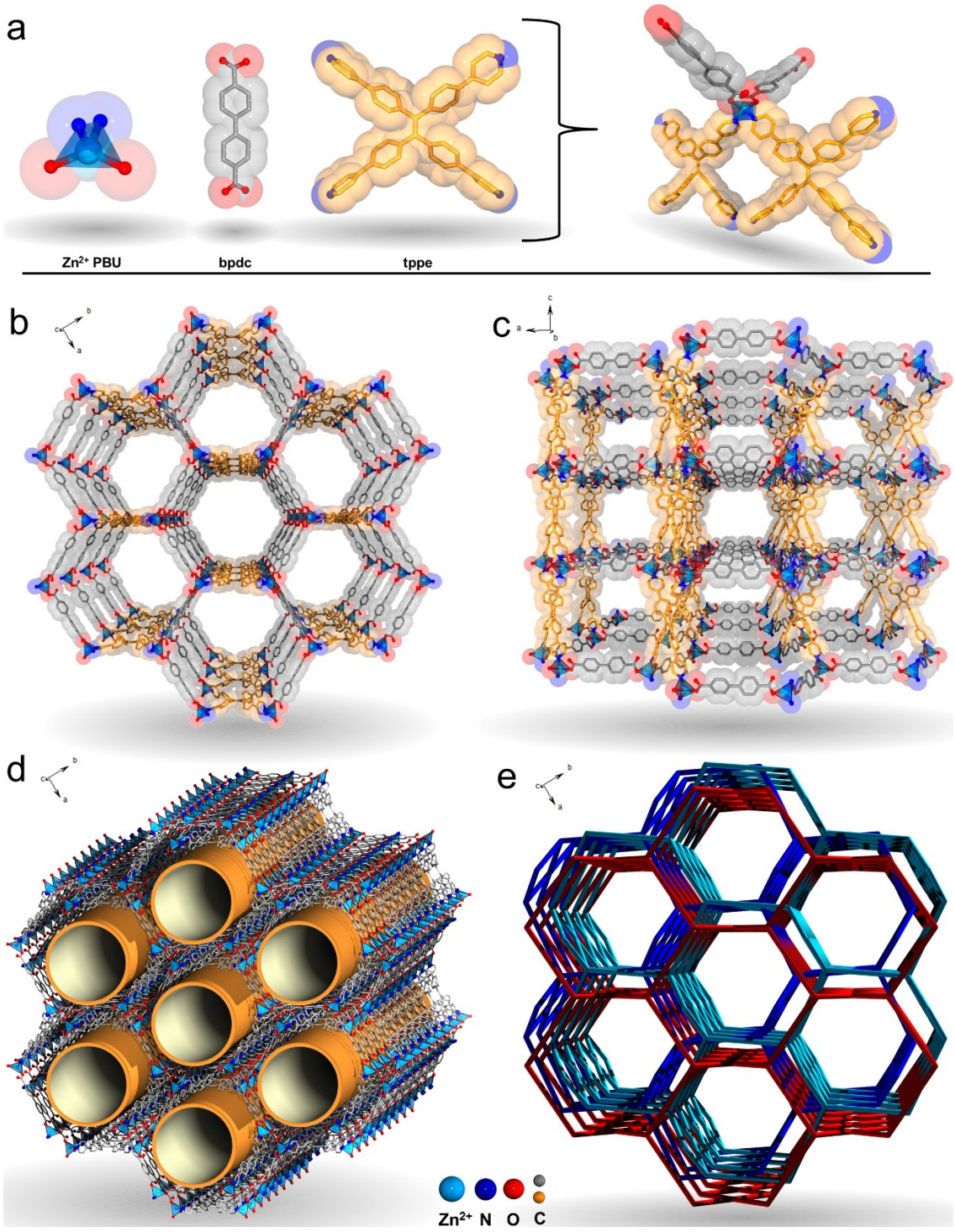

Figure 6. (a) The PBU of LMOF-241, showcasing a tetrahedrally coordinated Zn center bound to two tppe molecules and two bpdc molecules. (b) A single net of LMOF-241 framework viewed along the c -axis, composed of edge-sharing hexagonal channels. (c) A single net of LMOF-241 framework viewed along the b-axis, showing pores that are closed upon the interpenetration. (d) Overall crystal structure demonstrating the 3-fold interpenetration and 1D pore running along the c-axis. (e) LMOF-241 drawn as 2-nodal (4,4)-c net (mog type), with tppe and bpdc simplified as a 4-c node and 2-c node, respectively. The different colors (red, blue, and aqua) indicate the three distinct interpenetrated

networks that form the complete structure of LMOF-241. In all structures, H atoms are omitted for clarity.

2.3.2 Optical Properties

The UV-Vis reflectance spectra of the ligand tppe and LMOF-241 were collected using a Shimadzu UV-3600 spectrophotometer, after which conversion to the Kubelka-Munk function allowed their optical band gaps to be estimated. The estimated optical HOMO-LUMO gaps are 2.3 and 2.6 eV for tppe and LMOF-241, respectively. Photoluminescence excitation and emission spectra were collected for samples of tppe and LMOF-241 at room temperature. Both samples showed strong blue-green emission when excited by UV light (λex = 340 nm), with tppe having an emission maximum at 490 nm, while that of LMOF-241 was slightly redshifted to 500 nm. In designing LMOF-241, we desired to preserve the strong emission from the tppe ligand in the final structure. Specifically, we intended that the immobilization of the chromophore ligand in the MOF framework would not alter the nature of ligand based emission. The Zn^{2+} ion was chosen for this purpose because, as a d^{10} metal with low-lying d-orbital energies, it is known to contribute negligibly in the luminescence of the resulting LMOFs.[47, 50-54]

A Hamamatsu C9220-03 spectrophotometer with integrating sphere was used to determine the IQY of both samples at 360 nm excitation. The values are 76.7% and 92.7% for tppe and LMOF-241, respectively. To the best of our knowledge, the latter represents the highest value reported so far for green-emitting MOFs. The significant increase (16%) in quantum yield is consistent with previous findings, indicating that immobilizing molecular chromophores (such as tppe) into rigid frameworks can improve the material's fluorescence efficiency by eliminating non-radiative relaxation pathways, such as some vibrational and rotational motions.[11, 47, 50-53]The high efficiency makes LMOF-241 an excellent candidate as fluorescence-based sensory material.

2.3.3 Mycotoxin Detection

The mycotoxin detection assay was performed by observing how emission from LMOF-241 changed before and after exposure to the mycotoxin in question. Upon addition of the mycotoxins, the emission intensity of LMOF-241 was quenched. An example of the change in photoluminescence across one complete sensing titration is given in Figure 7b, demonstrating that the degree of quenching increases as a function of AFB1 concentration. The quenching efficiency was quantified using the Stern-Volmer (SV) equation:

$$I_O = K_{SV}[Q] + 1$$

I_O is the initial emission intensity, I is the quenched emission intensity, [Q] is the concentration of the quenching mycotoxin, and K_{SV} is a constant indicating the efficiency of quenching. As shown in Figure 7c, at low concentrations, the I_O/I is linearly proportional to concentration for both AFB1 and AFB2; the slope is the K_{SV}. The K_{SV} plots for AFG1 and OTA are also shown in Figure 7c.

The K_{SV} = 54227 M^{-1} for AFB1, which is among the highest values reported for the known sensory materials. This value is also nearly twice of that of AFB2 (32436 M^{-1}), indicating a high selectivity of LMOF-241 toward AFB1. The detection limit for AFB1 is estimated to be 46 ppb, which is significantly better than 300 ppb, the tolerant level set by the FDA for corn and peanut feeds for beef cattle.[45]

Unlike AFB1 and AFB2, the Stern-Vollmer plots for AFG1 and OTA initially have a negative slope, which bends back upwards at higher concentrations. This is because both AFG1 and OTA are fluorescent under 340 nm excitation while both AFB1 and AFB2 are non-fluorescent under the same conditions. As a result, at low concentration, these two toxins

add to the overall emission intensity, causing a decrease in their SV curves. However, once a certain concentration threshold is reached, interactions between the toxins and LMOF-241 lead to a net quenching. When compared with OTA, AFG1 emits more efficiently and also acts as a stronger quencher, as evident from the shape of both slopes. The concentration of AFG1 at which the PL behavior shifts from enhancing to quenching is also lower OTA's.

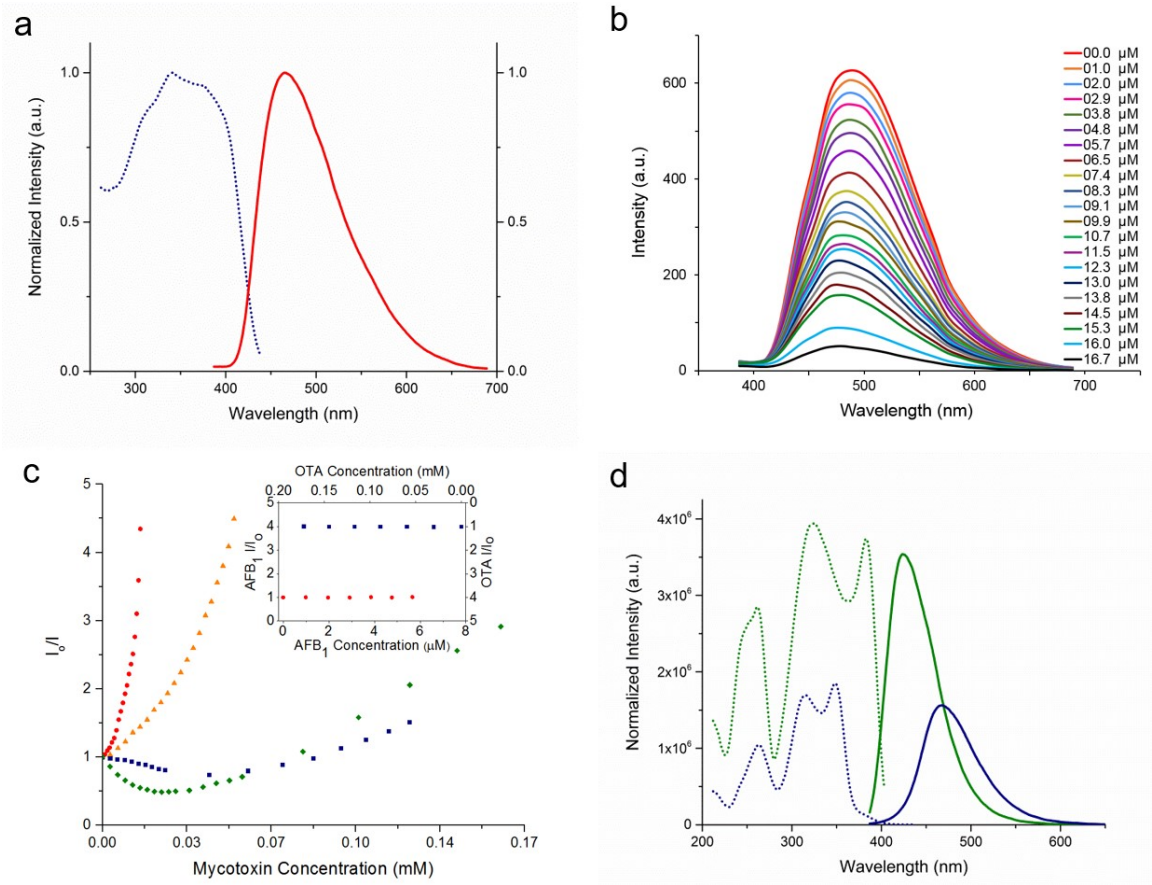

Figure 7. (a) The excitation (dotted blue) and emission (solid red, λ_{ex} = 340 nm) spectra of LMOF-241 suspended in DCM. (b) Emission spectra of LMOF-241 with the incremental addition of AFB1 in DCM, with toxin concentrations given in the key to the right of the figure. (c) The Stern-Volmer curves acquired at λ_{ex} = 340 nm and λ_{ex} = 410 nm (insert) for AFB1 (red dot), AFB2 (orange triangle), AFG1 (green diamond), and OTA (blue square). (d) Excitation (dotted) and emission (solid, λ_{ex} = 340 nm) spectra of AFG1 (green) and OTA (blue) in DCM.

2.3.4 Mycotoxin Detection Mechanism

Emission quenching upon exposure to AFB1 and AFB2 takes place via the photo-induced electron transfer (PET) mechanism.[54] Based on the results obtained from our molecular orbital calculations, the bottom of the LUMO (or CB) energy states of LMOF-241 lies above the LUMO energies of AFB1 and AFB2, allowing an efficient electron transfer from the MOF to both toxin molecules (Fig. 8). In addition, the LUMO of AFB1 is lower in energy compared to that of AFB2, which results in more efficient electron transfer and partially accounts for the stronger observed quenching behavior..

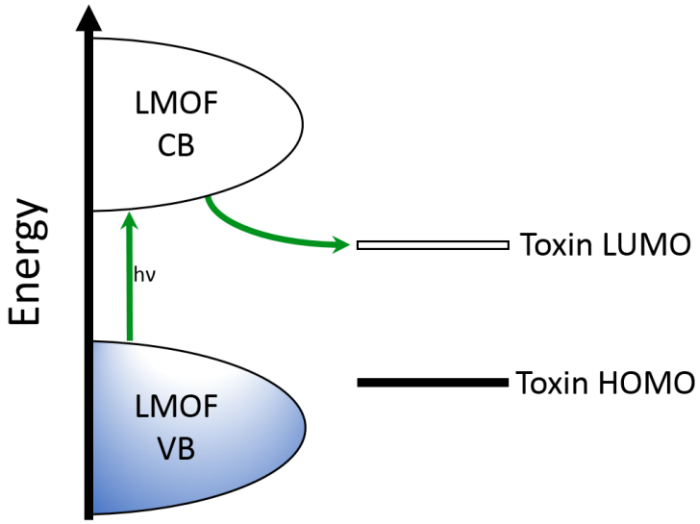

Figure 8. Schematic demonstrating electron transfer from LMOF-241 to mycotoxin LUMO resulting in quenched emission.

The extent of analyte-sensor interactions also plays an important role in the electron-transfer process. With LMOF-241's channel diameter being approximately 16.6 Å, we expect that the aflatoxin molecules (measuring approximately 13.3 Å at their widest) would be able to enter the pores. To confirm this and quantitatively assess the analyte-sensor interactions, we first carried out a structure optimization process on AFB1 and AFB2 loaded LMOF-241, using the Materials Studio Sorption Package, which utilized the GCMC method and Burchard Universal Force Field. Analyte sites located within the LMOF pore with the shortest distances

to the MOF were identified for each of AFB1 and AFB2 by the GCMC simulation method. We then performed overlap population calculations using EH method to quantitatively measure such interactions. The absolute fragment molecular orbital overlap population (SAFMOOP) and absolute reduced overlap population (AROP) between the analytes and the MOF were obtained. The average of the summed absolute orbital overlaps between AFB1 and LMOF-241 is 0.57, whereas that between AFB2 and LMOF-241 is 0.17, indicating that AFB1 interacts significantly stronger with the MOF framework than AFB2. The reduced overlap population follows the same order, with the AFB1 value 1.4 times of that for AFB2. The stronger orbital overlap of AFB1 with LMOF-241 is due to the higher π-conjugation of AFB1, creating more π-type overlap with the conjugate π-orbitals of LMOF-241. As a result, it facilitates a more efficient electron transfer and higher extent of fluorescence quenching.

Energy transfer often contributes significantly in fluorescence quenching and should also be considered. As can be seen in Figure 9a, the spectral overlap between the mycotoxin absorption and LMOF-241 emission is very limited, which hinders the energy transfer from LMOF-241 to AFB1 and AFB2, indicating that it does not likely play a role in the mycotoxin detection. However, when comparing the excitation spectrum of LMOF-241 with the emission spectra of AFG1 and OTA (note: AFB1 and AFB2 are non-emissive), it is apparent that there is significant overlap, especially in the case of AFG1 (Fig. 9c). The energy transfer between the excited toxins (AFG1 and OTA) and LMOF-241 is likely to contribute appreciably to the apparent increase in the fluorescence intensity of LMOF-241 at low concentrations of AFG1 and OTA (Fig. 9c). AFG1 causes a higher degree of increase in LMOF-241 fluorescence intensity, as its emission overlaps more strongly with LMOF-241's excitation spectrum than that of OTA.

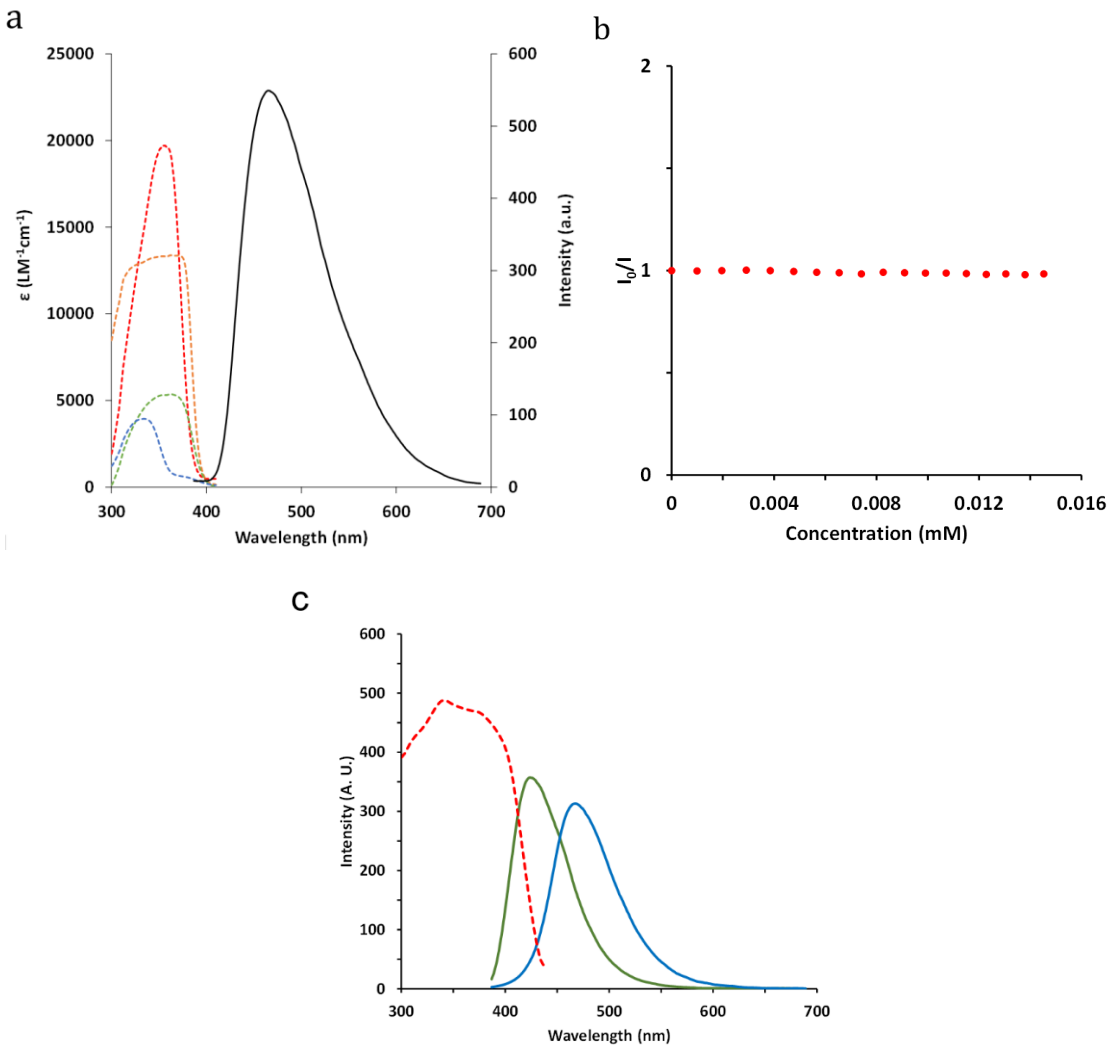

Figure 9. (a) Molar absorptivity of AFB1 (dotted red), AFB2 (dotted orange), AFG1 (dotted green), and OTA (dotted blue), and the emission spectrum of LMOF-241 in DCM (solid black, λ_{ex} = 340 nm). (b) Ksv plot for the titration of a 4 mg/mL solution of tppe with AFB1. (c) Excitation spectrum of LMOF-241 in DCM (dotted red) overlaid on the emission spectra (solid lines, λ_{ex} = 340 nm) of AFG1 (green), and OTA (blue) in DCM.

Also noted in Figure 9a is that all four mycotoxins absorb the excitation energy used in the sensing experiment (λ_{ex} = 340 nm). This suggests that competition between the MOF and the toxins for excitation energy may also contribute to the quenching of LMOF-241's emission. However, it is unlikely that competition for excitation energy plays a significant role in the observed emission quenching, as the toxins are present in extremely low amounts relative to LMOF-241 throughout the sensing titration. Additionally, if competition for

excitation energy was occurring to a significant degree, non-specific quenching of any fluorophores under 340 nm excitation in the presence of the mycotoxins would be observed. Figure 9b demonstrates that luminescence from tppe linker, itself a strong fluorophore, is not affected by titration with AFB1. The strong and continuing decrease in LMOF-241 emission intensity is primarily due to the electron transfer process described above.

Figure 9b also reveals that incorporating the fluorophore into a metal-organic framework is vital for the selective emission quenching to occur. While the tppe molecule is a strong fluorophore, it does not strongly interact with the toxin molecules. By anchoring the fluorophore into a crystalline, porous framework using the metal oxide PBU, we create a well-characterized material that has both an intense emission signal and a strong interaction with the target mycotoxins.

3.4 Conclusions

We have designed and synthesized a new luminescent MOF and investigated its luminescent properties as well as related applications in chemical sensing. LMOF-241 is a blue-green emitting LMOF with an exceptionally high internal quantum yield (92.7%). We have demonstrated for the first time the use of this compound for the effective and selective optical detection of mycotoxins via a luminescence quenching mechanism. LMOF-241 is capable of quickly and efficiently detecting and differentiating several major Aflatoxins and Ochratoxin A and is most sensitive towards Aflatoxin B1. With a detection limit of 46 ppb, LMOF-241 makes one of the best performing luminescence-based chemical sensors to date. We have also studied the electronic properties of LMOF-241 and the selected mycotoxins by theoretical methods. A possible detection mechanism via electron, rather than energy, transfer processes is elucidated. These results suggest that LMOFs have immense potential as simple, low-cost, easily-portable and readily-available luminescence-based sensors for the detection of

biochemical hazards such as toxins and other toxic molecular species, which can be particularly useful for developing countries. This study opens a new direction for practical applications making use of multifunctional MOFs.

Chapter 3: Chromophore-based LMOFs as Lighting Phosphors

3.1 Introduction

There are a variety of strategies that may be used in designing an LMOF for applications as a lighting phosphor, as the wide variety of possible LMOF luminescence mechanisms allows for a wide degree of tunability. However, complex luminescence mechanisms make rational design difficult. With this in mind, the design of LMOFs with ligand-centered emission is ideal for phosphor applications, as it builds upon the significant work done in building organic phosphors. Our strategy to develop organic chromophore-based MOFs is centered on the following consideration: By using chromophoric ligands in the synthesis, highly luminescent metal-organic frameworks (LMOFs) can be constructed that not only can maintain the emission from their ligands but also enhance and tune their emission proper-ties. LMOF quantum yields (QYs) can be higher than their chromophoric ligands because their rigid structures limit the molecular vibrations, torsions, and rotations that often lead to nonradiative excitation decay in the molecular chromophore. In addition, binding chromophores into a rigid framework can improve their thermal stability. Third, including a second ligand in the framework construction may contribute to fine-tuning of emission energy and color. Finally, as many MOFs are porous, it also provides an opportunity to tailor chromophore emission via host-guest interactions.

3.2 Overview of LMOF Design and Synthesis

3.2.1 LMOF-231

In order to design a high performing LMOF, we began by selecting a strongly emissive organic chromophore that could be functionalized with carboxylate groups to provide binding sites for its eventual construction into a framework structure. Our starting point was the

chromophore tetraphenylethene (tpe), which is well-known to fluoresce through aggregation-induced emission (AIE).[55-57] An AIE chromophore was initially chosen because it was known that restricting the molecular movement available to the chromophore would result in markedly improved luminescent efficiency (such a restriction should occur upon incorporation into a framework); however, this process is generalizable to non-AIE chromophores as well.[58]

Table 2. Calculated HOMO/LUMO energy levels and estimated band gap of chromophores, co-ligands, and LMOF fragments.

Species	HOMO (eV)	LUMO (eV)	dE (eV)
H_4tcpe	-6.40	-2.68	3.72
H_4tcbpe	-5.87	-2.46	3.41
H_4(tcbpe-F)	-6.10	-2.68	3.42
tppe	-6.03	-2.25	3.78
btc	-8.19	-2.53	5.66
azpy	-7.15	-3.34	3.81
bpe	-7.24	-1.17	6.07
3 fragment	-6.01	-2.48	3.53

One drawback of using tpe as the chromophore in constructing an LMOF is its high emission energy.[59] As described above a blue-excitable, yellow-emitting LMOF would be preferable for use in PC-WLEDs, and the chromophore emission should be consistent with that goal. In order to shift the emission into the yellow region, DFT calculations were performed to estimate the impact of structural changes to the tetracarboxylated tpe chromophore tetrakis(4-carboxyphenyl)ethylene (H_4tcpe) on its emission energy (table 2). These calculations indicated that the extension of each H_4tcpe arm by an additional phenyl ring should redshift the molecule's emission energy. This led to the synthesis of a yellow chromophore 1,1,2,2-tetrakis(4-(4-carboxy-phenyl)phenyl)ethene (H_4tcbpe) (fig. 10). As desired, H4tcbpe exhibits strong yellow emission at 540 nm, with a high quantum yield of 70.3% under 365 nm excitation (fig. 11).

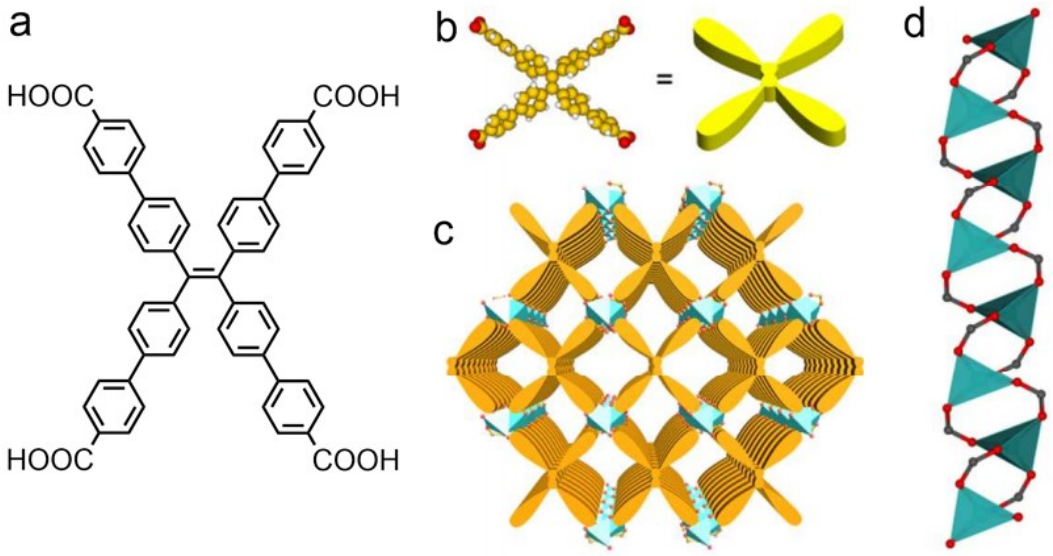

Figure 10. (a) The structure of H4tcbpe. (b) The simplified representation of the tcbpe ligand. (c) The structure of 1', viewed along the c axis, demonstrating the pi-pi stacking of the tcbpe ligand. (d) A view of the tetrahedrally-coordinated Zn infinite PBU, with two carboxylate groups bridging between each of the Zn^{2+} ions, viewed from the b axis. The Zn^{2+} ion is the blue tetrahedron, oxygen atoms are red, and carbon atoms are grey.

Finally, in designing a LMOF with chromophore-based emission, it was important that the metal ions used in constructing the framework do not interfere with the chromophore's optical properties. The Zn^{2+} ion was chosen for this purpose, as density of states (DOS) calculations indicate that the fully occupied 3d subshell lies far below the valence band (VB) region, preventing the metal ion from participating in MOF luminescence.[53, 60-61]

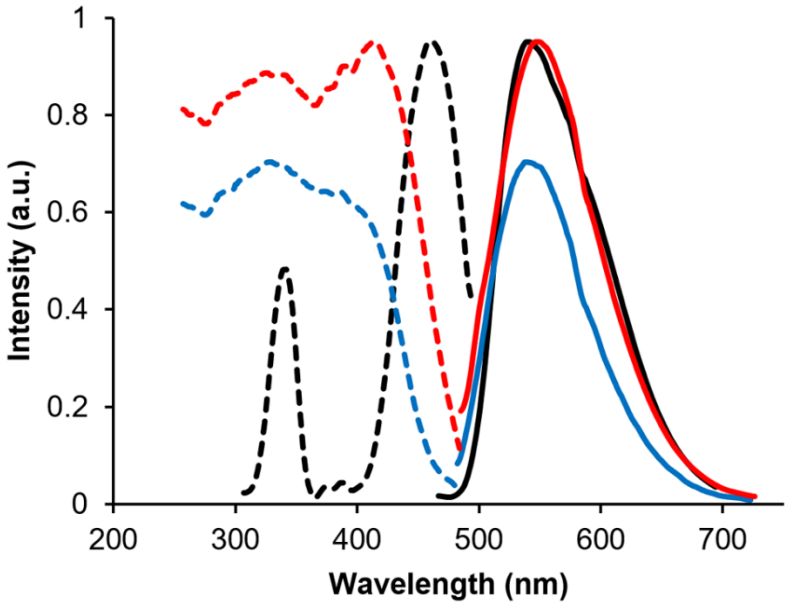

Figure 11. The excitation (dotted) and emission (solid) spectra for the H4tcbpe chromophore (blue), 1' (red), and the commercial phosphor YAG:Ce (black). Peak emission and excitation intensity is scaled to internal quantum yield.

LMOF-231, with the formula Zn_2(tcbpe)·xDMA (1), was synthesized in solvothermal conditions; 0.3 mmol $Zn(NO_3)_2 \cdot 6H_2O$ reacted with 0.03 mmol H_4tcbpe in 2 mL DMA at 120 °C for 48 hours.[62] The residual solvent molecules were then removed by heating under vacuum at 100 °C overnight to give 1', with structural stability confirmed via powder X-ray diffraction. The structure is composed of an infinite zinc-carboxylate primary building unit (PBU) running in the c direction, with stacked columns of tcbpe molecules bridging four zinc-carboxylate chains. The zinc ions are tetrahedrally coordinated, with two carboxylates bridging between each Zn^{2+} ion and its two neighboring ions. The tcbpe layers are closely packed, with interlayer H-H distances between 2.4 and 3.2 Å (fig. 10).

1' has exceptional optical properties; its performance clearly demonstrates the value of incorporating the H_4tcbpe chromophore into a met-al-organic framework. While maintaining the H_4tcbpe's desirable emission energy with only a slight redshift to 550 nm, the immobilization of the molecule enforced by the framework increased the internal quantum

yield from 70.3% under 365 nm excitation for the bulk chromophore to 82.5% for the solvated framework 1 by preventing phenyl ring rotation and C=C bond torsion at the central ethene moiety, which dominate non-radiative excitation decay pathways in tpe-based chromophores.[63] Outgassing to yield 1' eliminates emission-quenching due the solvent molecules, further increasing the internal quantum yield to 95.1% under 365 nm excitation and 76.4% under 455 nm excitation, which is competitive with the commercial phosphor YAG:Ce (fig. 11).

In addition to improving the chromophore's optical qualities, incorporating H_4tcbpe into a metal-organic framework significantly enhanced its thermal stability, as indicated by thermogravimetric (TG) analysis. While molecular H_4tcbpe began to decompose around 340 °C, 1' remained thermally stable until about 450 °C.

3.2.2 LMOF-241

In addition to carboxylate-based chromophores like H_4tcbpe, chromophores with appropriately positioned pyridine groups (and other nitrogen-based groups) can also be incorporated into LMOFs. However, in order to construct a neutral framework using a pyridine-based ligand, a secondary carboxylate-based ligand is needed for charge balancing.

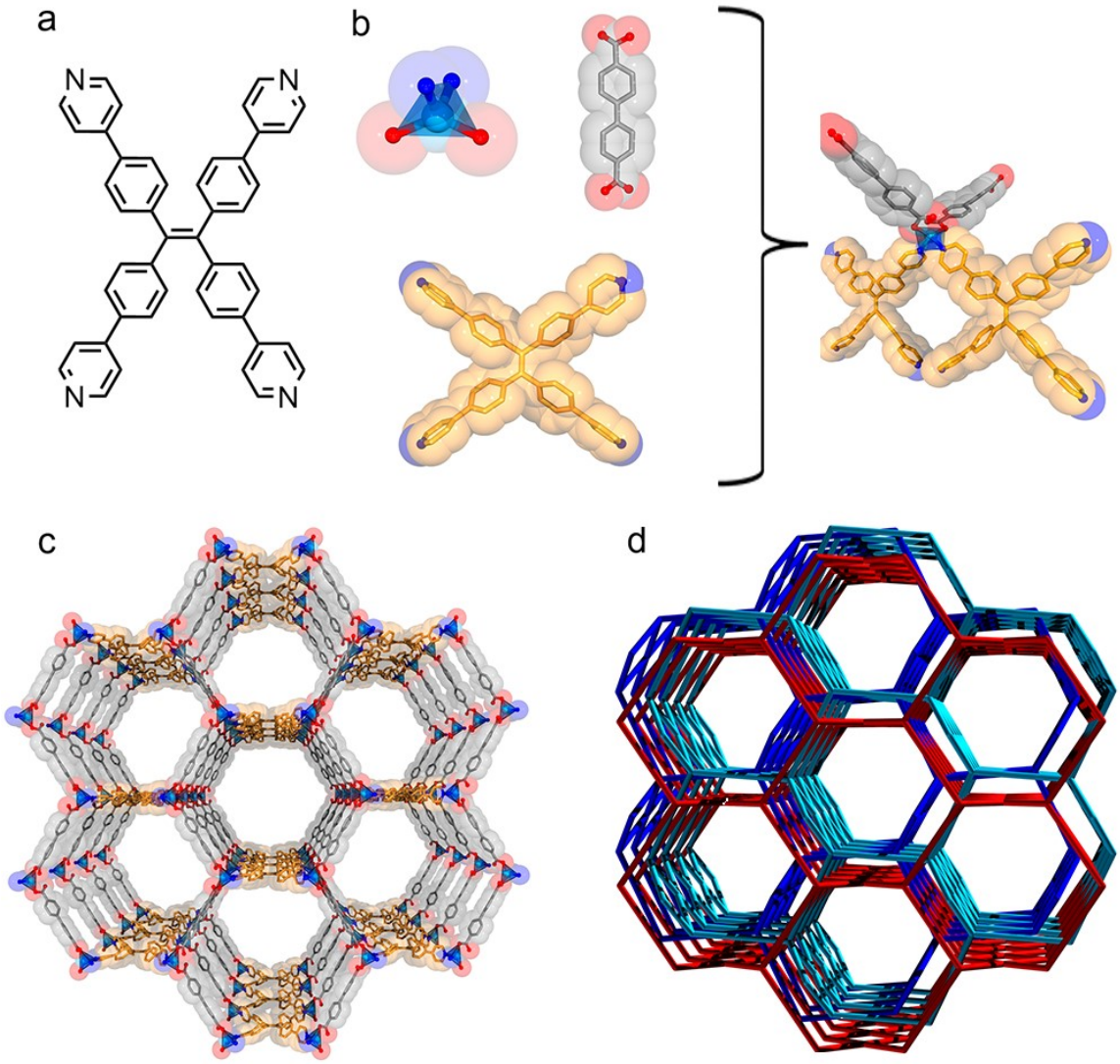

Figure 12. (a) The structure of the chromophore tppe. (b) The tetrahedral Zn2+ ion, bpdc co-ligand in grey, and tppe in gold combining to form the PBU. (c) Structure of a single LMOF-241 framework, with hexagonal channels running along the c axis. (d) Three distinct LMOF-241 frameworks which interpenetrate to form the complete structure. Color scheme: key: C, grey or gold; N, blue; O, red; Zn, aqua.

We constructed an example of this type of LMOF using the pyridine derivative of H_4tcbpe, which is 1,1,2,2-tetrakis(4-(pyridin-4-yl)phenyl)ethene (tppe) (fig. 12), synthesized according to a method described in chapter 2.[64] Bulk tppe emits at 490 nm under 340 nm excitation, with an internal quantum yield of 76.7% The secondary carboxylate ligand chosen for this structure is [1,1'-biphenyl]-4,4'-dicarboxylic acid (bpdc). As observed with 1', the

emission from the chromophore tppe is preserved in 2 with only a slight redshift of 10 nm (from 490 nm to 500 nm), while the internal quantum yield is in-creased from 76.7% to 92.7% under 340 nm excitation (fig. 13).

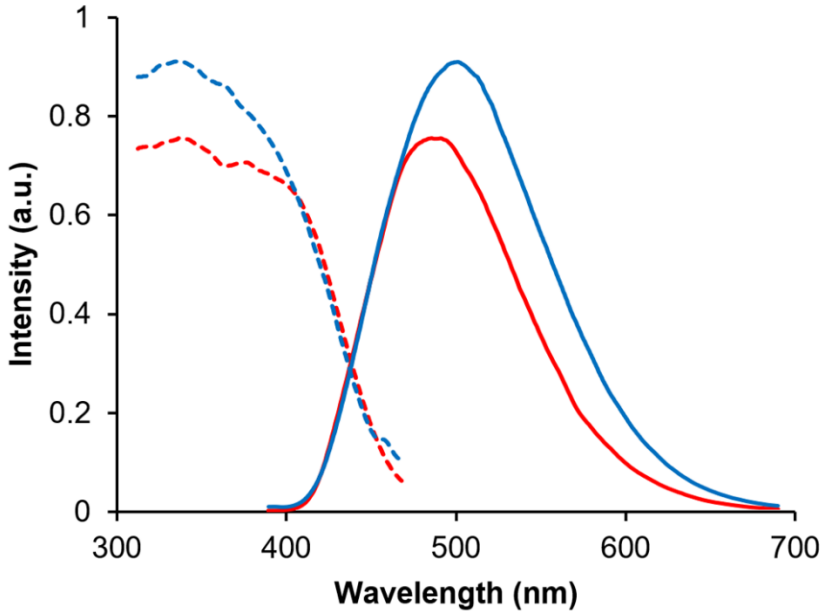

Figure 13. The excitation spectra (dotted) and emission spectra (solid) for the tppe chromophore (red) and 2 (blue). Peak intensity is scaled to internal quantum yield.

3.2.3 LMOF-302

In order to investigate the impact of structural changes on chromophore performance, we sought to incorporate pyridine-based co-ligands intro structures containing the fluorinated H_4tcbpe analog, H_4tcbpe-F (fig. 14). Being fluorinated at the ortho position relative to the carboxylic acid group, it was hoped that the fluorine would moderately reduce electron density on the carboxylate groups, thereby reducing the electron density available for coordination to the Zn^{2+} ions, making the Zn^{2+} in turn more amenable to coordination with the pyridine lone pair. Additionally, DFT calculations indicated that while functionalization with fluorine would decrease the chromophore's HOMO and LUMO energy levels, the chromophore's HOMO/LUMO gap should be essentially unchanged (table 1). As expected, the fluorinated

ligand fluoresced at 540 nm under 455 nm excitation, which is identical to the non-fluorinated ligand. However, while the emission energy was unchanged, the internal quantum yield of H_4tcbpe-F is only 46.5% under 455 nm excitation, as compared to 62.3% for H_4tcbpe. Despite this decrease, the H_4tcbpe-F chromophore is still an effective model with which to study structural effects on chromophore behavior.

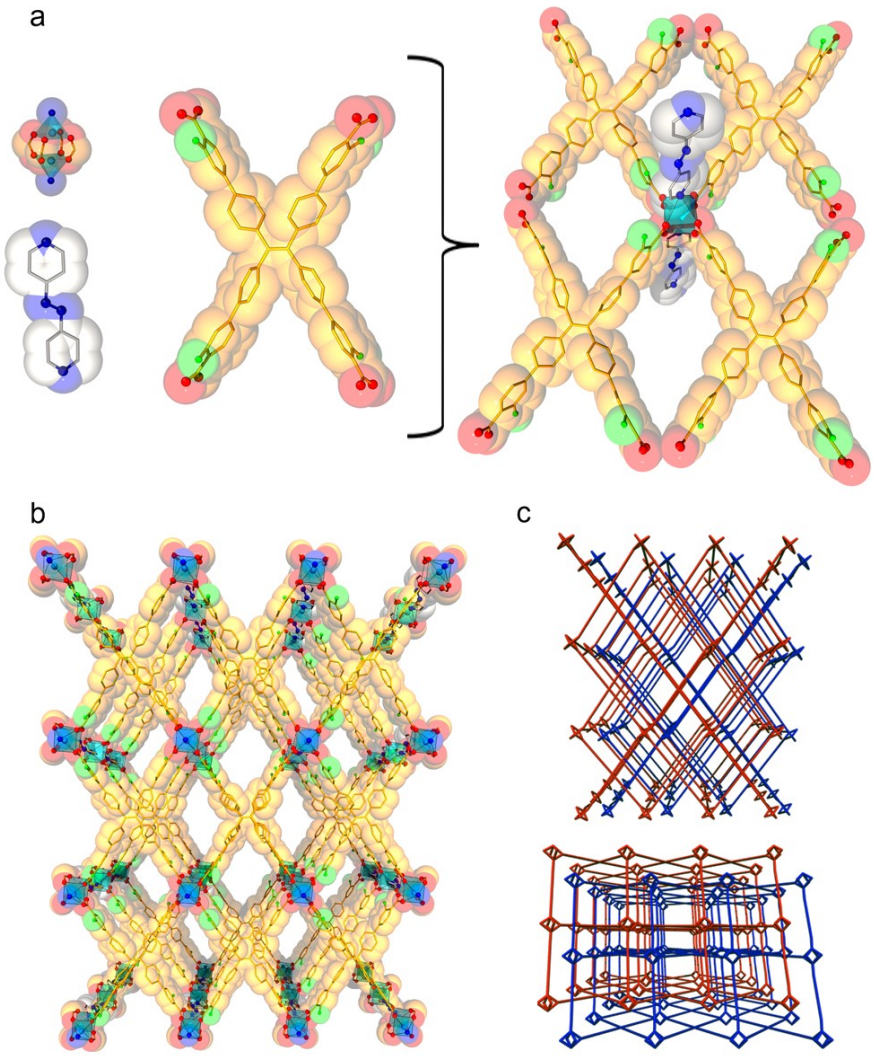

Figure 14. (a) Zinc paddlewheel (top left), azpy co-ligand (bottom left), and tcbpe-F fluorophore combining to form a fragment of 4. (b) Structure of a single framework in 4, viewed along the b-axis.

(c) Two identical frame-works interpenetrate to form the complete structure of 4, viewed along the b (top) and c (bottom) axes. Color scheme: key: C, grey or gold; N, blue; O, red; F, green; Zn, aqua.

Following synthesis of H_4tcbpe-F, the first pyridine ligand to be incorporated into a structure with H_4tcbpe-F was 4,4'-azopyridine (azpy). 0.05 mmol azpy was introduced into solution with 0.05 mmol H_4tcbpe-F and 0.10 mmol $Zn(NO_3)_2 \cdot 6H_2O$ in DMA. Following 48 hours at 100 °C, the non-fluorescent crystalline product LMOF-302 (4) with formula Zn_2(tcbpe-F)(azpy) was recovered. Single crystal X-ray analysis showed that the resulting structure is formed by two interpenetrated frameworks, which are related to each other through a center of inversion. Each framework consists of the classic Zn^{2+} paddlewheel SBUs, in which two Zn^{2+} atoms are bridged by four roughly orthogonal carboxylate groups from tcbpe-F. These SBUs are each coordinated to four tcbpe-F molecules, which are in turn coordinated to four more SBUs (etc.), forming a two-dimensional sheet in the ac plane. These sheets are linked by pillaring azpy ligands in the c direction, which coordinate through the pyridyl nitrogen and connect each of the SBUs to those above and below (fig. 14).

As shown by thermogravimetric analysis (TGA), 4 decomposes at approximately 330 °C, which is 120 °C lower than 1. A decrease in thermal stability is to be expected when comparing 1 and 4, as the SBUs in 4 contain Zn-N bonds, which are relatively weaker than the Zn-O bonds which make up the entirety of ligand-metal bonds in 1.[65] Additionally, the high degree of tcbpe pi-pi stacking in 1 increases its thermal stability, whereas gaps of approximately 5.7 Å separate every two layers of tcbpe-F in 4, limiting the effectiveness of the pi-pi stacking as a thermal stabilization mechanism.

3.2.4 LMOF-304

The second pyridine-based ligand to be incorporated into a structure with tcbpe-F was 1,2-bis(4-pyridyl)ethane (bpe). Un-der the same reaction conditions as 4 (but with bpe replacing azpy), the crystalline product Zn_2(tcbpe-F)(bpe)·nDMA was recovered. PXRD was

used to confirm that the product is isoreticular with 4 (fig. 15). Solvent exchange with acetone was performed to remove residual DMA from the pores, followed by outgassing under vacuum. TGA was used to confirm the full removal of the solvent, giving LMOF-304 (5), with the formula Zn_2(tcbpe-F)(bpe).

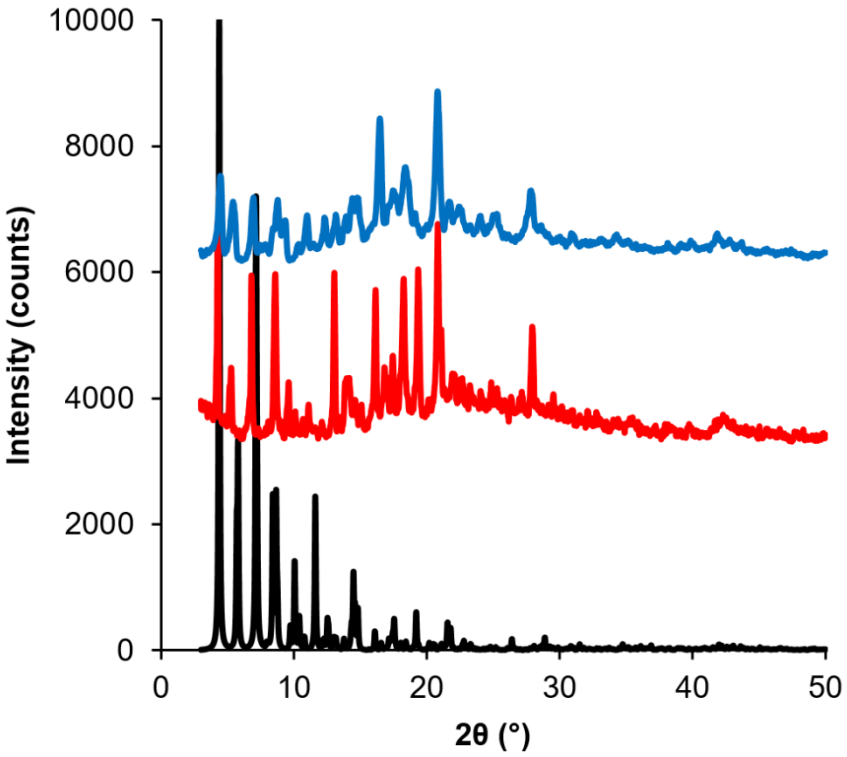

Figure 15. Overlaid PXRD patterns for 4 (red) and 5 (blue). The simulated pattern for 4 is in black.

Unlike 4, 5 is strongly luminescent, with a peak emission of 527 nm and an internal quantum yield of 64.0% under 455 nm excitation (fig. 16). This increase from 46.5% in the fluorinated chromophore H_4tcbpe-F to 64% in 5 is commensurate with the increased quantum yields observed between H_4tcbpe and 1, suggesting that the lower quantum yield of 5 when compared to 1 is due primarily to the lower quantum yield of H_4tcbpe-F, rather than being due to some structural factor. This consistency in the face of structural differences implies that it is possible to significantly alter LMOF structures and connectivity without affecting the base

chromophore luminescence. The result also suggests that introducing a co-ligand can alter the electronic structure and consequently emission energy of a LMOF.

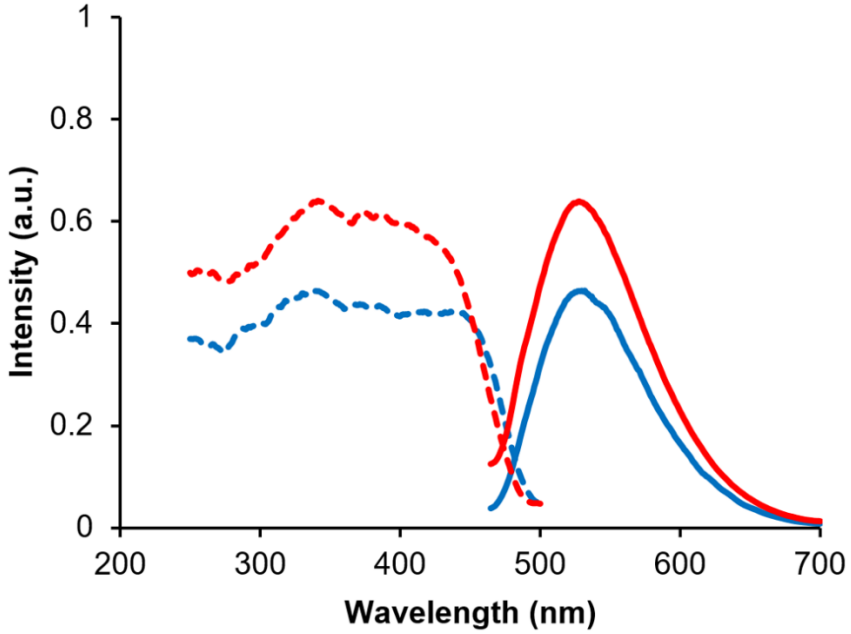

Figure 16. The excitation spectra (dotted) and emission spectra (solid) for the tcbpe-F chromophore (blue) and 5 (red). Peak excitation and emission intensity is scaled to internal quantum yield.

In addition to the positive influences that incorporating a chromophore into a MOF has on fluorescence quantum yield and stability, MOFs can often possess permanent porosity. This presents an opportunity to further influence LMOF emission through loading guest molecules into the structure. In order to investigate the influence that potential host-guest interactions could have on emission from 5, aromatic solvents with varying functional groups were loaded into this LMOF using a solvent-exchange procedure. Under 365 nm excitation, the emission from 5 was tunable based on which guest molecule was present (fig. 17).

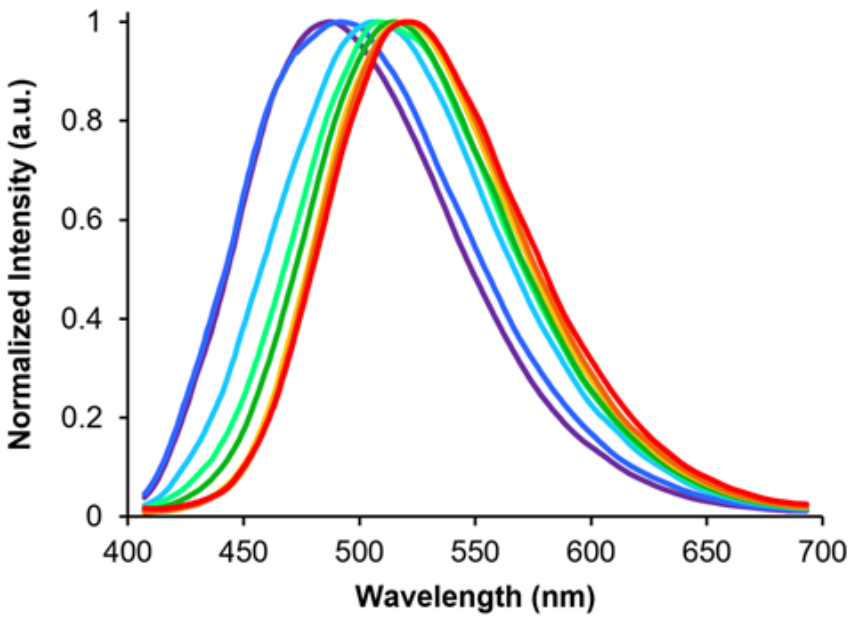

Figure 17. Overlaid normalized emission spectra for guest-loaded samples of 5. In order of decreasing emission energy, the guest molecules are: Butylbenzene (violet), 1,2,4-Trimethylbenzene (blue), p-Chlorotoluene (aqua), p-Xylene (light green), Bromobenzene (dark green), Chlorobenzene (yellow), Toluene (orange), and outgassed 5 (red, no guest molecule).

Interestingly, the electron donating or with-drawing character of functional groups on the guest molecules had little effect on the observed emission shift; instead, guest molecule size appears to have had the largest impact. In the presence of butylbenzene and 1,3,5-trimethylbenzene, emission from 5 was strongly blueshifted to 488 and 489 nm, respectively. A more moderate blueshift was observed in the presence of p-chlorotoluene and p-Xylene, with emission at 508 and 509 nm, while the smallest blueshift was observed in the presence of bromobenzene, chlorobenzene, and toluene, with emission peaks at 517, 519, and 520 nm. This relationship between guest size and emission shifting may be related to the closer interactions that are expected between larger guest molecules and the LMOF pore.

3.3 Conclusions

Chromophore-based LMOFs present an exciting opportunity to develop high-performance, rare-earth free phosphor materials. Upon immobilizing organic chromophores

into a rigid framework, both their luminescence quantum efficiency and thermal stability can be greatly improved. Various LMOF structures can be obtained by incorporating different chromophores, and adjustments to the chromophore emission energy can be achieved through the careful selection of co-ligands. Additionally, the inherent porosity of the LMOF system presents the opportunity to further tune phosphor emission through the interaction with selected guest molecules.

Chapter 4: Tuning QY under Blue Excitation in a Multivariate MOF

4.1 Introduction

We reported the best LMOF candidate for a phosphor material in PC-WLEDs in 2015—LMOF-231, or Zn_2(tcbpe)—which has strong yellow emission with a peak at 550 nm and a quantum yield of 76% under 455 nm excitation, which is the peak emission wavelength for the most common InGa LED chip. This is the highest reported quantum yield for a yellow-emitting LMOF under blue excitation. However, this is still lower than the quantum yield of the current commercially available phosphor YAG:Ce, a cerium-doped yttrium-aluminum garnet, which has a quantum yield of 95% under the same conditions. In order to produce a material which could more effectively rival the performance of YAG:Ce, it was necessary to improve the material's quantum yield under blue excitation. In this work, photoluminescence spectroscopy is used to probe the luminescence mechanism in LMOF-231, and DFT calculations are used to identify a secondary ligand with the appropriate electronic structure to improve the LMOF's quantum yield. Based on the information from these spectroscopic and theoretical studies, a ligand doping strategy is used to incorporate this secondary ligand into LMOF-231, creating LMOF-305, which sets a new record for LMOF PC-WLED phosphors with a quantum yield of 88% under 455 nm excitation and an ideal emission peak of 550 nm.

4.2 Materials & Methods

All materials were used as received from Sigma Aldrich. The chromophoric ligand H_4tcbpe and the chromophoric ligand H_4tcbpe-F (fig. 18), as was LMOF-231.[66-67]

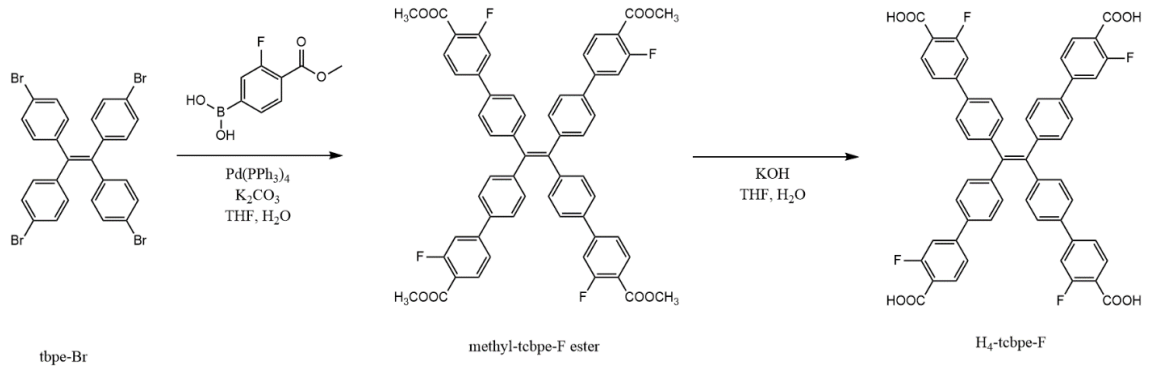

Figure 18. Synthesis of H_4tcbpe-F

LMOF-305 was synthesized solvothermally. H_4tcbpe (0.0305 g, 0.0375 mmol), H_4tcbpe-F (0.0332 g, 0.0375 mmol), and $Zn(NO_3)_2 \cdot 6H_2O$ (0.149 g, 0.400 mmol) were dissolved in a glass vial with dimethylacetamide (DMA, 2 mL). The resulting solution was heated in a reaction oven at 120 ° C for 24 hours, after which the product was collected via filtration as large, slightly yellow translucent crystals. Solvent exchange was performed by immersion in approximately 15 mL ethyl acetate for 24 hours, with the solvent being refreshed every two hours for the first eight hours, after which the sample was heated under vacuum at 50 ° C overnight to give the outgassed product.

For the single crystal analysis, the selected crystal was mounted on MiTeGen® loops in Paratone oil on a Bruker D8 diffractometer equipped with a PHOTON100 CMOS detector and Oxford Cryosystems Cryostream 800 plus, on Beamline 11.3.1 of the Advanced Light Source at LBNL. A sphere of data were collected at 100K using Bruker APEX3 software[68] in shutterless mode with ω rotations at fixed φ values at λ= 0.7749Å, from a channel cut Silicon [111] monochromator. The intensity data were integrated and corrections applied with SAINT v8.34a,[69] absorption and other corrections were made using TWINABS 2012/1.[70] Dispersion corrections appropriate for this wavelength were calculated using the Brennan method in XDIP with in WinGX.[71] The structures were solved with a dual space method with SHELXT

2014/4 and refined using SHELXL 2014/7.[72] Once the refinement had converged, SQUEEZE was used to mask the electron density in the pores.[73]

A Rigaku Ultima IV diffractometer was used to collect all powder X-ray diffraction (PXRD) data. Data collection was performed at room temperature using Cu Kα radiation (λ = 1.5406 Å), scanning across a 2θ range from 3° to 35° with a scan speed of 2° 2θ/min and a step size of 0.2°. A TA Instruments Q5000 was used to perform thermogravimetric analyses (TGA) of all samples. Samples were loaded into a Pt pan and heated under constant N2 flow (20 mL/min) from 30 °C to 600 °C, with the temperature increasing at a constant rate of 10 °C/min. SEM images were obtained using a Zeiss Sigma Field Emission SEM with Oxford INCA PentaFETx3 EDS system. Several crystals were tried, and the best crystal was used. The diffraction pattern showed twinning. Using Cell_now, two orientation matrices were determined. The data were integrated using the two matrices in SAINT. SAINT determined the transformation between the two cells to be -1 0 -1 0 -1 0 0 0 1. TWINABS was used to produce a merged HKLF4 file, for structure solution and initial refinement, and HKLF5 file for final structure refinement. The HKLF5 file contained the merged reflections first component and those that overlapped with this component, which were split into 2 reflections. TWINABS indicated the twin faction to be 50:50. The structure was solved using the HKLF4 file, however the best refinement was given by the HKLF4 file. All non-hydrogen atoms were refined anisotropically. Hydrogen atoms were placed geometrically, then constrained and refined using a riding model. One FLAT comment was used to keep F1' in the plane with is phenyl ring. Once the modelling of the framework was complete attempts were made to locate the solvent molecules (DMA) and water. However, no meaningful molecules could be found in the difference map, so SQUEEZE was used. SQUEEZE reported Solvent Accessible Volume of 6290 $Å^3$ and Electrons Found in S.A.V. to be 1245.

As there is a mixture of solvents used, it was not possible to approximate the amount of solvent, and no solvent was included in the chemical formula.

Table 3. Single crystal data for LMOF-305 at 100 K

Compound	$Zn_2(tcbpe)_{0.8}(tcbpe\text{-}F)_{0.2}\cdot$xDMA (LMOF-305)
Formula	$C_{54}H_{31.02}O_8F_{0.8}Zn_2$
M	953.93
Crystal system	Monoclinic
Space group	C 2/c
a/Å	37.1066(17)
b/Å	31.733(15)
c/Å	11.8903(6)
α/o	90
β/o	99.208(2)
γ/o	90
V, Å3	13533.1(11)
Z	8
Temperature (K)	100
λ(radiation wavelength) Å	0.7749
D, g/cm^3	0.936
Reflections collected	12941
R1[a] [I > 2σ(I)]	0.0807
wR2[b] [I > 2σ(I)]	0.2512
Goodness-of-fit	1.24
CCDC No.	1946919

$$^{a}R1 = \sum \left| F_o - F_c \right| / \sum \left| F_o \right|$$
$$^{b}wR2 = \sum[w(F_o^2 - F_c^2)^2] / w(F_o^2)^2]^{1/2}$$

Steady-state photoluminescence emission and excitation spectra were collected in the solid state using a Varian Cary Eclipse spectrophotometer at room temperature. Diffuse reflectance data were collected at room temperature using a Shimadzu UV-3600 spectrophotometer. Internal quantum yield was measured at room temperature for all samples with a Hamamatsu C9220-03 spectrophotometer, using a 150 W Xenon monochromatic light source and integrating sphere.

DFT calculations were performed on Gaussian 09, using the B3LYP3 hybrid functional and DGDZVP basis set.[74-79] The geometries of all ligand molecules were optimized,

with a frequency calculation performed after geometry optimization to confirm that the calculations resulted in a true minimum.

4.3 Results & Discussion

4.3.1 Structure and Luminescence mechanism of LMOF-231

LMOF-231 or Zn_2(tcbpe) is composed of a zinc-carboxylate chain forming an infinite secondary building unit running in the *c* direction, with each tcbpe^{4-} ligand linking four of these chains linked together. The Zn^{2+} ions display a distorted tetrahedral geometry, with each ion bound to oxygen from four different ligand molecules, and the ligand molecules organized into close-packed columns running in the *c* direction (fig. 19).

Within each ligand, the dihedral angles of the four phenyl rings connected to the ligand's central ethenyl moiety vary. Two phenyl rings bonded to one of the ethenyl carbons having dihedral angles of 42.2° relative to the central ethene, while the two phenyl rings bonded to the other ethenyl carbon have dihedral angles of 58.7° (fig. 19). Each ligand is symmetrically related to its neighbors above and below it in the column through an inversion center; this results in the neighboring phenyl rings on different ligands being arranged in an edge-face-edge fashion, with close H-H interactions (atom-atom distances of approximately 2.4 Å) preventing significant rotation of the phenyl rings in the structure (fig. 19). Additionally, DFT calculations indicated that the lowest energy configuration of a single ligand molecule has ethene-phenyl dihedral angles of 49.4°. The observed displacement from that value supports the identification of rigidifying H-H interactions.

The average layer spacing between ligands within these stacks, determined by simplifying the tcbpe ligand into a 2D rectangular surface with its corners defined by the four carboxylate carbons and measuring the distance separating these surfaces, is 5.4 Å. And since the ligands are arranged in a tilted fashion, the closest centroid-centroid distance between

phenyl rings in neighboring ligands is 5.93 Å, which is distant enough to prevent significant pi-pi interactions that could lead to quenching.[80]

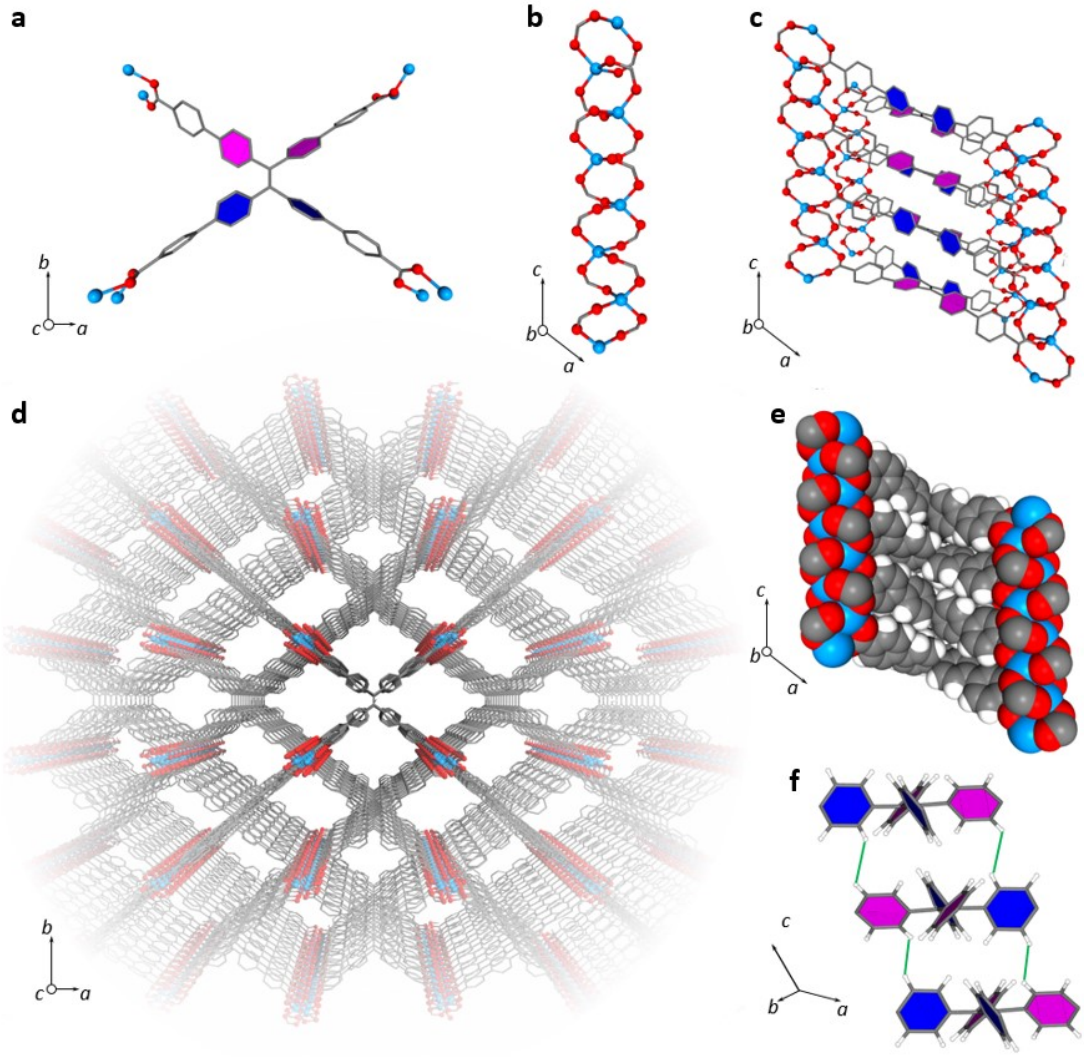

Figure 19. a) A single tcbpe molecule coordinated to eight Zn2+ ions, with the pink-colored phenyl rings having a dihedral angle of 42.2° with respect to the central ethene, and the blue colored phenyl rings having dihedral angles of 58.7° with respect to the centra l ethene. b) A segment of LMOF-231's infinite secondary building unit, which runs parallel to the c axis. c) A section of LMOF-231 viewed along the b axis, showing a single column of tcbpe ligands linking four zinc-carboxylate chains parallel to the c axis. Pink-colored phenyl rings indicate an ethene-phenyl dihedral angle of 42.2°, while blue-colored phenyl rings indicate an ethene-phenyl dihedral angle of 58.7°. d) The complete structure of LMOF-231 viewed along the c axis. e) The structure of LMOF-231 viewed along the b axis using a space-filling model to illustrate the tight packing of the ligand molecules. f) The central tetraphenylethene cores from three neighboring tcbpe ligands within a column, illustrating the edge-face-edge arrangement, with green lines showing close H-H interactions. Pink-colored phenyl rings indicate an ethene-phenyl dihedral angle of 42.2°, while blue-colored phenyl

rings indicate an ethene-phenyl dihedral angle of 58.7°. Hydrogen have been omitted from figures 19a, 19c, and 19d for clarity (Zn = blue, O = red, C = grey, H = white).

LMOF-231 emits yellow light at 550 nm under both blue and UV excitation, with an internal quantum yield of 96% under 420 nm excitation and a quantum yield of 76% under 455 nm excitation.[62] Given the scale of Stokes shift, it is apparent that the absorbance of both 455 nm and 420 nm photons excites an electron from the ground state to a higher energy state than the state involved in emission, after which the electron rapidly relaxes to the emissive state. As the emission energy (fig. 20) is independent of the excitation wavelength, it is likely that electrons excited by both 420 nm and 455 nm relax to the same state before emitting (fig. 21).

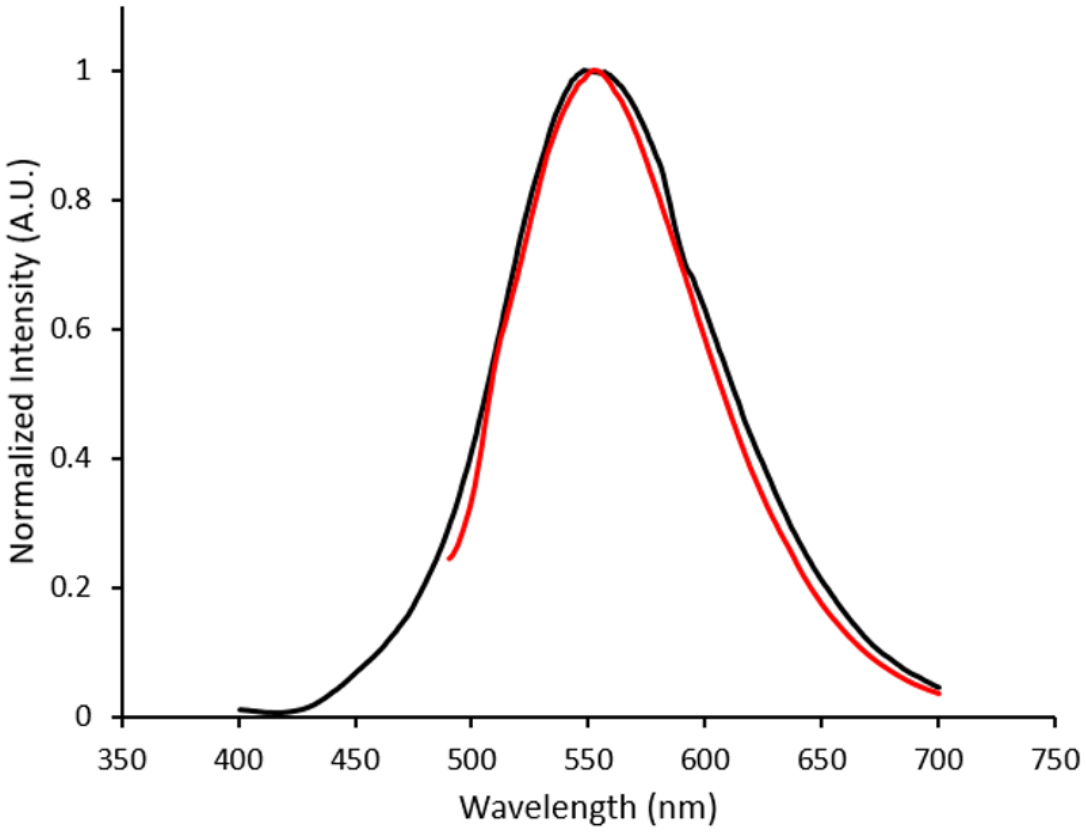

Figure 20. Emission spectra from LMOF-231 under 365 nm (black) and 455 nm (red) emission.

The only clear difference between excitation at 420 nm and excitation at 455 nm is the energy level of the orbital containing the excited electron immediately after absorbance of the

photon, which is higher for the 420 nm photon. However, fact that absorbance of the 420 nm photon resulted in emission with a higher quantum yield suggests that the "higher energy pathway" through which it decays is more efficient than the "lower energy pathway" available to the 455 nm photon (Figure 21).

There are slight differences between the photoluminescent lifetimes of LMOF-231 under 380 nm (UV) and 440 nm (blue) excitation, supporting the existence of these two pathways (table 4). In both cases, the average amplitude weighted lifetime for LMOF-231 is approximately 4 ns—4.14 ns under UV excitation and 3.81 ns under blue excitation—with the total decay being the sum of two processes ($\tau 1$ and $\tau 2$). However, under UV excitation, the faster $\tau 1$ process is more significant, while the slower $\tau 2$ dominates under blue excitation. Additionally, both $\tau 1$ and $\tau 2$ are approximately 1 ns slower under UV excitation than under blue excitation.

Table 4. Room temperature excited state lifetime data for LMOF-231, LMOF-305, and the two ligands under 440 nm excitation.

Excitation	Average amplitude weighted τ	$\tau 1$ (ns)	$\tau 2$ (ns)
UV	4.14 ns	3.02 (56.3%)	5.59 (43.7%)
Blue	3.81 ns	1.98 (35.6%)	4.80 (64.4%)

This suggests that the quantum yield of LMOF-231 under 455 nm excitation could potentially be improved by altering the material's electronic structure such that absorbance of a 455 nm photon activates the "higher energy pathway", mimicking absorbance of a 420 nm photon. One possible way to accomplish this is through an adapted bandgap modulation approach,[47] in which a functionalized tcbpe ligand with an offset HOMO-LUMO energy gap relative to the non-functionalized ligand is introduced into the LMOF as a secondary ligand to create a new dual-ligand MOF. This could achieve the desired change in one of two ways. If the ligand with higher-lying HOMO-LUMO energy levels is excited by a 455 nm photon,

that excited electron could be transferred to the ligand with the lower-lying HOMO-LUMO energy levels at a higher energy state than was possible in the original absorbing ligand (fig. 21c). Alternatively, absorbance of a photon may directly excite an electron between the primary and secondary ligands, with the offset HOMO-LUMO gaps of the two permitting the 455 nm photon to directly excite the electron into the "higher energy pathway" (fig. 21d). Experimentally, these two mechanisms can be distinguished by their optical bandgaps; for the first mechanism, the optical bandgap will be identical to native LMOF-231, while in the second mechanism, a decreased optical bandgap would be observed for the dual-ligand MOF.

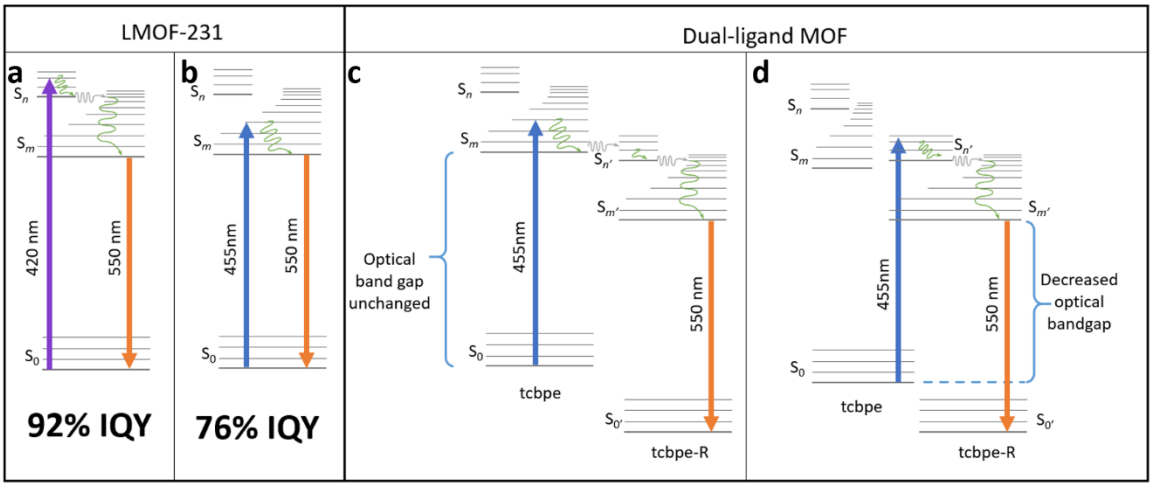

Figure 21. (a) Schematic illustrating a possible fluorescence mechanism for the more efficient "higher-energy pathway" in LMOF-231 following absorbance of a 420 nm photon. (b) Schematic illustrating a possible fluorescence mechanism for the less efficient "lower-energy pathway" in LMOF-231 following absorbance of a 455 nm photon. (c) Schematic demonstrating a possible fluorescence mechanism in a dual-ligand MOF composed of both tcbpe and a functionalized tcbpe with an offset HOMO-LUMO, in which absorbance on a 455 nm photon on one ligand is followed by electron transfer to a neighboring functionalized tcbpe ligand with lower-lying HOMO/LUMO energy levels. (d) Schematic demonstrating a possible fluorescence mechanism in a dual-ligand MOF composed of both tcbpe and a functionalized tcbpe with an offset HOMO-LUMO, in which absorbance on a 455 nm photon results in direct excitation from the non-functionalized ligand to the functionalized ligand, injecting an excited electron directly in to the "higher-energy pathway".

However, for bandgap modulation with a functionalized tcbpe as a secondary ligand to be effective, the luminescence process in the modulated LMOF must involve electron or energy transfer between the primary and secondary ligands. Given the close spacing between

neighboring tcbpe ligands within LMOF-231 and the electron-rich aromatic core of the ligand, it was hypothesized that the luminescence process may involve interactions between neighboring ligands. This suggests that bandgap modulation would be an effective strategy, as long as the functionalized tcbpe ligand replace some of the non-functionalized tcbpe ligands without disturbing the overall framework structure.

4.3.2 Development of Secondary Ligand

Density Functional Theory (DFT) calculations were used as a screening method to identify the functionalized tcbpe-analogue with the appropriate electronic structure, and the version of tcbpe fluorinated at the ortho position relative to the carboxylate was found to meet the design requirements. Calculations indicated that this ligand, 1,1,2,2-tetrakis(4-(3-fluoro-4-carboxy-phenyl)phenyl)ethane or H_4tcbpe-F, possessed HOMO and LUMO energy levels that are approximately 0.23 and 0.22 eV lower than those of H_4tcbpe, respectively. This is ideal, as the offset energy levels in combination with a multi-ligand excitation process should allow the ligand to function as a bandgap modulator for excitation, while the nearly identical HOMO-LUMO energy gap should limit changes to the emission wavelength.

Following synthesis, spectroscopic study indicated that the electronic properties of the fluorine-functionalized ligand were consistent with the relevant calculations. Diffuse reflectance data indicated that the two ligands had nearly identical optical bandgaps, and their excitation and emission spectra were nearly identical as well (Figure 22).

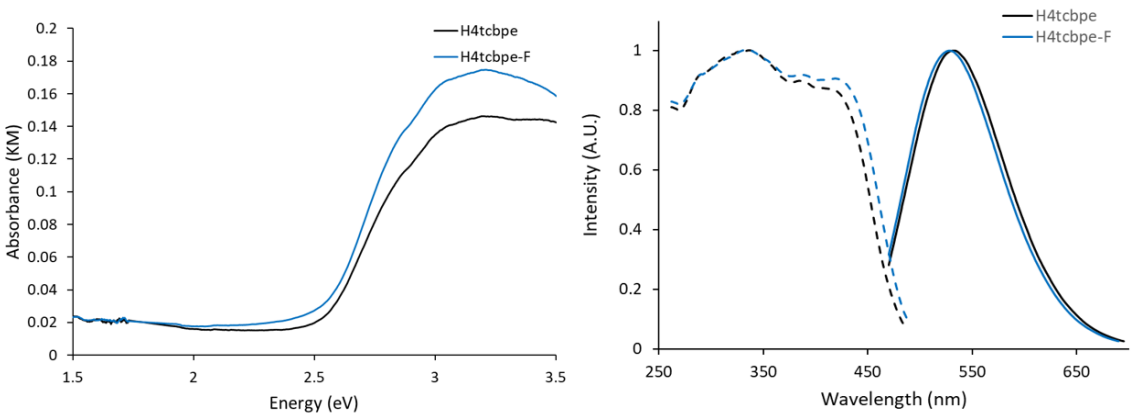

Figure 22. Absorbance-analogue Kubelka-Munk function for H4tcbpe and H4tcbpe-F. b) Excitation (dotted line) spectra for H4tcbpe and H4tcbpe-F at 550 nm emission, and emission spectra (solid line) for H4tcbpe and H4tcbpe-F under 455 nm excitation.

4.3.3 Structure of LMOF-305

The multivariate LMOF-305 or $Zn_2(tcbpe)_{0.8}(tcbpe\text{-}F)_{0.2}$ was synthesized solvothermally with a 1:1 molar ratio for H_4tcbpe and H_4tcbpe-F. The resulting single crystals grew up to 2 mm long, in bloom-like bunches of rectangular crystals. Both PXRD and single crystal analysis confirmed that inclusion of the tcbpe-F ligand did not alter the crystal structure or phase of the LMOF, and fragments of multiple crystals were analyzed using SEM-EDS to ensure that the distribution of tcbpe-F within the LMOF was homogenous (fig. 23). The elemental analysis data confirmed that, although the synthetic ratio between H_4tcbpe and H_4tcbpe-F being 50:50, the resulting LMOF-305 crystal was composed of approximately 80% H_4tcbpe and 20% H_4tcbpe-F. This was consistent with the single crystal data, which yielded a 20% occupancy of F atoms at the relevant crystallographic site.

Despite the relatively low loading of the fluorinated ligand into the LMOF, the replacement of 20% of the tcbpe ligands with tcbpe-F leads to a structure in which approximately 50% of the remaining non-functionalized tcbpe ligands have one neighboring tcbpe-F ligand either above or below within the c-oriented ligand stacks. This assumes that two tcbpe-F ligands rarely neighbor each other, which is reasonable given the low

functionalized ligand loading level and the fact that attempts to further increase the percentage of H_4tcbpe-F within the structure were not successful, which is likely due to steric crowding around the zinc-carboxylate chain in the presence of multiple fluorinated ligands. This is consistent with the thermal stability of LMOF-305 as measured by TGA, which was slightly reduced relative to LMOF-231 and would be expected in the event that the inclusion of the fluorine increased steric strain near the zinc-carboxylate PBU (fig. 23). TG analysis also indicated that less solvent was present within the LMOF pore, which is consistent with the presence of fluorine slightly decreasing the available space (fig. 23).

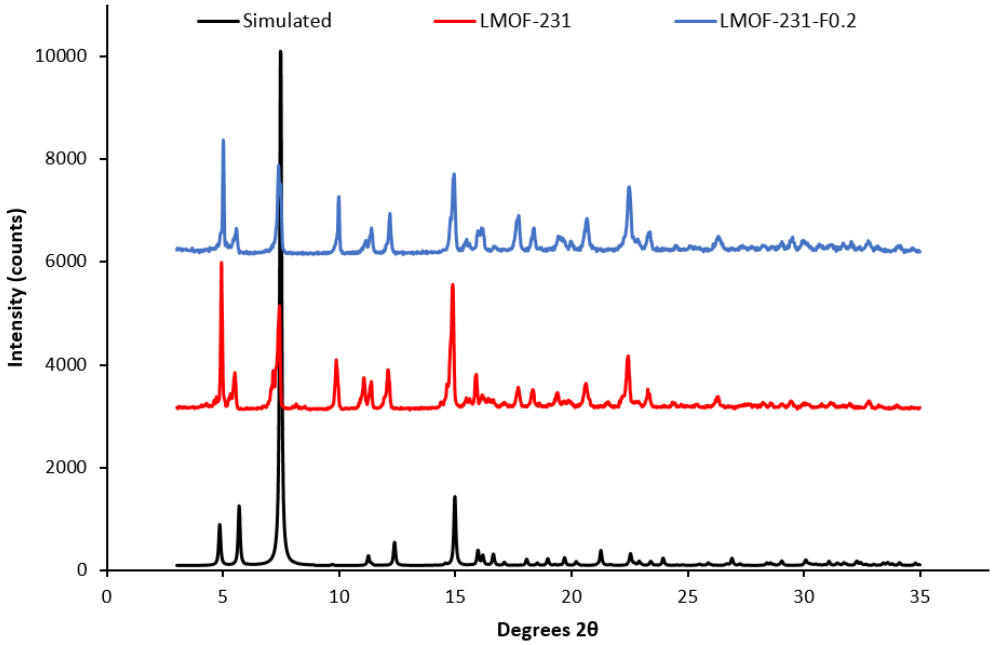

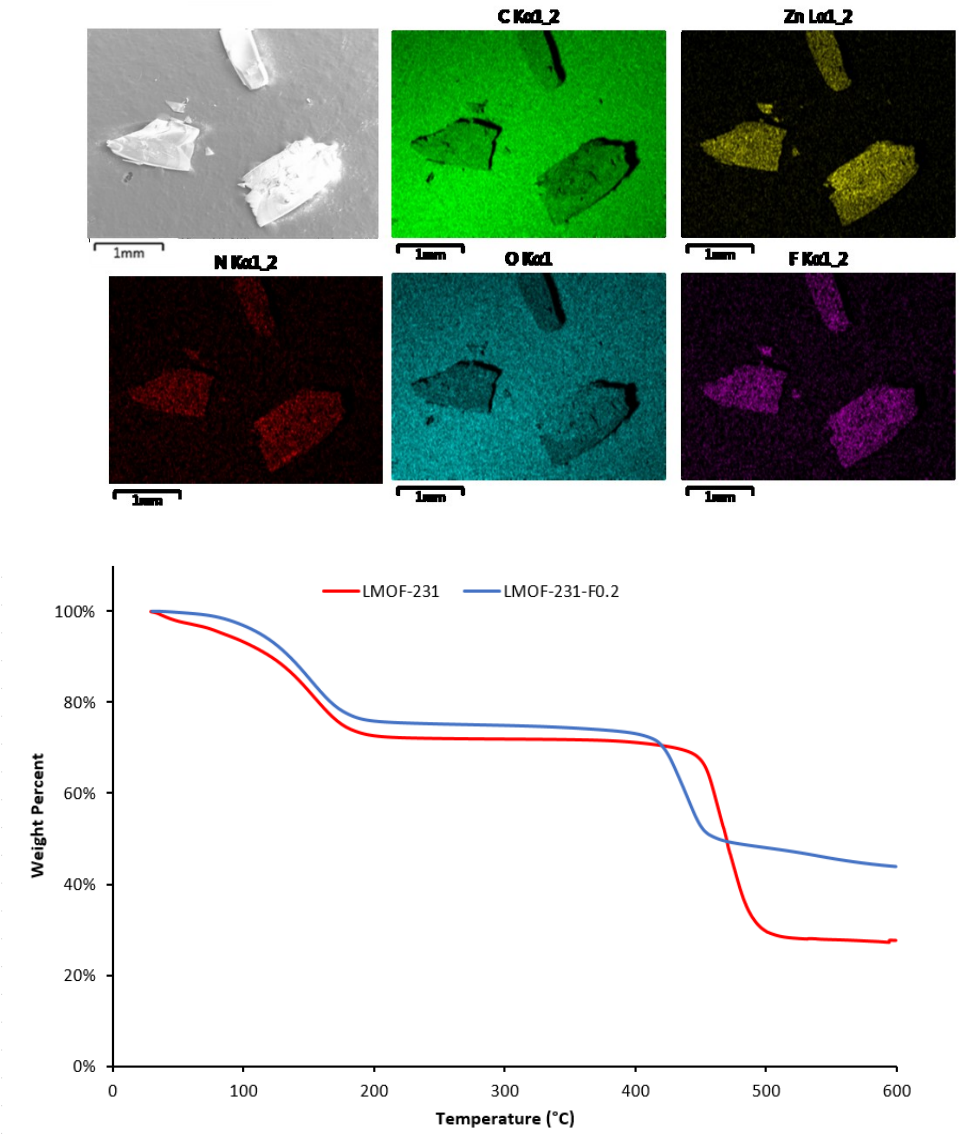

Figure 23. PXRD patterns of LMOF-231 and LMOF-305 overlaid with the simulated PXRD pattern (top), SEM-EDS images of fragments from three different LMOF-305 crystals, mounted on graphite tape, showing the distribution of C, Zn, N, O, and F atoms within the samples (middle), and thermogravimetric decomposition curve for LMOF-231 and LMOF-305 (bottom).

4.3.4. Optical Properties of LMOF-305

Following the successful inclusion of H_4tcbpe-F into the Zn_2(tcbpe) framework at 20% occupancy to give LMOF-305, the material's optical bandgap decreased by approximately 0.3 eV based on diffuse reflectance measurement, and the absorption intensity at 455 nm increased significantly (fig. 24a). The excitation spectrum similarly redshifted to increase

coverage at 455 nm, while changes to the emission spectrum were minor, as desired (fig. 24b). Most importantly, the quantum yield of LMOF 305 under 455 nm excitation increased to 88%, a 12% increase over that of LMOF-231 (76%) under the same excitation energy.

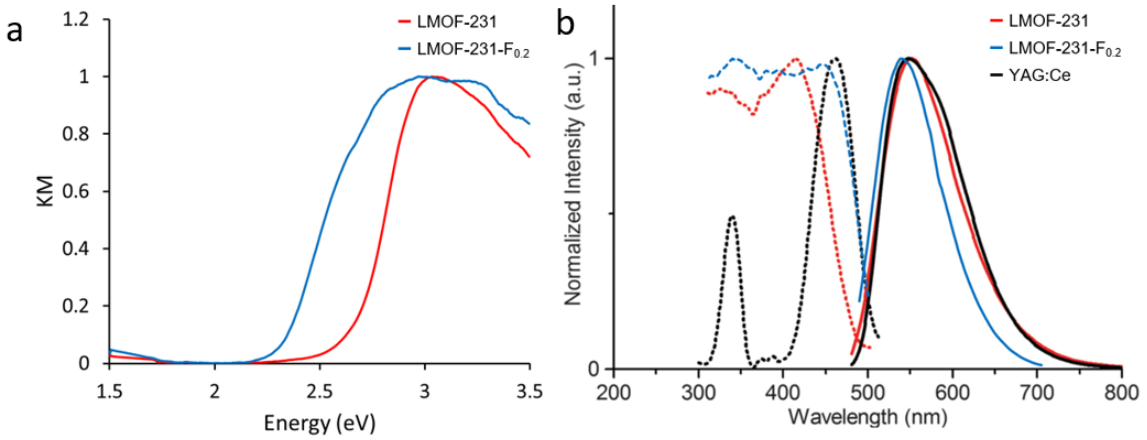

Figure 24. (a) UV-Vis absorbance analogue Kubelka-Munk function derived from diffuse reflectance for LMOF-231 (red) and LMOF-305 (blue). (b) Excitation (dotted) and emission (solid) spectra for LMOF-231 (red), LMOF-305 (blue), and the commercial phosphor YAG:Ce (black). Excitation spectra were monitored at 550 nm emission, and emission spectra were collected under 455 nm excitation.

To probe any differences in emission mechanism, temperature dependent excitation lifetime data were collected for the bulk ligands H_4tcbpe and H_4tcbpe-F, as well as LMOF-231 and LMOF-305, from 77 K to 295 K under 440 nm excitation. Lifetime data and decay curves are given below, in tables 5-8 and figures 25-28.

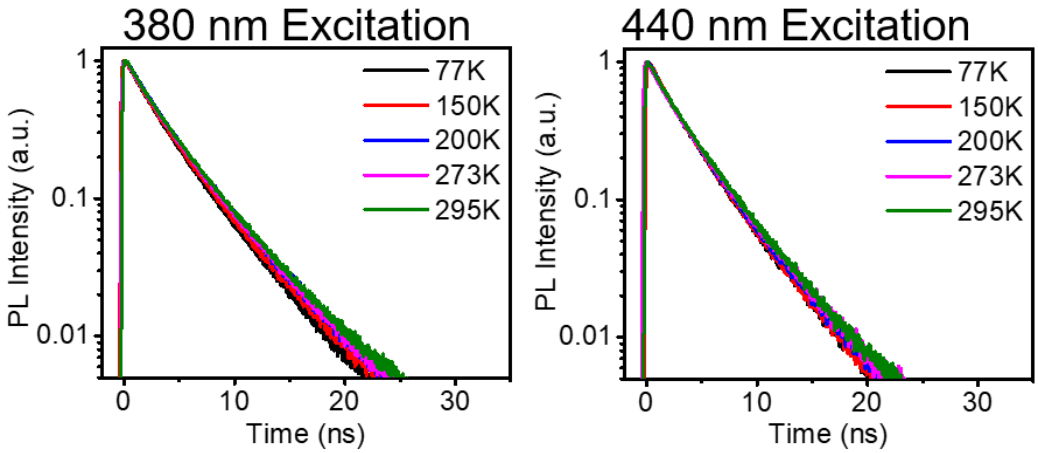

Figure 25. Luminescence decay profiles for H_4tcbpe at various temperatures under 380 (left) and 440 nm (right) excitation.

Table 5. Excited state lifetime data for H_4tcbpe under 440 nm excitation at various temperatures.

	380 nm excitation			440 nm excitation		
Temp	**Avg. amp. weighted τ**	**τ1 (ns)**	**τ2 (ns)**	**Avg. amp. weighted τ**	**τ1 (ns)**	**τ2 (ns)**
77 K	3.40	2.38 (57.3%)	4.76 (42.7%)	3.29 ns	2.56 (69.0%)	4.91 (31.0%)
150 K	3.54	2.51 (58.0%)	4.97 (42.0%)	3.21 ns	2.23 (55.9%)	4.47 (44.1%)
200 K	3.65	2.45 (51.8%)	4.95 (48.2%)	3.30 ns	2.25 (54.1%)	4.54 (45.9%)
273 K	3.63	2.31 (48.8%)	4.90 (51.2%)	3.43 ns	2.08 (42.7%)	4.43 (57.3%)
295 K	3.67	2.30 (48.7%)	4.98 (51.3%)	3.44 ns	2.11 (44.2%)	4.49 (55.8%)

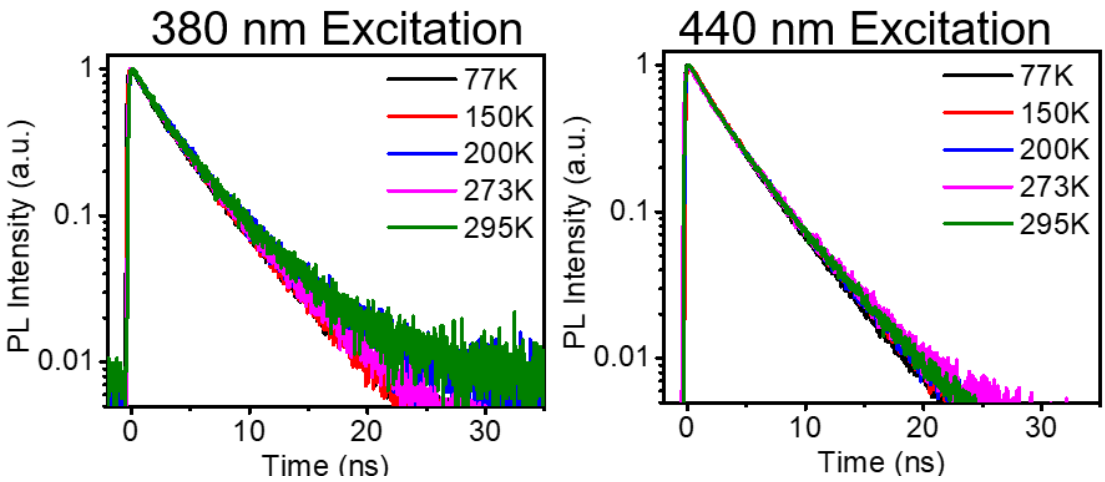

Figure 26. Luminescence decay profiles for H4tcbpe-F at various temperatures under 380 nm (left) and 440 nm (right) excitation.

Table 6. Excited state lifetime data for H4tcbpe-F under 440 nm excitation at various temperatures.

	380 nm excitation			440 nm excitation		
Temp	**Avg. amp. weighted τ**	**τ1 (ns)**	**τ2 (ns)**	**Avg. amp. weighted τ**	**τ1 (ns)**	**τ2 (ns)**
77 K	3.61	2.30 (47.0%)	4.78 (53.0%)	3.52 ns	2.73 (66.5%)	5.08 (33.5%)
150 K	3.63	2.65 (60.3%)	5.12 (39.7%)	3.55 ns	2.38 (49.0%)	4.68 (51.0%)
200 K	3.86	2.97 (69.6%)	5.89 (30.4%)	3.60 ns	2.38 (47.7%)	4.71 (52.3%)
273 K	3.67	2.49 (55.2%)	5.16 (44.8%)	3.58 ns	2.10 (41.7%)	4.63 (58.3%)
295 K	3.80	2.58 (58.0%)	5.48 (42.0%)	3.57 ns	2.34 (50.5%)	4.83 (49.5%)

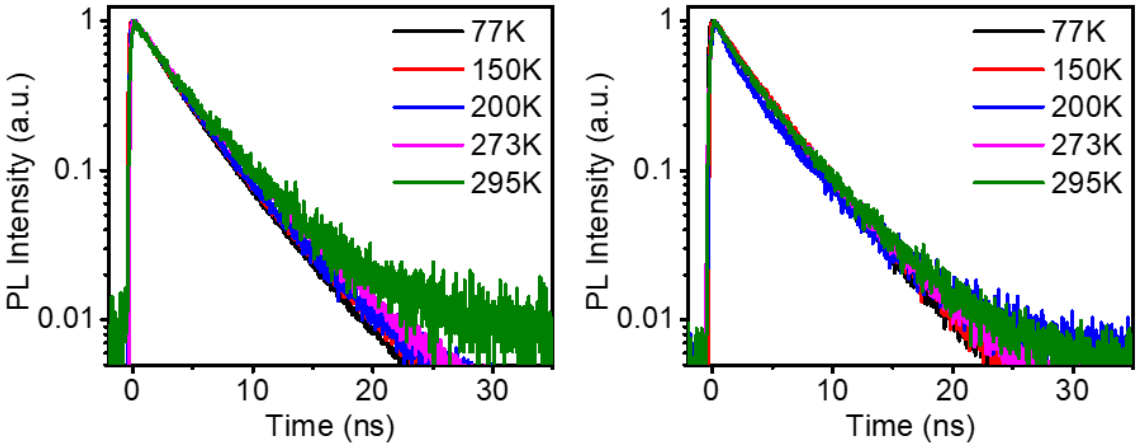

Figure 27. Luminescence decay profiles for LMOF-231 at various temperatures under 380 nm (left) and 440 nm (right) excitation.

Table 7. Excited state lifetime data for LMOF-231 under 380 and 440 nm excitation at various temperatures.

	380 nm excitation			440 nm excitation		
Temp	**Avg. amp. weighted τ**	**τ1 (ns)**	**τ2 (ns)**	**Avg. amp. weighted τ**	**τ1 (ns)**	**τ2 (ns)**
77 K	3.64 ns	3.07 (82.0%)	6.23 (18.0%)	3.85 ns	3.13 (69.1%)	5.47 (30.9%)
150 K	3.73 ns	3.04 (76.7%)	6.00 (23.3%)	3.90 ns	2.82 (47.0%)	4.87 (53.0%)
200 K	3.82 ns	3.36 (89.2%)	7.63 (10.8%)	3.24 ns	1.38 (43.5%)	4.67 (56.5%)
273 K	4.07 ns	3.22(69.2%)	6.00 (30.8%)	3.81 ns	2.10 (36.3%)	4.79 (63.7%)
295 K	4.14 ns	3.02 (56.3%)	5.59 (43.7%)	3.80 ns	1.98 (35.6%)	4.80 (64.4%)

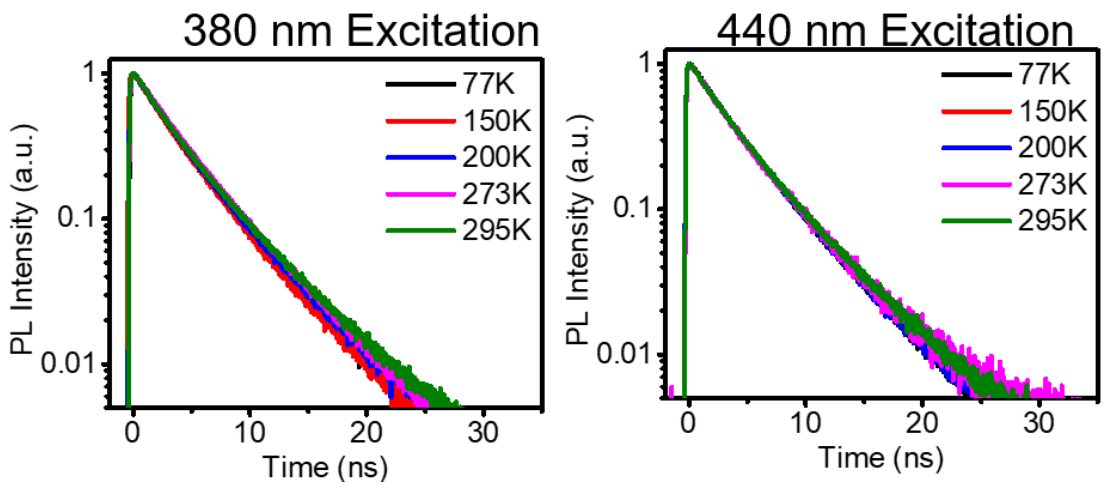

Figure 28. Luminescence decay profiles for LMOF-305 at various temperatures under 380 nm (left) and 440 nm (right) excitation.

Table 8. Excited state lifetime data for LMOF-305 under 380 nm and 440 nm excitation at various temperatures.

	380 nm excitation			440 nm excitation		
Temp	**Avg. amp. weighted τ**	**τ1 (ns)**	**τ2 (ns)**	**Avg. amp. weighted τ**	**τ1 (ns)**	**τ2 (ns)**
77 K	3.92	3.39 (84.2%)	6.74 (15.8%)	3.96 ns	3.44 (85.5%)	7.05 (14.5%)
150 K	3.78	2.92 (65.2%)	5.38 (34.8%)	3.97 ns	2.66 (47.8%)	5.16 (52.2%)
200 K	3.92	3.12 (74.3%)	6.23 (25.7%)	3.97 ns	3.15 (69.9%)	5.86 (30.1%)
273 K	4.09	3.41(78.6%)	6.61 (21.4%)	3.98 ns	3.00 (66.2%)	5.91 (33.8%)
295 K	3.99	2.87 (64.6%)	6.04 (35.4%)	4.05 ns	3.05 (66.2%)	6.00 (33.8%)

At room temperature, both LMOF samples possessed similar average amplitude weighted lifetimes of approximately 4 ns (3.81 ns for LMOF-231 and 3.98 ns for LMOF-305) at 273 K, with the total decay being the sum of two processes (τ1 and τ2). LMOF-305 showed longer lifetimes for τ1 and τ2, with τ1 (3.05 ns) being 54 % longer than that of LMOF-231 (1.98 ns) and τ2 (6.00 ns) being 25 % longer than that of LMOF-231 (4.80 ns). Despite this,

the average amplitude-weighted lifetimes were very similar because the longer τ2 lifetime was dominant in LMOF-231, while the shorter τ1 lifetime was dominant in LMOF-305.

Importantly, the lifetime behavior displayed by LMOF-305 under 440 nm excitation is identical to the previously-discussed lifetime behavior of LMOF-231 under 380 nm excitation. This is strong evidence that inclusion of the fluorinated ligand helped push emission towards the more efficient "higher-energy pathway". It should also be noted that the lifetime of LMOF-305 is independent of excitation wavelength, which further indicates that the luminescence mechanism for the material is identical for both blue and UV photons, unlike LMOF-231.

Furthermore, the same trend can be observed when comparing the lifetime of H_4tcbpe and H_4tcbpe-F; both the τ1 and τ2 processes are slower at room temperature in H_4tcbpe-F, but the relatively faster τ1 process plays a larger role in the fluorinated ligand. This suggests that the H_4tcbpe-F ligand plays a relatively large role in the emission from LMOF-305, despite the fact that it is present at a much lower concentration than H_4tcbpe, and is convincing evidence that excitation energy moves to the H_4tcbpe-F ligand before emission. furthermore, the fact that LMOF-305 has both a higher quantum yield than LMOF-231 and slower excited state decay processes indicates that the inclusion of H_4tcbpe-F within LMOF-231 weakens nonradiative excited state recombination.

4.4 Conclusions

In order to develop LMOF-based phosphor materials capable of competing with the commercial yellow phosphor YAG:Ce for applications in PC-WLEDs, it is necessary to be able to develop a yellow-emitting LMOF with quantum yield comparable to YAG:Ce under blue (455 nm) excitation. We have previously developed LMOF-231, based on the

chromophoric ligand H_4tcbpe. With a quantum yield of 76% (λ_{ex} = 455 nm), it became the highest performing yellow phosphor among all LMOFs reported to date. However, further improvement was necessary to increase the material's competitiveness. To address this, spectroscopic measurements were used to assess the potential excitation mechanisms at work within the LMOF, and DFT calculations were performed to help design a ligand that could be doped into the LMOF-231 structure and function as a bandgap modulator. The ligand H_4tcbpe-F was synthesized, and spectroscopic studies indicated that it possessed the qualities predicted by DFT calculations; namely, reduced HOMO and LUMO energies and a largely unchanged HOMO-LUMO energy gap. H_4tcbpe-F was successfully doped into LMOF-231 at 20% occupancy, and the resulting LMOF-305 showed increased blue light absorption and a significantly higher quantum yield of 88.2% under blue excitation. This material is the strongest blue-excitable yellow-emitting LMOF phosphor yet reported, and serves as an example of how understanding luminescence mechanisms within LMOFs can guide the rational design of materials with higher performance.

Chapter 5: Improving LMOF QY via Guest-Mediated Rigidification

5.1 Introduction

It is extremely important for LMOF applications for it to have strong emission properties, so a significant amount of research has been focused on producing LMOFs with exceptional quantum yields;[66, 81-85] however, it can be challenging to develop an LMOF that possesses both the chemical stability and emission profile required by a given application and a high quantum yield. As shown previously, introducing bandgap modulating ligands can be an effective method for accomplishing this. However, as that strategy requires specific circumstances, it is important to develop more general methods for improving quantum yields.

In LMOFs, quantum yields can often be depressed by framework flexibility.[86-87] Upon excitation, vibrational and rotational modes are often available to return the excited electron to the ground state in a non-radiative fashion. This can be addressed using rigidification strategies first developed for improving quantum yield in flexible organic chromophore molecules; for example, ligand design can be altered to increase rigidity.[88-90] However, solutions like this typically place a design limit on the types of LMOFs which can be used in applications requiring strong photoluminescence. In situations where these strategies cannot work, it is necessary to develop post-synthetic methods for rigidifying the frameworks. One way that this can be accomplished is through "guest-packing", in which loading the porous LMOF with a guest molecule serves to prevent certain vibrational or rotational modes from being available.

This chapter reports the synthesis and structure of [Zn_2(tcbpe)(bpy) or LMOF-263; H_4tcbpe = 1,1,2,2-tetrakis(4-(4-carboxy-phenyl)phenyl)ethene, bpy = 4,4'-bipyridine] and its framework rigidification by a post-synthesis guest-packing approach. For comparison

purpose, a previously-discussed isoreticular LMOF, [Zn2(tcbpe-F)(bpy) or LMOF-301; H_4tcbpe-F = 1,1,2,2-tetrakis(4-(4-carboxy-3-fluoro-phenyl)phenyl)ethene] is also included in the study.[67] The two LMOFs possess nearly identical ligands, with the only difference being the replacement of one of the hydrogen vicinal to the carboxylate group with fluorine; both structures have formulas of Zn_2(tcbpe-R)(bpy), with R = H in LMOF-263 and F in LMOF-301. This difference permits rotation of a pyridyl moiety in a neighbouring bpy ligand in LMOF-236, while the rotation is sterically prevented in LMOF-301. These two LMOFs serve as an ideal model system for testing a guest-packing rigidification effect. Guest molecules with various functional groups and of various shapes and sizes are loaded into these two LMOFs, and it is determined that quantum yield is significantly improved in the rotation-allowed LMOF-236 upon loading with n-pentane, as the solvent rigidifies the framework by inducing a framework shift that brings the rotating bpy moiety into contact with the neighbouring framework.

5.2 Materials and Methods

The ligands H_4tcbpe and H_4tcbpe-F were synthesized according to previously published reports.[66-67] All solvents, reagents, and catalysts used in the synthesis of these two ligands were purchased from Sigma Aldrich and used without further purification. The ligand bpy, $Zn(NO_3)_2 \cdot 6H_2O$, $Zn(ClO_4)_2 \cdot 6H_2O$ dimethylacetamide (DMA), and HBF_4 used in the synthesis of the LMOFs 236 and 301, as well as all solvents used in the solvent exchange/guest packing experiment, were also purchased from Sigma Aldrich and used without further purification.

To synthesize LMOF-236, 0.050 mmol $Zn_2(NO_3)_2 \cdot 6H_2O$ was added to 0.025 mmol H_4tcbpe and 0.050 mmol bpy in a glass vial. 4 mL DMA was added, followed by 2 drops of HBF_4, and the solution was sonicated until clear. The vial was sealed and placed in a 100 °C

oven for 72 hours, after which the crystals were recovered via filtration. LMOF-301 was synthesized using the reported method.[67]

Solvent exchange was achieved by immersing the LMOF samples in 20 mL of the exchange solvent, and replacing the solvent five times over the course of 10 hours. Solvent was exchanged with a pipet, and without filtering. The samples were then left immersed in the exchange solvent for at least another 24 hours, and stored in the exchange solvent until analysis. Outgassed samples of LMOF-236 and LMOF-301 were prepared by placing the pentane-exchanged samples in a vacuum oven at 40 °C overnight.

Single crystal diffraction data for LMOF-236 were collected at 100 K on a Bruker APEXII CCD diffractometer using the synchrotron source (λ = 0.7749 Å) at the Advanced Light Source 11.3.1 Chemical Crystallography beamline, Berkeley National Lab. All non-hydrogen atoms were refined anisotropically. Hydrogen atoms were placed geometrically, constrained, and refined with a riding model. The unresolvable electron density from the framework's void space was removed by SQUEEZE (Table 9).

All powder X-ray diffraction (PXRD) data was collected on a Rigaku Ultima IV diffractometer with a wavelength of 1.5406 Å, scanning from 3° to 35° 2θ at a rate of 2° 2θ/min and with and a step size of 0.2° 2θ. All thermogravimetric analysis data was collected using a TA Instruments Q5000 TGA. Samples were loaded into a Pt pan and heated under a constant dry N2 flow of 20 mL/min. The temperature was gradually increased from ambient to 600 °C at a constant rate of 10 °C/min.

All photoluminescence emission and excitation spectra were collected in the solid state using a Varian Cary Eclipse spectrophotometer at room temperature. Internal quantum yield was measured in the solid state at room temperature for all samples, using a Hamamatsu

Quantarus-QY spectrophotometer with a 150 W Xenon monochromatic light source and integrating sphere.

Density functional theory (DFT) calculations were performed using Gaussian 09, with the B3LYP3 hybrid functional and 6-311++(3df,3pd) basis set.[74-75, 77-78, 91] The geometries of bpy, H_4tcbpe, and H_4tcbpe-F were optimized, and a frequency calculation was performed after the geometry optimization to confirm that all calculations resulted in a true minimum.

Table 9. Single crystal data of LMOF-236

Compound	LMOF-263
Formula	$C_{64}H_{40}N_2O_8Zn_2$
M	1002.07
Crystal system	Triclinic
Space group	P -1
a/Å	13.9511(6)
b/Å	16.5329(7)
c/Å	20.1599(9)
α/o	89.937(3)
β/o	82.221(2)
γ/o	88.827(2)
V, Å^3	4606.16(35)
Z	2
Temperature (K)	100
λ(radiation wavelength) Å	0.7749
D, g/cm^3	0.722459
Reflections collected	39877
R1[a] [I > 2σ(*I*)]	0.0607
wR2[b] [I > 2σ(*I*)]	0.1779
Goodness-of-fit	0.983
CCDC No.	1947629

[a] $R1 = \sum | F_o - F_c | / \sum | F_o |$

[b] $wR2 = \sum[w(F_o^2 - F_c^2)^2] / w(F_o^2)^2]^{1/2}$

5.3 Results and Discussion

5.3.1 LMOF-236 and LMOF-301 Structure

LMOF-236 is triclinic and crystallizes in the space group P-1. It is composed of 2D layers of the tcbpe ligand, with each ligand linked to four more through classic zinc-paddlewheel SBUs to form a sheet in the *bc* plane. The pillaring bpy ligand links these sheets into a three dimensional framework by bonding to the axial SBU position in neighbouring layers. Two of these frameworks interpenetrate to give the complete structure (fig. 29). LMOF-301 is nearly identical to LMOF-236, with the primary difference being the presence of a fluorine atom on the ligand carbon vicinal to the carboxylate group instead of a hydrogen atom.

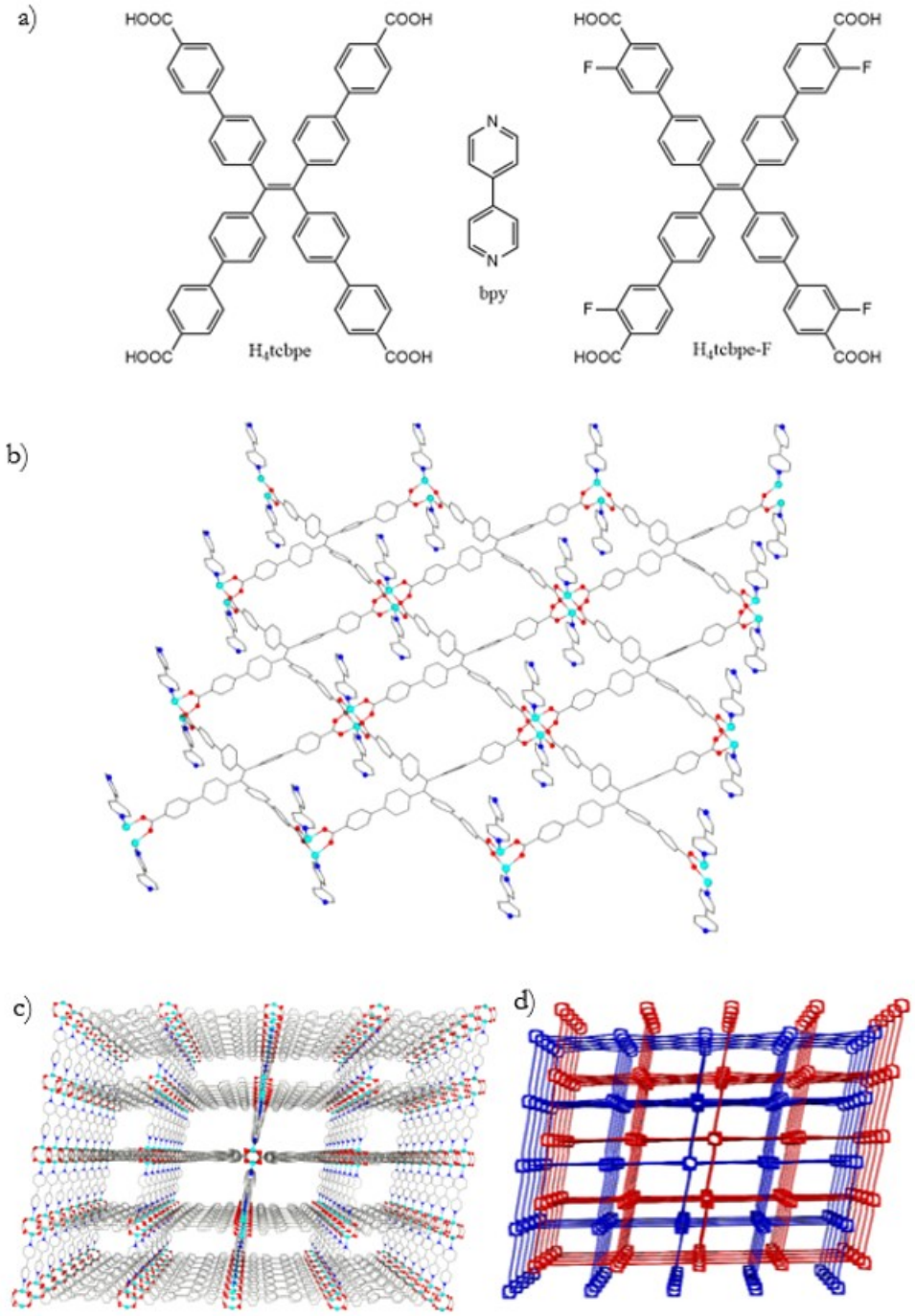

Figure 29. (a) Structures of the ligands H_4tcbpe, bpy, and H_4tcbpe-F (b) 2D sheet of tcbpe ligands in the bc plane linked by zinc paddlewheel SBUs, showing pillaring bpy ligands extending above and below the sheet. (c) Single 3D net of LMOF-236. (d) Schematic of two interpenetrated nets (red and blue), giving the final structure of LMOF-236.

In the structure of LMOF-236, one of the two pyridyl rings in the ligand bpy has a large degree of rotational freedom (fig. 30). At its closest, the H-H distance between this

pyridine group's hydrogen and the closest atom on the neighbouring framework—a hydrogen located on the tcbpe ligand—is 3.8 Å measuring from nucleus to nucleus, which is sufficient to permit free rotation of the pyridine moiety. In fact, the only significant steric interaction is the H-H interaction between pyridyl rings within the same bpy ligand. However, given the exceptionally low thermal barrier to rotation in non-substituted biphenyls at room temperature,[92] it is reasonable to consider this interaction trivial.

The same is not true for LMOF-301, in which the presence of fluorine on the tcbpe-F ligand plays a major role in preventing free rotation of the bpy pyridyl ring (fig. 30). In LMOF-301, the distance between the pyridyl hydrogen and fluorine on the neighbouring framework is just 2.54 Å, suggesting the formation of a weak H-F interaction,[93] and preventing rotation of the pyridyl ring, as continued rotating would further decrease the H-F distance. This is consistent with the single crystal data for LMOFs 236 and 301, as the pyridyl ring in the structure of LMOF-301 shows no disorder, while the same pyridyl ring in LMOF-236 shows significant rotational disorder, even when cooled to 100 K.

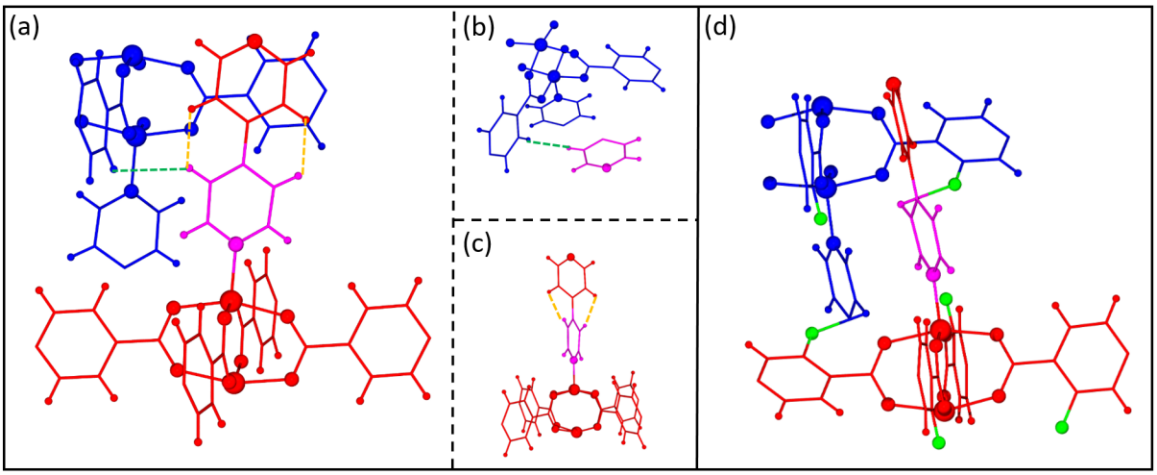

Figure 30. (a) Fragment of LMOF-236 showing the interaction between the two frameworks (red and blue) around a highlighted pyridyl moiety (pink) with significant rotational freedom. The dotted green line shows the closest interaction between the highlighted pyridine and the neighbouring framework (3.8 Å), while the dotted orange lines indicate the closest intramolecular interaction of the bpy via the

two H atoms located at the two pyridyl rings (red and pink) of the same framework. (b) Isolated view of the H—H interaction between the highlighted pyridine (pink) and the neighbouring framework. (c) Isolated view of the intramolecular H—H interaction between the two pyridyl groups of bpy (pink and red) within the same framework. (d) Fragment of LMOF-301 showing the interaction between the two frameworks (red and blue) around a highlighted pyridyl moiety (pink), with the H-F interaction (2.54 Å) shown as a bond between the fluorine atom (green) and the pyridyl hydrogen on the neighbouring framework. All distances given are measured between atom centers.

5.3.2 Guest-mediated rigidification

The luminescence properties of the chromophoric ligands in LMOF-236 (tcbpe) and LMOF-301 (tcbpe-F) are very similar,[38] as both ligands have nearly identical HOMO-LUMO energy gaps. And although a second ligand (bpy) is present within the structure, it is expected to have minimal effect on the excitation and emission transitions, as DFT calculations indicated that bpy's LUMO is located significantly higher than that of H_4tcbpe and H_4tcbpe-F, while its HOMO is lower than those of the chromophore ligands (table 10).

Table 10. Calculated LUMO and HOMO energy levels for the ligands bpy, H4tcbpe, and H4tcbpe-F.

Ligand	LUMO	HOMO
bpy	-2.02 eV	-7.39 eV
H_4tcbpe	-2.46 eV	-5.87 eV
H_4tcbpe-F	-2.68 eV	-6.10 eV

Both LMOF-263 and LMOF-301 emit at approximately 520 nm when excited by 455 nm light (fig. 31). For LMOF-301, the quantum yield is fairly consistent regardless of the solvation state of the LMOF, dropping from 50.9% in the as-made state (DMA-solvated) to 45.1% upon solvent removal under 455 nm excitation (table 11). This performance is consistent with ligand-centered emission from the free chromophoric ligand H4tcbpe-F, which has a quantum yield of 46.5% under the same excitation conditions (table 12).[25] For LMOF-263, the quantum yield shows a much stronger dependence on the presence of guest molecules within the pore, with the as-made (DMA-solvated) sample's quantum yield under

455 nm excitation of 42.5% dropping to just 12.2% upon removal of the solvent (table 8). Both of these values are significantly lower than the free H_4tcbpe ligand's quantum yield of 62.3% under the same excitation conditions (table 12).[66]

In both cases, the trends in luminescent efficiency are consistent with our understanding of the LMOFs' structures. In the case of LMOF-301, strong interaction between the fluorine located on the chromophore ligand and the hydrogen located on the bpy ligand serves to rigidify the structure in the absence of pore solvent, which helps to maintain the activated structure's quantum yield. In the case of LMOF-236, the ability of the bpy pyridyl ring to freely rotate in the absence of pore solvent induces a significant drop in the activated structure's quantum yield.

In order to assess how effectively the rotation of the bpy pyridyl moiety could be suppressed, solvent exchange was performed on both LMOF-236 and LMOF-301 with a variety of solvents. Solvents were selected to represent a diverse group of functionalities, molecule size, and molecule shape. Following activation and solvent exchange, quantum yield measurements were taken, PXRD was used to confirm that the samples remained crystalline (fig. 32), and TGA decomposition curves were collected for selected samples to assess the degree of solvent exchange (fig. 33). The results are summarized in Table 11.

Table 11. Quantum yields of samples of LMOF-236 and LMOF-301 following solvent exchange under 455 nm excitation

Solvent	QY (LMOF-236)	QY (LMOF-301)
Dimethylacetamide	42.5 % (as made)	50.9 % (as made)
Outgassed	12.2 %	45.1 %
Acetone	Not stable	Not tested
Ethanol	Not stable	Not tested
Isopropanol	Not stable	Not tested
Glycerol	Not stable	Not tested
Triethylamine	Not stable	Not tested
Dichloromethane	Not stable	Not tested

Ethyl Acetate	27.3 %	49.3 %
N-Pentane	59.3 %	48.5 %
Cyclohexane	44.2 %	44.9 %
Dodecane	43.7 %	41.6 %
Benzene	32.5 %	28.2 %
Toluene	21.7 %	16.7 %
Durene	35.1 %	33.8 %

Table 12. Ligand quantum yield data

Ligand	Internal quantum yield
H4tcbpe	62.3%
H4tcbpe-F	46.5 %

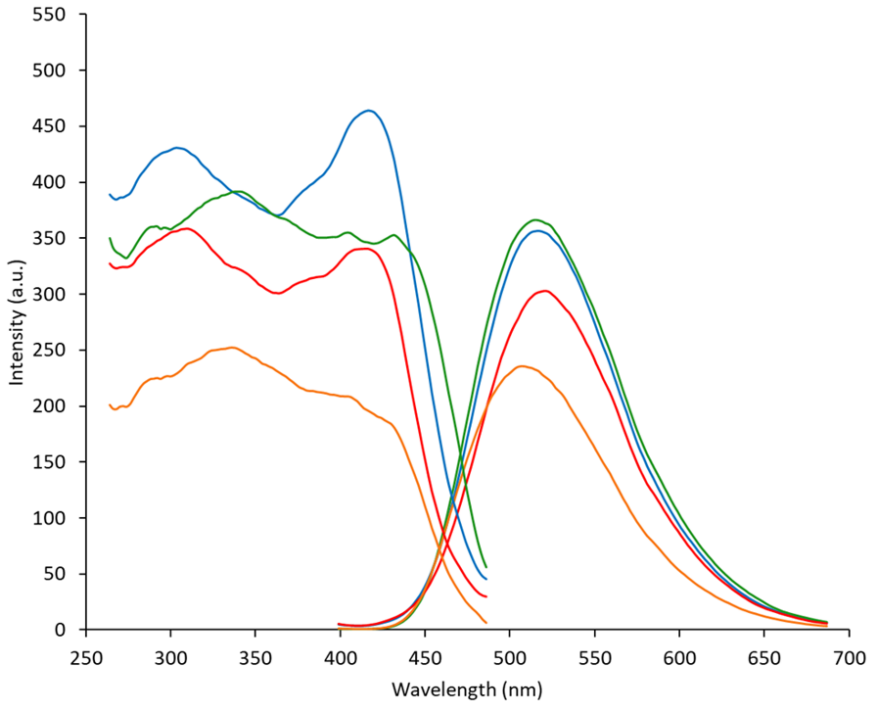

Figure 31. Excitation (left) and emission (right) spectra of DMA-solvated LMOF-236 (blue), DMA-solvated LMOF-301 (red), pentane-solvated LMOF-236 (green), and pentane-solvated LMOF-301

(gold). Excitation spectra were monitored at 520 nm emission, and emission spectra were collected under 455 nm excitation

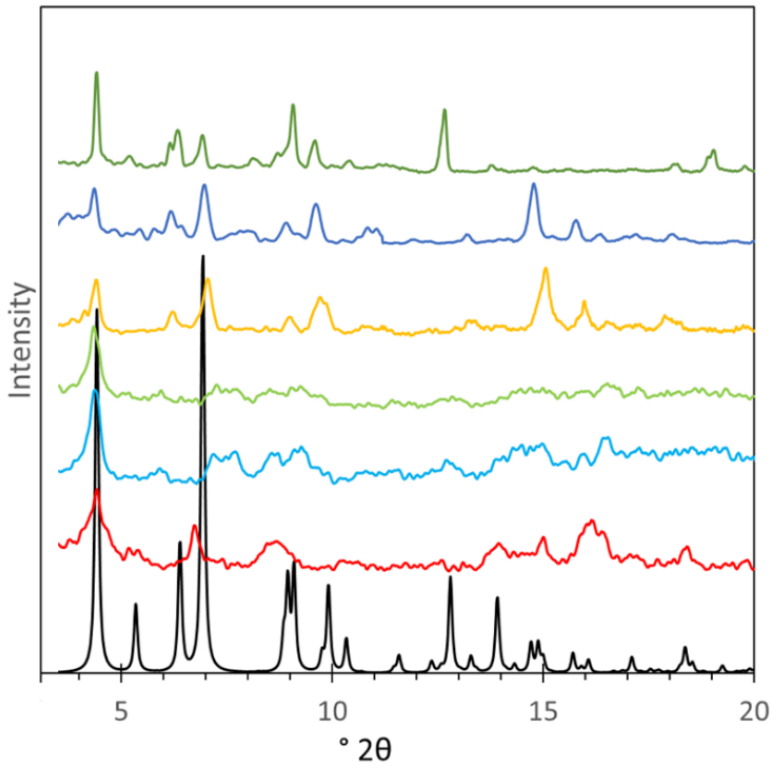

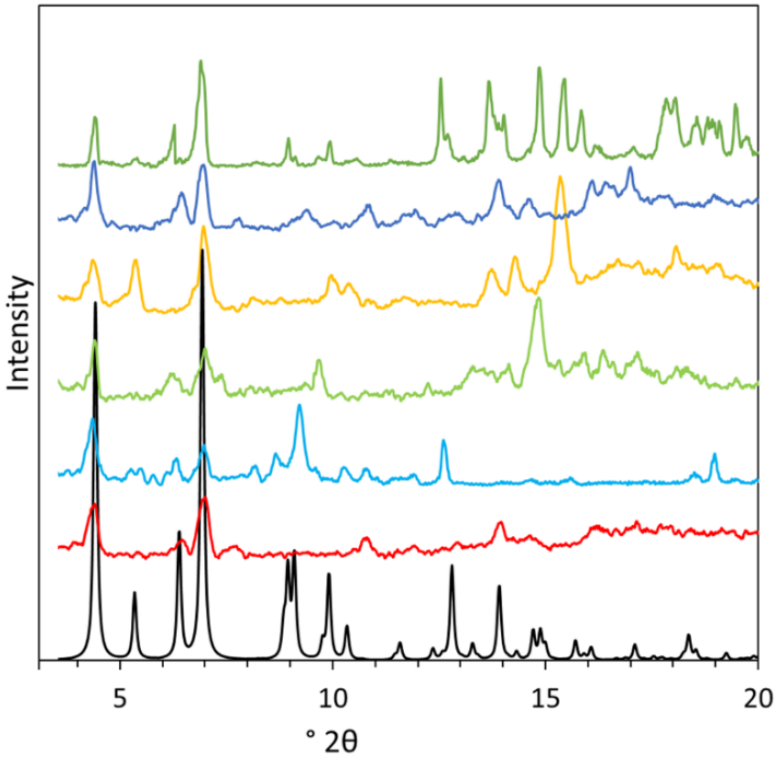

Figure 32. (Top) Powder X-ray diffraction patterns for as-made LMOF-263 (dark green), benzene-loaded LMOF-263 (dark blue), toluene-loaded LMOF-263 (gold), cyclohexane-loaded LMOF-263 (light green), n-dodecane-loaded LMOF-263 (light blue), and ethyl acetate-loaded LMOF-263 (red). The simulated pattern for LMOF-263 is shown in black. (Bottom) Powder X-ray diffraction patterns for as-made LMOF-301 (dark green), benzene-loaded LMOF-301 (dark blue), toluene-loaded LMOF-301 (gold), cyclohexane-loaded LMOF-301 (light green), n-dodecane-loaded LMOF-301 (light blue), and ethyl acetate-loaded LMOF-301 (red). The simulated pattern for LMOF-301 is shown in black.

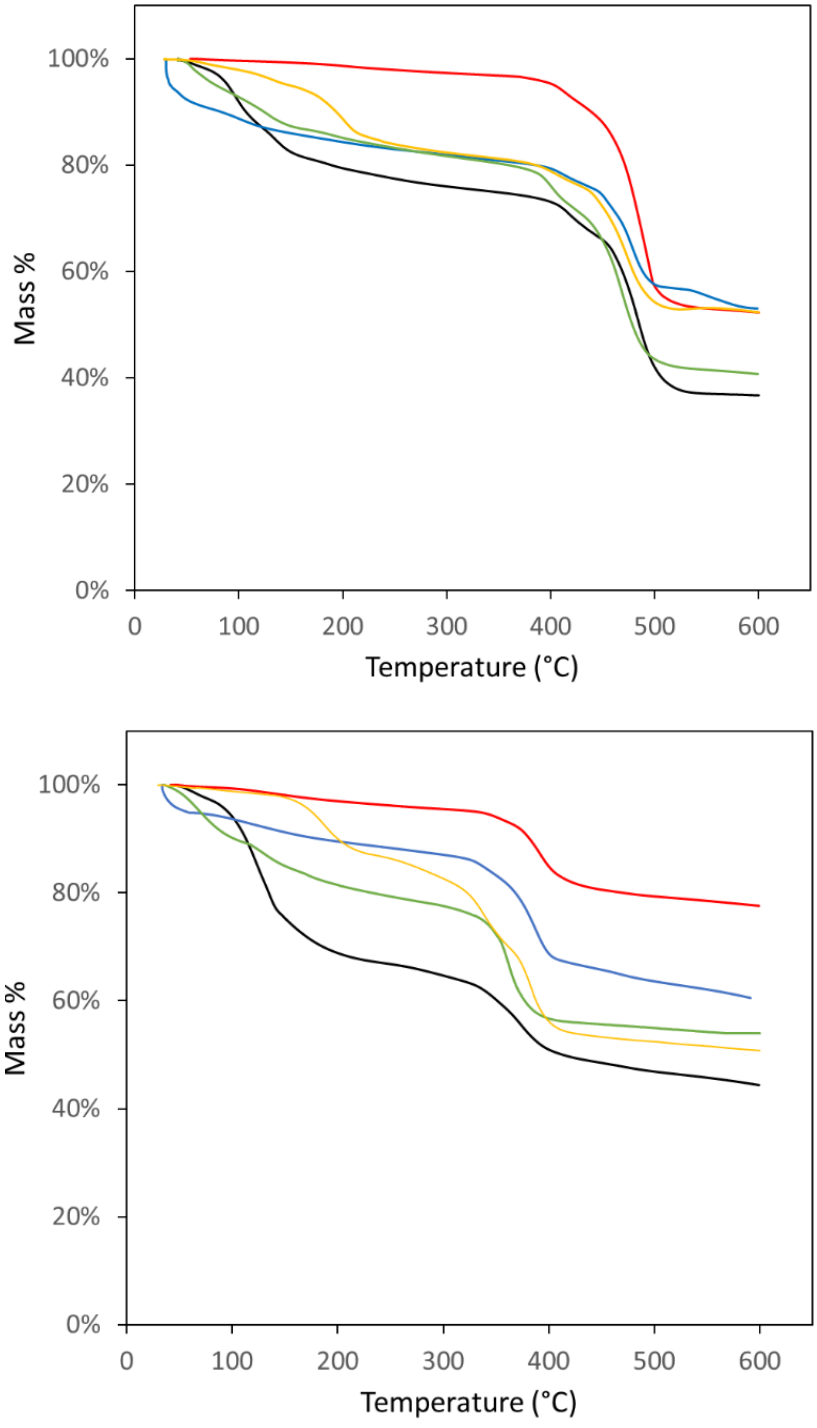

Figure 33. (Top) Thermogravimetric analysis data for LMOF-236 as made (black), outgassed (red), pentane-loaded (blue), cyclohexane-loaded (green), n-dodecane-loaded (yellow). (Bottom) Thermogravimetric analysis data for LMOF-301 as made (black), outgassed (red), pentane-loaded (blue), cyclohexane-loaded (green), n-dodecane-loaded (yellow).

For LMOF-301, aliphatic solvents had little impact on the quantum yield, indicating that any electronic interactions between the solvent and the LMOF were limited, and that any changes in the general rigidity of the framework itself had no appreciable effect on the quantum yield. Aromatic solvents significantly decreased quantum yield, which may be due to an electronic interaction between the solvent molecules and the LMOF framework.[67] For LMOF-263, quantum yield was significantly decreased upon activation where DMA solvent molecules were removed from the LMOF pores. Upon solvent exchange, quantum yield was significantly increased for both aliphatic and aromatic species, indicating that the presence/inclusion of any solvent molecule was sufficient to restrict the rotation of the bpy pyridyl moiety at different extent. The quantum yields in the presence of aromatic solvents was in trend with those of LMOF-301, and it is possible that these solvents effectively deactivated the pyridyl rotation, but that the same electronic interaction observed in LMOF-301 limited emission. The only solvent to significantly improve on the as-made quantum yield in LMOF-236 was n-pentane, which lifted the quantum yield to 59.3%.

Comparing the PXRD patterns of the pentane-loaded LMOF-263 and LMOF-301 with the activated and simulated patterns, it is apparent that framework flexibility allows both LMOFs to expand upon solvation with n-pentane (Fig. 34). In both pentane-loaded LMOFs, the 001 peak shifts to a lower angle, corresponding to an expansion along the *c* axis (20.01 Å) of 0.95 Å in LMOF-263 and 1.01 Å in LMOF-301, respectively. Simultaneously, the 010 peak shifts to a higher angle, corresponding to a contraction along the *b* axis (16.55 Å) of 0.83 Å for LMOF-263 and 0.87 Å for LMOF-301. This combination of expansion in the *c* direction and contraction in the *b* direction is consistent with a shifting in the relative positon of the two

interpenetrated frameworks, which has been previously observed in interpenetrated MOFs.[94-95] With the frameworks sliding in the negative *b*/positive *c* direction, it would bring LMOF-263's free-rotating pyridyl moiety from one framework nearly into contact with the tcbpe ligand in the other framework, as the nucleus-nucleus H—H distance would shrink to just 2.0 Å, effectively rigidifying the ligands.

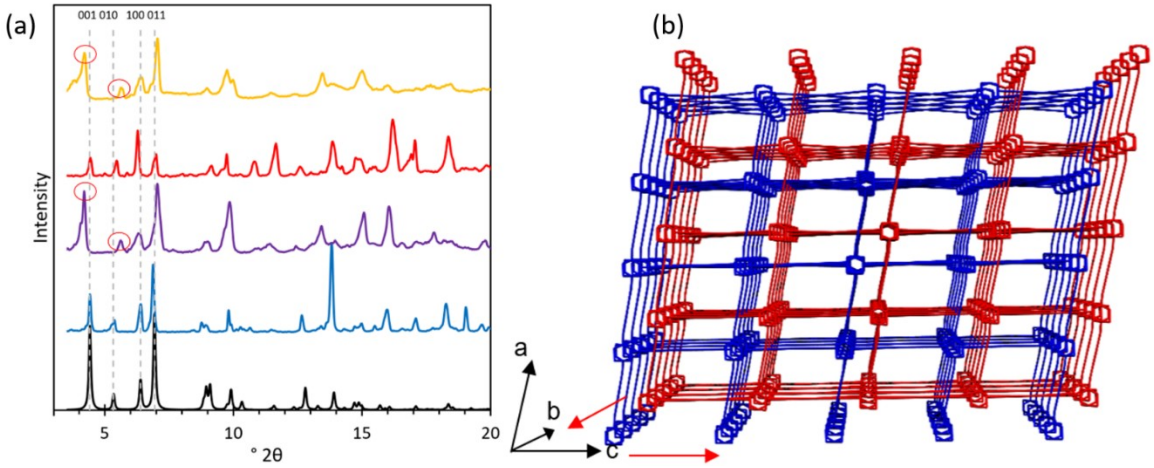

Figure 34. (a) Simulated PXRD pattern of LMOF-263 (black), overlaid with the PXRDs of the activated LMOF-263 (blue), activated LMOF-301 (red), the pentane-loaded LMOF-263 (purple), and pentane-loaded LMOF-301LMOF-301 (gold). The first four peaks are indexed, and the peak changes observed in the pentane-loaded samples are marked with red circles. As LMOF-263 and LMOF-301 are isoreticular with nearly identical unit cells, only the simulated pattern for LMOF-263 is shown. (b) A crystallographic shift that could be responsible for the expansion along the c axis and contraction along the b axis observed in the pentane-loaded samples.

5.4 Conclusions

Developing strategies for the post-synthetic rigidification of LMOFs provides another useful tool to fine-tune and enhance their luminescence. In this chapter, two isoreticular LMOFs having very similar structure but different framework rigidity are selected as ideal test materials to examine the solvent-packing effect to rigidification. LMOF-236 emission is severely weakened because of a freely-rotating pyridyl ring on the bpy ligand, while LMOF-301 shows very limited flexibility-related emission quenching due to limited rotation of the same pyridyl ring as a result of strong inter-framework hydrogen-fluorine interaction. The

structural similarities were discussed, and the structural basis for their divergent behavior was elucidated. Solvents with various functional groups and of various shapes and sizes were loaded into the two LMOFs, and n-pentane was able to enhance the emission from LMOF-236 by 40% with respect to the as-made sample and 386% with respect to the activated sample. Changes in the unit cells of their crystal structures demonstrate that n-pentane shifts the interpenetrated nets in both LMOF-263 and LMOF-301. In LMOF-263, this pushes the freely-rotating pyridyl ring from one net closer to the second net, restricting rotation and restoring emission intensity from the material, while in LMOF-301, the rotation of the pyridyl ring was already restricted, so the same shift does not result in noticeable changes in luminescent efficiency.

Chapter 6: Conclusions

Metal-organic frameworks are crystalline, typically porous materials composed of rigid, multitopic organic ligands linking together metal ions or metal ion clusters. The properties of metal-organic frameworks are extremely diverse, and arise from the interactions between various MOF building blocks. Luminescent MOFs are especially interesting for applications in sensing and as phosphor materials, as they combine a large surface area, strong signal, and highly tunable chemistry with a crystalline nature that enables precise, atomistic understanding of the material.

When designing an LMOF for sensing applications, strong luminescence is ideal to provide an easily detectable signal that can be modulated by the presence of the analyte. Ensuring a strong interaction between the sensor LMOF and the analyte is also important; specific functional groups within an LMOF can improve the specificity of LMOF-analyte interactions, but significant porosity and a high surface area are equally important. Finally, it is necessary to ensure that the electronic properties of the LMOF will allow its luminescent properties to change in a detectable fashion when exposed to the analyte in question. By combining porosity with the appropriate LUMO energy levels, the first LMOF optical sensor for mycotoxins was developed, with a LOD significantly lower than FDA requirements.

Designing a phosphor material can be more challenging, as there are fewer specific design requirements, and LMOFs can have complex emission mechanisms. As such, using a chromophore-based approach is one of the more reliable options. Using this strategy, an organic chromophore—ideally with aggregation-induced-emission qualities—is selected and converted into a ligand molecule, which is in turn immobilized into an LMOF using either a d^0 or d^{10} metal. Using a metal with either a completely filled or completely empty d orbital often prevents the metal from participating in luminescence, so the emissive properties of the

LMOF will be based on those of the chromophoric ligand. These can be more easily designed, especially using DFT calculations as a fast screening method to identify promising structures. Incorporation of the chromophore into the MOF will likely improve both thermal stability and quantum yield through rigidification.

Additionally, if the photoluminescence behavior of the chromophoric ligand requires fine tuning, it is possible to include additional ligands within the LMOF to influence the material's behavior. In the event of strong ligand-ligand charge transfer behavior, it is possible to alter the material's band gap by doping in a functionalized version of the ligand with offset HOMO-LUMO energy levels. Polarized photoluminescence spectroscopy can assist in identifying when this would be the case, as well as identify if the LLCT behavior is stronger after the bandgap modulating ligand is installed. This strategy was used to rationally develop a blue-excitable yellow-emitting LMOF with the highest quantum yield yet reported.

The structural diversity of metal-organic frameworks enables many approaches to similar issues. In cases where the quantum yield must be improved but changes cannot be made to the framework character, post-synthetic rigidification methods can often be successful. This can be accomplished because of MOF porosity. To demonstrate this, a pair of extremely similar isoreticular LMOFs were identified, in which only one exhibited strong non-radiative excitation decay as a result of framework flexibility. Solvent-packing was successfully used to fill the pore and stop the rotation that led to nonradiative decay, while having no significant effect on the control LMOF luminescence.

The strategies reported here represent examples of how improving our understanding of LMOF luminescence mechanisms can enable rational LMOF design and significant advances in LMOF performance. My research has focused on developing this understanding

and rationally design optical sensors and phosphor materials in phosphor-converted white LED bulbs.

REFERENCES

1. Bao, Z.; Chang, G.; Xing, H.; Krishna, R.; Ren, Q.; Chen, B., Potential of microporous metal-organic frameworks for separation of hydrocarbon mixtures. *Energy & Environmental Science* **2016**.
2. He, Y.; Zhou, W.; Krishna, R.; Chen, B., Microporous metal-organic frameworks for storage and separation of small hydrocarbons. *Chemical Communications* **2012,** *48* (97), 11813-11831.
3. Wang, H.; Lustig, W. P.; Li, J., Sensing and capture of toxic and hazardous gases and vapors by metal–organic frameworks. *Chemical Society Reviews* **2018,** *47* (13), 4729-4756.
4. Morozan, A.; Jaouen, F., Metal organic frameworks for electrochemical applications. *Energy & Environmental Science* **2012,** *5* (11), 9269-9290.
5. Song, B.-Q.; Wang, X.-L.; Yang, G.-S.; Wang, H.-N.; Liang, J.; Shao, K.-Z.; Su, Z.-M., A polyrotaxane-like metal–organic framework exhibiting luminescent sensing of Eu3+cations and proton conductivity. *CrystEngComm* **2014,** *16* (30), 6882.
6. Liu, J.; Chen, L.; Cui, H.; Zhang, J.; Zhang, L.; Su, C.-Y., Applications of metal-organic frameworks in heterogeneous supramolecular catalysis. *Chemical Society Reviews* **2014,** *43* (16), 6011-6061.
7. Ke, F.; Yuan, Y.-P.; Qiu, L.-G.; Shen, Y.-H.; Xie, A.-J.; Zhu, J.-F.; Tian, X.-Y.; Zhang, L.-D., Facile fabrication of magnetic metal-organic framework nanocomposites for potential targeted drug delivery. *Journal of Materials Chemistry* **2011,** *21* (11), 3843-3848.
8. Ray Chowdhuri, A.; Bhattacharya, D.; Sahu, S. K., Magnetic nanoscale metal organic frameworks for potential targeted anticancer drug delivery, imaging and as an MRI contrast agent. *Dalton Transactions* **2016,** *45* (7), 2963-2973.
9. Yang, Y.; Zhao, Q.; Feng, W.; Li, F., Luminescent Chemodosimeters for Bioimaging. *Chemical Reviews* **2013,** *113* (1), 192-270.
10. Taylor-Pashow, K. M. L.; Della Rocca, J.; Huxford, R. C.; Lin, W., Hybrid nanomaterials for biomedical applications. *Chemical Communications* **2010,** *46* (32), 5832-5849.
11. Wei, Z.; Gu, Z.-Y.; Arvapally, R. K.; Chen, Y.-P.; McDougald, R. N.; Ivy, J. F.; Yakovenko, A. A.; Feng, D.; Omary, M. A.; Zhou, H.-C., Rigidifying Fluorescent Linkers by Metal-Organic Framework Formation for Fluorescence Blue Shift and Quantum Yield Enhancement. *J. Am. Chem. Soc.* **2014,** *136* (23), 8269-8276.
12. Lustig, W. P.; Mukherjee, S.; Rudd, N. D.; Desai, A. V.; Li, J.; Ghosh, S. K., Metal-organic frameworks: functional luminescent and photonic materials for sensing applications. *Chem. Soc. Rev.* **2017,** *46* (11), 3242-3285.
13. Allendorf, M. D.; Bauer, C. A.; Bhakta, R. K.; Houk, R. J. T., Luminescent metal-organic frameworks. *Chem. Soc. Rev.* **2009,** *38* (5), 1330-1352.
14. Cui, Y.; Yue, Y.; Qian, G.; Chen, B., Luminescent Functional Metal-Organic Frameworks. *Chem. Rev. (Washington, DC, U. S.)* **2012,** *112* (2), 1126-1162.

15. Heine, J.; Muller-Buschbaum, K., Engineering metal-based luminescence in coordination polymers and metal-organic frameworks. *Chemical Society Reviews* **2013,** *42* (24), 9232-9242.

16. Stavila, V.; Talin, A. A.; Allendorf, M. D., MOF-based electronic and opto-electronic devices. *Chemical Society Reviews* **2014,** *43* (16), 5994-6010.

17. Roncali, J., Molecular engineering of the band gap of π-conjugated systems: facing technological applications. *Macromol. Rapid Commun.* **2007,** *28* (17), 1761-1775.

18. Gui, B.; Yu, N.; Meng, Y.; Hu, F.; Wang, C., Immobilization of AIEgens into metal-organic frameworks: Ligand design, emission behavior, and applications. *J. Polym. Sci., Part A: Polym. Chem.* **2017,** *55* (11), 1809-1817.

19. Meyer, L. V.; Schoenfeld, F.; Mueller-Buschbaum, K., Lanthanide based tuning of luminescence in MOFs and dense frameworks - from mono- and multimetal systems to sensors and films. *Chem. Commun. (Cambridge, U. K.)* **2014,** *50* (60), 8093-8108.

20. Xie, W.; Qin, J.-S.; He, W.-W.; Shao, K.-Z.; Su, Z.-M.; Du, D.-Y.; Li, S.-L.; Lan, Y.-Q., Encapsulation of an iridium complex in a metal-organic framework to give a composite with efficient white light emission. *Inorg. Chem. Front.* **2017,** *4* (3), 547-552.

21. Ying, W.; Mao, Y.; Wang, X.; Guo, Y.; He, H.; Ye, Z.; Lee, S.-T.; Peng, X., Solid Confinement of Quantum Dots in ZIF-8 for Efficient and Stable Color-Conversion White LEDs. *ChemSusChem* **2017,** *10* (7), 1346-1350.

22. Zhao, B.; Li, N.; Wang, X.; Chang, Z.; Bu, X.-H., Host-Guest Engineering of Coordination Polymers for Highly Tunable Luminophores Based on Charge Transfer Emissions. *ACS Appl. Mater. Interfaces* **2017,** *9* (3), 2662-2668.

23. An, J.; Shade, C. M.; Chengelis-Czegan, D. A.; Petoud, S.; Rosi, N. L., Zinc-Adeninate Metal-Organic Framework for Aqueous Encapsulation and Sensitization of Near-infrared and Visible Emitting Lanthanide Cations. *J. Am. Chem. Soc.* **2011,** *133* (5), 1220-1223.

24. Chen, C.-X.; Liu, Q.-K.; Ma, J.-P.; Dong, Y.-B., Encapsulation of Ln3+ hydrate species for tunable luminescent materials based on a porous Cd(ii)-MOF. *J. Mater. Chem.* **2012,** *22* (18), 9027-9033.

25. Lustig, W. P.; Wang, F.; Teat, S. J.; Hu, Z.; Gong, Q.; Li, J., Chromophore-Based Luminescent Metal-Organic Frameworks as Lighting Phosphors. *Inorg. Chem.* **2016,** *55* (15), 7250-7256.

26. Farrusseng, D., *Metal-Organic Frameworks: Applications from Catalysis to Gas Storage*. Wiley-VCH: 2011; p 414.

27. Kaskel, S., *The Chemistry of Metal-Organic Frameworks: Synthesis, Characterization, and Applications*. Wiley-VCH: 2016; Vol. 1, p 904.

28. Gao, X.; Chang, S.; Liu, H.; Liu, Z., A Promising White-Light-Emitting Material Constructed from Encapsulating Eu3+/Tb3+ Hybrid Ions into a Robust Microporous Metal-Organic Framework. *Eur. J. Inorg. Chem.* **2016,** *2016* (17), 2837-2842.

29. Srivastava, S.; Gupta, B. K.; Gupta, R., Lanthanide-Based Coordination Polymers for the Size-Selective Detection of Nitroaromatics. *Cryst. Growth Des.* **2017,** *17* (7), 3907-3916.

30. Han, L.; Zhou, J.; Li, X.; Sun, C.-Y.; Zhao, L.; Zhang, Y.-T.; Zhu, M.; Wang, X.-L.; Su, Z.-M., Recognition of harmful fused aromatic hydrocarbons via a metal-organic framework with hydrophobic pores. *Inorg. Chem. Commun.* **2017,** *86*, 200-203.

31. Xu, X.-Y.; Yan, B., An efficient and sensitive fluorescent pH sensor based on amino functional metal-organic frameworks in aqueous environment. *Dalton Trans.* **2016,** *45* (16), 7078-7084.

32. Dou, Z.; Yu, J.; Xu, H.; Cui, Y.; Yang, Y.; Qian, G., Preparation and thiols sensing of luminescent metal-organic framework films functionalized with lanthanide ions. *Microporous Mesoporous Mater.* **2013,** *179*, 198-204.

33. Deibert, B. J.; Velasco, E.; Liu, W.; Teat, S. J.; Lustig, W. P.; Li, J., High-Performance Blue-Excitable Yellow Phosphor Obtained from an Activated Solvochromic Bismuth-Fluorophore Metal-Organic Framework. *Cryst. Growth Des.* **2016,** *16* (8), 4178-4182.

34. Xu, X.-Y.; Yan, B., Eu(III)-functionalized ZnO@MOF heterostructures: integration of pre-concentration and efficient charge transfer for the fabrication of a ppb-level sensing platform for volatile aldehyde gases in vehicles. *J. Mater. Chem. A* **2017,** *5* (5), 2215-2223.

35. Xu, W.; Zhang, C.-J.; Wang, H.; Wang, Y., Two Novel Two-Dimensional Lanthanide (III) Coordination Polymers Constructed from Isonicotinic Acid and Iminodiacetic Acid: Synthesis, Structure, and Luminescence Properties. *J. Cluster Sci.* **2017,** *28* (4), 2005-2015.

36. Heine, J.; Mueller-Buschbaum, K., Engineering metal-based luminescence in coordination polymers and metal-organic frameworks. *Chem. Soc. Rev.* **2013,** *42* (24), 9232-9242.

37. 2009 Residential Energy Consumption Survey, U.S. Energy Information Administration. https://www.eia.gov/consumption/residential/data/2009/ (accessed 03/24).

38. Lustig, W. P.; Wang, F.; Teat, S. J.; Hu, Z.; Gong, Q.; Li, J., Chromophore-Based Luminescent Metal–Organic Frameworks as Lighting Phosphors. *Inorganic Chemistry* **2016,** *55* (15), 7250-7256.

39. Smith, T.; Guild, J., The C.I.E. colorimetric standards and their use. *Transactions of the Optical Society* **1931,** *33* (3), 73.

40. Bardsley, N.; Bland, S.; Hansen, M.; Pattison, L.; Pattison, M.; Stober, K.; Yamada, M. *Solid State Lighting R&D Plan*; US Department of Energy: 2015.

41. Al-Taher, F.; Banaszewski, K.; Jackson, L.; Zweigenbaum, J.; Ryu, D.; Cappozzo, J., Rapid Method for the Determination of Multiple Mycotoxins in Wines and Beers by LC-MS/MS Using a Stable Isotope Dilution Assay. *Journal of Agricultural and Food Chemistry* **2013,** *61* (10), 2378-2384.

42. USFDA, CHAPTER 07 – MOLECULAR BIOLOGY AND NATURAL TOXINS *Compliance Program Guidance Manual* **2007**.

43. Bhat, R.; Rai, R. V.; Karim, A. A., Mycotoxins in Food and Feed: Present Status and Future Concerns. *Comprehensive Reviews in Food Science and Food Safety* **2010,** *9* (1), 57-81.

44. Song, S.; Liu, N.; Zhao, Z.; Njumbe Ediage, E.; Wu, S.; Sun, C.; De Saeger, S.; Wu, A., Multiplex Lateral Flow Immunoassay for Mycotoxin Determination. *Analytical Chemistry* **2014,** *86* (10), 4995-5001.

45. USFDA, Action Levels for Aflatoxins in Animal Feeds. *CPG Sec. 683.100 Action Levels for Aflatoxins in Animal Feeds* **2014**.

46. Yue, S.; Jie, X.; Wei, L.; Bin, C.; Dou Dou, W.; Yi, Y.; QingXia, L.; JianLin, L.; TieSong, Z., Simultaneous Detection of Ochratoxin A and Fumonisin B1 in Cereal Samples Using an Aptamer–Photonic Crystal Encoded Suspension Array. *Analytical Chemistry* **2014,** *86* (23), 11797-11802.

47. Gong, Q.; Hu, Z.; Deibert, B. J.; Emge, T. J.; Teat, S. J.; Banerjee, D.; Mussman, B.; Rudd, N. D.; Li, J., Solution Processable MOF Yellow Phosphor with Exceptionally High Quantum Efficiency. *J. Am. Chem. Soc.* **2014,** *136* (48), 16724-16727.

48. Hoffman, R., *J. Chem. Phys.* **1963,** *39*.

49. Whangbo, M. H.; Hoffmann, R.; Woodward, R. B., *Proc. R. Soc. London* **1979,** *A366*.

50. Pramanik, S.; Zheng, C.; Zhang, X.; Emge, T. J.; Li, J., New Microporous Metal-Organic Framework Demonstrating Unique Selectivity for Detection of High Explosives and Aromatic Compounds. *J. Am. Chem. Soc.* **2011,** *133* (12), 4153-4155.

51. Hu, Z.; Pramanik, S.; Tan, K.; Zheng, C.; Liu, W.; Zhang, X.; Chabal, Y. J.; Li, J., Selective, Sensitive, and Reversible Detection of Vapor-Phase High Explosives via Two-Dimensional Mapping: A New Strategy for MOF-Based Sensors. *Cryst. Growth Des.* **2013,** *13* (10), 4204-4207.

52. Pramanik, S.; Hu, Z. C.; Zhang, X.; Zheng, C.; Kelly, S.; Li, J., A Systematic Study of Fluorescence-Based Detection of Nitroexplosives and Other Aromatics in the Vapor Phase by Microporous Metal-Organic Frameworks. *Chem-Eur J* **2013,** *19* (47), 15964-15971.

53. Banerjee, D.; Hu, Z.; Pramanik, S.; Zhang, X.; Wang, H.; Li, J., Vapor phase detection of nitroaromatic and nitroaliphatic explosives by fluorescence active metal-organic frameworks. *CrystEngComm* **2013,** *15* (45), 9745-9750.

54. Hu, Z.; Tan, K.; Lustig, W. P.; Wang, H.; Zhao, Y.; Zheng, C.; Banerjee, D.; Emge, T. J.; Chabal, Y. J.; Li, J., Effective sensing of RDX via instant and selective detection of ketone vapors. *Chem. Sci.* **2014,** *5* (12), 4873-4877.

55. Han, X.; Liu, D.-E.; Wang, T.; Lu, H.; Ma, J.; Chen, Q.; Gao, H., Aggregation-Induced-Emissive Molecule Incorporated into Polymeric Nanoparticulate as FRET Donor for Observing Doxorubicin Delivery. *ACS Applied Materials & Interfaces* **2015,** *7* (42), 23760-23766.

56. Iasilli, G.; Battisti, A.; Tantussi, F.; Fuso, F.; Allegrini, M.; Ruggeri, G.; Pucci, A., Aggregation-Induced Emission of Tetraphenylethylene in Styrene-Based Polymers. *Macromolecular Chemistry and Physics* **2014,** *215* (6), 499-506.

57. Tong, H.; Hong, Y.; Dong, Y.; Hau; Lam, J. W. Y.; Li, Z.; Guo, Z.; Guo, Z.; Tang, B. Z., Fluorescent "light-up" bioprobes based on tetraphenylethylene derivatives with aggregation-induced emission characteristics. *Chemical Communications* **2006,** (35), 3705-3707.

58. Mei, J.; Leung, N. L. C.; Kwok, R. T. K.; Lam, J. W. Y.; Tang, B. Z., Aggregation-Induced Emission: Together We Shine, United We Soar! *Chemical Reviews* **2015,** *115* (21), 11718-11940.

59. Shustova, N. B.; McCarthy, B. D.; Dinca, M., Turn-On Fluorescence in Tetraphenylethylene-Based Metal-Organic Frameworks: An Alternative to Aggregation-Induced Emission. *J. Am. Chem. Soc.* **2011,** *133* (50), 20126-20129.

60. Pramanik, S.; Hu, Z.; Zhang, X.; Zheng, C.; Kelly, S.; Li, J., A Systematic Study of Fluorescence-Based Detection of Nitroexplosives and Other Aromatics in the Vapor Phase by Microporous Metal–Organic Frameworks. *Chemistry – A European Journal* **2013,** *19* (47), 15964-15971.

61. Lan, A.; Li, K.; Wu, H.; Olson, D. H.; Emge, T. J.; Ki, W.; Hong, M.; Li, J., A luminescent microporous metal-organic framework for the fast and reversible detection of high explosives. *Angew. Chem., Int. Ed.* **2009,** *48* (13), 2334-2338.

62. Hu, Z.; Huang, G.; Lustig, W. P.; Wang, F.; Wang, H.; Teat, S. J.; Banerjee, D.; Zhang, D.; Li, J., Achieving exceptionally high luminescence quantum efficiency by immobilizing an AIE molecular chromophore into a metal-organic framework. *Chem. Commun. (Cambridge, U. K.)* **2015,** *51* (15), 3045-3048.

63. Shustova, N. B.; Ong, T.-C.; Cozzolino, A. F.; Michaelis, V. K.; Griffin, R. G.; Dincă, M., Phenyl Ring Dynamics in a Tetraphenylethylene-Bridged Metal–Organic Framework: Implications for the Mechanism of Aggregation-Induced Emission. *Journal of the American Chemical Society* **2012,** *134* (36), 15061-15070.

64. Hu, Z.; Lustig, W. P.; Zhang, J.; Zheng, C.; Wang, H.; Teat, S. J.; Gong, Q.; Rudd, N. D.; Li, J., Effective Detection of Mycotoxins by a Highly Luminescent Metal–Organic Framework. *Journal of the American Chemical Society* **2015,** *137* (51), 16209-16215.

65. Nimmermark, A.; Öhrström, L.; Reedijk, J., Metal-ligand bond lengths and strengths: are they correlated? A detailed CSD analysis. *Zeitschrift für Kristallographie - Crystalline Materials* **2013,** *228* (7), 311-317.

66. Hu, Z.; Huang, G.; Lustig, W. P.; Wang, F.; Wang, H.; Teat, S. J.; Banerjee, D.; Zhang, D.; Li, J., Achieving exceptionally high luminescence quantum efficiency by immobilizing an AIE molecular chromophore into a metal–organic framework. *Chemical Communications* **2015,** *51* (15), 3045-3048.

67. Wang, F.; Liu, W.; Teat, S. J.; Xu, F.; Wang, H.; Wang, X.; An, L.; Li, J., Chromophore-immobilized luminescent metal–organic frameworks as potential lighting phosphors and chemical sensors. *Chemical Communications* **2016,** *52* (67), 10249-10252.

68. *Bruker Apex3*, Bruker Analytical X-ray Systems Inc.: Madison, WI, 2003.

69. *Bruker SAINT: SAX Area-Detector Integration Program* v7.60a; Bruker Analytical X-ray Systems, Inc.: Madison, WI, 2010.

70. Blessing, R., An empirical correction for absorption anisotropy. *Acta Crystallographica Section A* **1995,** *51* (1), 33-38.

71. Farrugia, L., WinGX suite for small-molecule single-crystal crystallography. *Journal of Applied Crystallography* **1999,** *32* (4), 837-838.

72. Sheldrick, G., A short history of SHELX. *Acta Crystallographica Section A* **2008,** *64* (1), 112-122.

73. Spek, A. L., PLATON SQUEEZE: a tool for the calculation of the disordered solvent contribution to the calculated structure factors. *Acta Crystallogr C Struct Chem* **2015,** *71* (Pt 1), 9-18.

74. Becke, A. D., Density-functional exchange-energy approximation with correct asymptotic behavior. *Physical Review A* **1988,** *38* (6), 3098-3100.

75. Lee, C.; Yang, W.; Parr, R. G., Development of the Colle-Salvetti correlation-energy formula into a functional of the electron density. *Physical Review B* **1988,** *37* (2), 785-789.

76. Frisch, M. J.; Trucks, G. W.; H. B. Schlegel; G. E. Scuseria; M. A. Robb; J. R. Cheeseman; G. Scalmani; V. Barone; B. Mennucci; G. A. Petersson; H. Nakatsuji; M. Caricato; X. Li; H. P. Hratchian; A. F. Izmaylov; J. Bloino; G. Zheng; J. L. Sonnenberg; M. Hada; M. Ehara; K. Toyota; R. Fukuda; J. Hasegawa; M. Ishida; T. Nakajima; Y. Honda; O. Kitao; H. Nakai; T. Vreven; J. A. Montgomery, J.; J. E. Peralta; F. Ogliaro; M. Bearpark; J. J. Heyd; E. Brothers; K. N. Kudin; V. N. Staroverov; T. Keith; R. Kobayashi; J. Normand; K. Raghavachari; A. Rendell; J. C. Burant; S. S. Iyengar; J. Tomasi; M. Cossi; N. Rega; J. M. Millam; M. Klene; J. E. Knox; J. B. Cross; V. Bakken; C. Adamo; J. Jaramillo; R. Gomperts; R. E. Stratmann; O. Yazyev; A. J. Austin; R. Cammi; C. Pomelli; J. W. Ochterski; R. L. Martin; K. Morokuma; V. G. Zakrzewski; G. A. Voth; P. Salvador; J. J. Dannenberg; S. Dapprich; A. D. Daniels; O. Farkas; J. B. Foresman; J. V. Ortiz; J. Cioslowski; Fox, D. J. *Gaussian 09*, Revision D.01; Gaussian, Inc.: Wallingford CT, 2013.

77. Sosa, C.; Andzelm, J.; Elkin, B. C.; Wimmer, E.; Dobbs, K. D.; Dixon, D. A., A local density functional study of the structure and vibrational frequencies of molecular transition-metal compounds. *The Journal of Physical Chemistry* **1992,** *96* (16), 6630-6636.

78. Becke, A. D., A new mixing of Hartree–Fock and local density-functional theories. *The Journal of Chemical Physics* **1993,** *98* (2), 1372-1377.

79. Godbout, N.; Salahub, D. R.; Andzelm, J.; Wimmer, E., Optimization of Gaussian-type basis sets for local spin density functional calculations. Part I. Boron through neon, optimization technique and validation. *Canadian Journal of Chemistry* **1992,** *70* (2), 560-571.

80. Huang, Y.; Xing, J.; Gong, Q.; Chen, L.-C.; Liu, G.; Yao, C.; Wang, Z.; Zhang, H.-L.; Chen, Z.; Zhang, Q., Reducing aggregation caused quenching effect through co-assembly of PAH chromophores and molecular barriers. *Nature Communications* **2019,** *10* (1), 169.

81. Lustig, W. P.; Li, J., Luminescent metal–organic frameworks and coordination polymers as alternative phosphors for energy efficient lighting devices. *Coordination Chemistry Reviews* **2018,** *373*, 116-147.

82. Gong, Q.; Hu, Z.; Deibert, B. J.; Emge, T. J.; Teat, S. J.; Banerjee, D.; Mussman, B.; Rudd, N. D.; Li, J., Solution Processable MOF Yellow Phosphor with Exceptionally High Quantum Efficiency. *Journal of the American Chemical Society* **2014,** *136* (48), 16724-16727.

83. Deibert, B. J.; Velasco, E.; Liu, W.; Teat, S. J.; Lustig, W. P.; Li, J., High-Performance Blue-Excitable Yellow Phosphor Obtained from an Activated Solvochromic Bismuth-Fluorophore Metal–Organic Framework. *Crystal Growth & Design* **2016,** *16* (8), 4178-4182.

84. Wei, Z.; Gu, Z.-Y.; Arvapally, R. K.; Chen, Y.-P.; McDougald, R. N.; Ivy, J. F.; Yakovenko, A. A.; Feng, D.; Omary, M. A.; Zhou, H.-C., Rigidifying Fluorescent Linkers by Metal–Organic Framework Formation for Fluorescence Blue Shift and Quantum Yield Enhancement. *Journal of the American Chemical Society* **2014,** *136* (23), 8269-8276.

85. Ma, J.-x.; Huang, X.-f.; Song, X.-q.; Liu, W.-s., Assembly of Framework-Isomeric 4 d–4 f Heterometallic Metal–Organic Frameworks with Neutral/Anionic Micropores and Guest-Tuned Luminescence Properties. *Chemistry – A European Journal* **2013,** *19* (11), 3590-3595.

86. Zhang, M.; Feng, G.; Song, Z.; Zhou, Y.-P.; Chao, H.-Y.; Yuan, D.; Tan, T. T. Y.; Guo, Z.; Hu, Z.; Tang, B. Z.; Liu, B.; Zhao, D., Two-Dimensional Metal–Organic Framework with Wide Channels and Responsive Turn-On Fluorescence for the Chemical Sensing of Volatile Organic Compounds. *Journal of the American Chemical Society* **2014,** *136* (20), 7241-7244.

87. Shustova, N. B.; Cozzolino, A. F.; Reineke, S.; Baldo, M.; Dincă, M., Selective Turn-On Ammonia Sensing Enabled by High-Temperature Fluorescence in Metal–Organic Frameworks with Open Metal Sites. *Journal of the American Chemical Society* **2013,** *135* (36), 13326-13329.

88. Jousselme, B.; Blanchard, P.; Frère, P.; Roncali, J., Enhancement of the π-electron delocalization and fluorescence efficiency of 1,6-diphenyl-1,3,5-hexatriene by covalent rigidification. *Tetrahedron Letters* **2000,** *41* (26), 5057-5061.

89. Pyo, K.; Thanthirige, V. D.; Kwak, K.; Pandurangan, P.; Ramakrishna, G.; Lee, D., Ultrabright Luminescence from Gold Nanoclusters: Rigidifying the Au(I)–Thiolate Shell. *Journal of the American Chemical Society* **2015,** *137* (25), 8244-8250.

90. Jacobsen, J. A.; Stork, J. R.; Magde, D.; Cohen, S. M., Hydrogen-bond rigidified BODIPY dyes. *Dalton Transactions* **2010,** *39* (3), 957-962.

91. Frisch, M. J.; Pople, J. A.; Binkley, J. S., Self-consistent molecular orbital methods 25. Supplementary functions for Gaussian basis sets. *The Journal of Chemical Physics* **1984,** *80* (7), 3265-3269.

92. Grein, F., Twist Angles and Rotational Energy Barriers of Biphenyl and Substituted Biphenyls. *The Journal of Physical Chemistry A* **2002,** *106* (15), 3823-3827.

93. O'Reilly, D.; Stein, R. S.; Patrascu, M. B.; Jana, S. K.; Kurian, J.; Moitessier, N.; Damha, M. J., Exploring Atypical Fluorine–Hydrogen Bonds and Their Effects on Nucleoside Conformations. *Chemistry – A European Journal* **2018,** *24* (61), 16432-16439.

94. Mulfort, K. L.; Farha, O. K.; Malliakas, C. D.; Kanatzidis, M. G.; Hupp, J. T., An Interpenetrated Framework Material with Hysteretic CO2 Uptake. *Chemistry – A European Journal* **2010,** *16* (1), 276-281.

95. Bae, Y.-S.; Dubbeldam, D.; Nelson, A.; Walton, K. S.; Hupp, J. T.; Snurr, R. Q., Strategies for Characterization of Large-Pore Metal-Organic Frameworks by Combined Experimental and Computational Methods. *Chemistry of Materials* **2009,** *21* (20), 4768-4777.

Acknowledgements of Previous Publications

Chapters 1.1, 1.2, and 1.4 (including figures) are adapted with permission from reference 81. Copyright 2018, Elsevier.

Chapter 1.3 (including figures) is adapted with permission from reference 3. Copyright 2018, Royal Society of Chemistry.

Chapter 2 (including figures and tables) is adapted with permission from reference 62. Copyright 2015, American Chemical Society.

Chapter 3 (including figures and tables) is adapted with permission from reference 25. Copyright 2016, American Chemical Society.

Chapter 4 will be published in the near future.

Chapter 5 will be published in the near future.